

8-2015

The Lunar Exosphere: Spatial and Temporal Variations of Sodium and Potassium Emissions from November 2013 to May 2014

Dona Chathuni P. Kuruppuaratchi

Follow this and additional works at: <https://commons.erau.edu/edt>



Part of the [Astrophysics and Astronomy Commons](#), and the [Engineering Physics Commons](#)

Scholarly Commons Citation

Kuruppuaratchi, Dona Chathuni P., "The Lunar Exosphere: Spatial and Temporal Variations of Sodium and Potassium Emissions from November 2013 to May 2014" (2015). *Dissertations and Theses*. 222.
<https://commons.erau.edu/edt/222>

This Thesis - Open Access is brought to you for free and open access by Scholarly Commons. It has been accepted for inclusion in Dissertations and Theses by an authorized administrator of Scholarly Commons. For more information, please contact commons@erau.edu.

THE LUNAR EXOSPHERE: SPATIAL AND TEMPORAL
VARIATIONS OF SODIUM AND POTASSIUM EMISSIONS
FROM NOVEMBER 2013 TO MAY 2014

BY

DONA CHATHUNI P. KURUPPUARATCHI

A Thesis

Submitted to the Department of Physical Sciences

and the Committee on Graduate Studies

In partial fulfillment of the requirements

for the degree of

Master of Science in Engineering Physics

08/2015

Embry-Riddle Aeronautical University

Daytona Beach, Florida

© Copyright by Dona Chathuni P. Kuruppuaratchi 2015

All Rights Reserved

THE LUNAR EXOSPHERE: SPATIAL AND TEMPORAL
VARIATIONS OF SODIUM AND POTASSIUM EMISSIONS
FROM NOVEMBER 2013 TO MAY 2014

by

Dona Chathuni P. Kurupparatchi

This thesis was prepared under the direction of the candidate's Thesis Committee Chair, Dr. Edwin J. Mierkiewicz, Thesis Committee members Dr. Theodore von Hippel, Dr. Bereket Berhane, and external Thesis Committee member Dr. Ronald J. Oliverson. It was submitted to the Department of Physical Sciences in partial fulfillment of the requirements for the degree

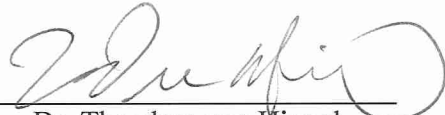
of

Master of Science in Engineering Physics

THESIS COMMITTEE



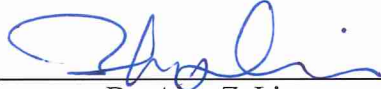
Dr. Edwin J. Mierkiewicz,
Committee Chair



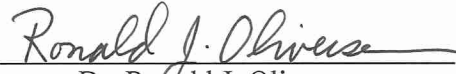
Dr. Theodore von Hippel,
Committee Member



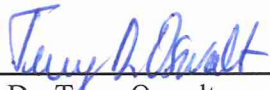
Dr. Bereket Berhane,
Committee Member



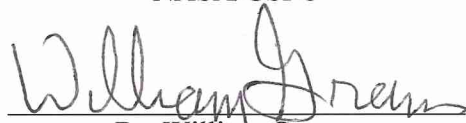
Dr. Alan Z. Liu,
Graduate Program Chair,
Engineering Physics



Dr. Ronald J. Oliverson,
External Committee Member
NASA/GSFC



Dr. Terry Oswalt,
Department Chair,
Physical Sciences



Dr. William Grams,
Dean, College of Arts and
Sciences



Dr. Christopher Grant,
Vice Chancellor

ABSTRACT

I apply high resolution spectroscopy to investigate the lunar exosphere by measuring sodium and potassium spectral line profiles to determine spatial and temporal variations in exospheric effective temperatures and velocities. Observations were made from the National Solar Observatory (MMP) at Kitt Peak, Arizona from November 2013 to May 2014, with the exception of March 2014. Data collection was centered on full Moon and spanned several nights with lunar phase angle coverage ranging from 65.6° (waxing) to 78.7° (waning). Observations were concurrent with the NASA LADEE mission science and instrument testing phases. We used a dual etalon Fabry-Perot spectrometer with a resolving power of 180,000 (1.7 km s^{-1}) to measure the line widths and radial velocity shifts of the sodium D2 (5889.9506 \AA) and potassium D1 (7698.9646 \AA) emission lines. The instrument's three arcmin field of view ($\sim 336 \text{ km}$) was positioned at several locations off the lunar limb in each of the four cardinal directions. Only data taken up to 28 seconds in time are presented and discussed in this thesis.

The sodium line widths were mostly symmetric for both waxing and waning phase angles, with line widths being approximately constant at phase angles larger than 40° . The line widths, and thus line width derived effective temperatures, were largest during magnetotail passage (phase angle $0 - 40^\circ$). The line widths outside of the magnetotail (phase angle $> 40^\circ$) were $1.5 - 2.0 \text{ km s}^{-1}$ ($\sim 1100 - 1500 \text{ K}$) while the line widths during full Moon (phase angle $\sim 6^\circ$) increased to $\sim 4 \text{ km s}^{-1}$ ($\sim 8000 \text{ K}$). The selenographic east limb was hotter than the selenographic west limb, resulting from either location or the role plasma sheet ions play in priming the lunar surface. While line width derived temperatures are indicative of an energetic source such as PSD, the large line widths during full Moon could be due to an observed red shift in velocities due to looking down the extended sodium tail.

Observed Potassium line widths are much higher ($\sim 50\%$) during waxing phase than waning phase at phase angles $> 40^\circ$. The Potassium temperatures pre-magnetotail passage are $\sim 1000\text{K}$ and post-magnetotail passage are $\sim 2000\text{K}$. Potassium is not detected during full Moon period. The potassium relative intensities for the equatorial regions are similar. The brightest observed limb region was off the Aristarchus crater, which is located near the KREEP region.

ACKNOWLEDGEMENTS

This thesis has taken many hardworking months to come into completion, and finally, after almost 2 years it has turned into a piece of work I never imagined would be possible. I would like to take this opportunity to thank my wonderful advisors, who also happen to be my observing partners, and without whom this work would have never turned into a thesis.

A big thank you to Dr. Mierkiewicz for believing in me and giving me the opportunity to conduct this wonderful research. Thank you for your patience, guidance, encouragement and constant advice in helping me conduct and complete this research work. A big thank you to Dr. Oliverson (Ron), whom despite being an external advisor and having multiple other jobs, has always been there throughout the course of this work. Thank you for your guidance, encouragement, constant advice, and last but not least, for making observing fun with your loud music that keeps everyone awake and mini adventures on and off the mountain. The MMP is a fun place when you are around.

Thank you to both Dr. Mierkiewicz and Dr. Oliverson for helping me embark on this enriching journey, which I hope will continue for a long time. I am thankful to both of you for carefully scrutinizing my written work, which eventually made me a better writer. I have learnt many useful skills, gained valuable knowledge, met a lot of people, and have become not only a better student and researcher, but a better person.

Thank you to Nick Derr, my colleague and friend, who is always coming up with tech-savvy ways to sort out the enormous amount of data we have collected to this date. Without his help, it would have taken me much longer to sort and process all the data. Thank you for the potassium data processing and analysis. Thank you for all the other observers who came out and made observing fun (Maggie, Chad, Sara, Maurice, Lori).

A heartfelt thank you to my family and friends for their constant support, encouragement, and words of wisdom. Thank you to my parents for their undying love and support, and for always believing in me, no matter what. It is an honor to be your daughter. I am grateful to my wonderful friends, who are always there for me. Thank you for making life more bearable during times when work was so overwhelming.

I would like to thank the National Solar Observatory for use of their fine telescope and especially the assistance of Detrick Branstom and Matt Penn. The lunar team will always be appreciative of the advice from Dr. Fred Roesler, University of Wisconsin and Jody Wilson, University of New Hampshire. Finally, this work was supported by NASA grants NNX11AE38G and NNX13AL30G.

CONTENTS

1. Introduction	1
1.1. Our Moon: A Brief Introduction and its Significance in Space Exploration	2
1.2. The Lunar Exosphere and a History of its Study	4
1.2.1. First Ground-Based Observations of the Lunar Sodium and Potassium Exosphere (Late 1980's to Early 2000's)	6
1.2.2. The Lunar Sodium and Potassium Exosphere: The Current State of Affairs 10	
1.2.3. Source Mechanisms of the Lunar Sodium Atmosphere	12
1.2.4. Sink and Transport Mechanisms of the Lunar Atmosphere	16
1.2.5. Direct Temperature Measurements	19
1.3. Differences between Exospheric Sodium and Potassium	20
1.3.1. Potassium and KREEP	21
1.4. Significance of Study	22
2. Telescope and Instrumentation	23
2.1. Telescope	23
2.2. Fabry-Perot Spectrometer (FPS)	26
2.2.1. Fabry-Perot Spectrometers, A Brief Introduction:	27
2.3. Fabry-Perot Spectroscopy for the Study of Lunar Exospheric Emissions	30
2.3.2. UW/GSFC dual etalon Fabry-Perot	35
2.4. Focus and Collimation	38
2.5. Pressure Tuning and Ring Radius	39
2.6. Dispersion	41
3. Observations	43
3.1. Observational Setup	44
3.2. Observing Methodology	45
3.2.1. Observational Sequence, Drift, and Telescope Guiding	46
3.2.2. Sky Background	50
4. Data Reduction	52

4.1.	Fabry-Perot CCD Annular Summing Technique and Code.....	53
4.1.1.	Camera Focus.....	56
4.2.	Instrumental Profile (IP).....	57
4.2.1.	IP construction	58
4.2.2.	Stability and Reliability of the IP.....	62
4.3.	VoigtFit and Fitting Model	63
4.3.1.	Fitting Model for Lunar Sodium Spectra.....	65
4.4.	Wavelength Calibration.....	68
5.	RESULTS.....	71
5.1.	Line Width (FWHM) vs Phase Angle Dependence by Month	72
5.2.	Line Width as a Function of Distance from the Limb	81
5.3.	Relative Intensity as a Function of Distance off the Limb.....	82
6.	Discussion and Conclusions	85
6.1.	Morphology of the Lunar Sodium Exosphere.....	85
6.1.1.	Equatorial Regions.....	85
6.1.2.	High Latitude Regions	90
6.1.3.	Monthly Variations	94
6.2.	Relative Intensity Trends for Sodium	97
6.2.1.	Our Observations in the Context of LADEE and Kaguya Sodium Results	103
6.3.	Global Trends of Potassium.....	105
6.3.1.	Line Width FWHM.....	105
6.3.2.	Relative Intensity Trends for Potassium.....	108
6.4.	Conclusions	110
6.5.	Future Work	111
	Appendix A.....	117

LIST OF TABLES

1.1	Detected surface boundary exospheres and some of their known data adapted from Stern (1999).....	5
1.2	Comparison of parameters between sodium and potassium (Potter and Morgan, 1988a).....	6
2.1	Optical parameters of the McMath-Pierce telescope facility as adapted from Pierce (1964) and (NOAO/AURA/NSF).....	26
2.2	Table of sodium (Juncar et al., 1981) and potassium emission lines (Fujii and Takashi, 2005) lines.....	31
2.3	Table of sodium and potassium calibration lamps with their respective wavelengths.....	31
2.4	Table of lens parameters.....	33
2.5	Table of parameters for the 50 mm dual etalon Fabry-Perot Spectrometer.....	36
2.6	Table of parameters for CCD detector.....	37
2.7	Table of parameters for narrowband filters.....	37
3.1	Summary of data runs.....	44
3.2	Table of major and minor craters used for observations, their positions, and telescope offsets by region.....	47
4.1	Table summarizing the corresponding fit parameters for the spectrum in Figure 4.10.....	66
6.1	Equatorial region line width derived effective temperatures averaged according to pre magnetotail passage ($> 40^\circ$), during magnetotail passage ($0 - 40^\circ$), post magnetotail passage ($> 40^\circ$) for all data runs.....	87
6.2	High latitude region line width derived effective temperatures averaged according to pre magnetotail passage ($> 40^\circ$), during magnetotail passage ($0 - 40^\circ$), post magnetotail passage ($> 40^\circ$) for all data runs for all data runs...	93

LIST OF FIGURES

1.1	Image of the lunar near side with the landing sites of the various Apollo missions.....	4
1.2	The lunar extended sodium atmosphere taken at third quarter (Mendillo et al., 1991).....	9
1.3	Image of the lunar sodium atmosphere 5 days after new Moon (Mendillo et al., 1991).....	9
1.4	Source, sink, and escape mechanisms of Mercury’s SBE.....	12
1.5	A close up schematic of the source, sinks, and escape mechanisms.....	13
1.6	Schematic depicting the dynamics of transport in the lunar sodium exosphere.....	13
1.7	Comparison of direct temperature observations made by Mierkiewicz et al. (2014) and those determined by Potter et al. (2000).....	20
1.8	Thorium concentrations on the Moon as mapped by the Lunar Prospector....	21
2.1	The McMath-Pierce Solar Telescope at Kitt Peak, Arizona.....	24
2.2	View of the #1 mirrors for the Main, the East auxiliary, and West auxiliary..	24
2.3	Optical layout of three mirror telescope.....	25
2.4	Schematic of the McMath-Pierce solar telescope facility showing the 3 mirror system	25

2.5	Schematic showing multiple wave reflections of an incident light beam within two highly parallel glass plates (etalons).....	27
2.6	(a) Schematic of the FPS showing individual components and the optical axis. (b) Ray tracing diagram with horizontal axis expanded by a factor of 4.	33
2.7	The UW/GSFC 50 mm dual etalon FPS situated at the MMP north Port...	34
2.8	Calibration setup showing white foam board at the focal plane.....	39
2.9	A raw FPS ring image of the sodium calibration lamp.....	39
2.10	ThNa spectrum with fit for March 2012.....	42
3.1	Image of the Moon as projected on top of instrument.....	45
3.2	The 3 arcmin entrance aperture of the instrument is shown positioned at the limb east of Aristarchus crater.	48
3.3	Schematic of observations, with different offsets, made off the Grimaldi limb.....	48
3.4	Sodium sky background raw Fabry-Perot image.....	51
4.1	Thorium hollow cathode lamp fringe pattern with the bright central fringe representing the Th I line at 5891.451 Å.	55
4.2	Ring-summed spectra of the ring image shown in Figure 4.1.....	55
4.3	Fabry-Perot ring image for a reduced ring thorium calibration scan.....	59
4.4	Fitted spectrum of a reduced ring thorium image for the ring image shown in Figure 4.3.	60
4.5	The reduced ring image with the corresponding fitted spectrum as shown in Figure 4.4.....	60

4.6	The isolated Th I line seen as a residual in Figure 4.5	61
4.7	The IP created by using the file shown in Figure 4.6.	61
4.8	Plot showing the FWHM (Doppler (DW) and Lorentzian (LW)) for all the IPs from November 2013 – May 2014.....	63
4.9	Ring-summed spectrum of a lunar sodium image taken on February 19 at the limb off the Grimaldi crater.....	64
4.10	Lunar Sodium spectrum shown in Figure 4.9 plotted with a false zero.....	64
4.11	Corresponding fitted spectrum for spectrum shown in Figure 4.9.	65
4.12	Sky background image taken 40 minutes west from the Moon center.....	68
4.13	Fabry-Perot ring image of a sodium lamp calibration image.....	70
4.14	Ring-summed spectrum of the sodium lamp image seen in Figure 4.13.....	70
5.1	Equatorial Doppler width (FWHM) as a function of phase angle for November-2013.	75
5.2	High Latitude Doppler width (FWHM) as a function of phase angle for November-2013.	75
5.3	Equatorial Doppler width (FWHM) as a function of phase angle for December-2013.	76
5.4	High Latitude Doppler width (FWHM) as a function of phase angle for December-2013.	76
5.5	Equatorial Doppler width (FWHM) as a function of phase angle for January-2014.	77
5.6	High Latitude Doppler width (FWHM) as a function of phase angle for January-2014.	77

5.7	Equatorial Doppler width (FWHM) as a function of phase angle for February-2014.	78
5.8	High Latitude Doppler width (FWHM) as a function of phase angle for February-2014.	78
5.9	Equatorial Doppler width (FWHM) as a function of phase angle for April-2014.	79
5.10	High Latitude Doppler width (FWHM) as a function of phase angle for April-2014.	79
5.11	Equatorial Doppler width (FWHM) as a function of phase angle for May-2014.	80
5.12	High Latitude Doppler width (FWHM) as a function of phase angle for May-2014.	80
5.13	FWHM as a function of distance off the selenographic north (Plato limb), south limb (Tycho limb), west limb (Aristarchus limb), and east limb (Langrenus limb).....	81
5.14	FWHM as a function of distance off the selenographic east limb (Langrenus limb) of the Moon on May 10, 2014 and off the selenographic west limb (Grimaldi limb) on May 18, 2014.....	82
5.15	Relative intensity as a function of distance off the selenographic east limb from Langrenus crater on May 10, 2014.	83
5.16	Relative intensity as a function of distance off the selenographic east limb from Cleomedes crater on May 10, 2014.....	83
5.17	Relative intensity as a function of distance off the selenographic west limb from Cleomedes crater on May 18, 2014.	84
6.1	Equatorial FWHM as a function of phase angle for all data runs ranging from November 2013 – May 2014 for equatorial regions.....	86
6.2	Equatorial FWHM as a function of phase angle for all data runs as found in Figure 6.1 with pre full Moon phases being negative.....	87
6.3	Sodium line widths as a function of phase angle for equatorial regions. Data points have been binned by intervals represented on the x-axis.	88
6.4	Global equatorial sodium data converted to line width derived effective temperatures and plotted along with results from Potter et al. (2000).....	90

6.5	FWHM as a function of phase angle for all data runs ranging from November 2013 – May 2014 for high latitude regions.....	91
6.6	FWHM as a function of phase angle for all data runs as found in Figure 6.1 with pre full Moon phases being negative	92
6.7	Sodium line widths as a function of phase angle for high latitude regions. Data points have been binned by intervals represented on the x –axis.....	92
6.8	FWHM as a function of decimal date for all data runs from November 2013 – May 2014 including both equatorial and high latitude regions.....	95
6.9	FWHM as a function of decimal date as seen in Figure 6.8 seperated into equatorial and high latitude regions.....	96
6.10	Relative intensity as a function of decimal date for all data runs from November 2013 – May 2014 including both equatorial and high latitude regions.....	98
6.11	Relative intensity as a function of decimal date as seen in Figure 6.11 seperated into equatorial and high latitude regions.....	99
6.12	Relative intensity as a function of decimal date for all data runs for data points taken at the limb.....	100
6.13	Relative intensity for equatorial and high latitude regions for May 2013.....	102
6.14	Variation in surface density of sodium atoms during day-of-year in 2009 (a) and (b) variation in surface density of sodium atoms as a function of phase angle (Kagitani et al. 2010).....	104
6.15	Potassium line widths for February 2014 as a function of phase angle.....	106
6.16	Potassium line widths for April 2014 as a function of phase angle.....	107
6.17	Potassium line widths for May 2014 as a function of phase angle.....	107
6.18	Potassium area (relative intensity) as a function of phase angle for February 2014.....	108
6.19	Potassium area (relative intensity) as a function of phase angle for April 2014.	108

6.20	Potassium area (relative intensity) as a function of phase angle for May 2014.....	109
------	--	-----

CHAPTER 1

1. Introduction

Within the framework of this thesis I report on my work utilizing the technique of Fabry-Perot spectroscopy for the study of the lunar sodium and potassium exosphere. My data set was collected over six observing runs, spanning a seven month interval from November 2013 through May 2014. I personally spent 40 nights at the McMath-Pierce Solar Telescope (Kitt Peak, AZ) collecting this data; additional observations were contributed by my collaborators as discussed in Chapter 3.

Although the intensity distributions of the lunar sodium and potassium exosphere have been measured on a number of occasions (e.g., Mendillo and Flynn, 1993, Potter et al., 1988a,b, Tyler et al., 1988), their scale height derived temperature distributions have mainly been inferred from models (e.g., Sprague et al., 2012, 1992). The data that I present here are unique in that they represent the first comprehensive look at lunar sodium and potassium line width derived exospheric temperatures over many months and lunar phases.

In the remainder of this chapter, I will briefly introduce the Moon and its significance in space exploration. I then discuss the lunar exosphere and outline a history of its study in terms of the ground based observations of sodium and potassium; recent lunar missions will also be discussed.

In the chapters that follow, I will describe the McMath-Pierce Solar Telescope and the Fabry-Perot spectrometer that I used to make these observations (Chapter 2). My observational strategy and data reduction/analysis procedures are discussed in Chapters 3 and 4. In Chapter 5 I present my sodium line width observations as a function of month, highlighting observations as a function of lunar phase angle for both equatorial and high latitude regions; sodium line widths as a function of distance from the lunar limb and sodium relative intensities as a function of distance from the lunar limb are also discussed.

In Chapter 6, I discuss the morphology of the lunar sodium exosphere in the context of my seven month data set. I also describe observed line width trends and their possible exospheric source mechanisms. Sodium relative intensities are also included in Chapter 6. My results are compared with the sodium observations of the recent LADEE and Kaguya lunar missions. I then highlight the global trends of potassium in terms of line width and relative intensity and make comparisons to sodium.

1.1. Our Moon: A Brief Introduction and its Significance in Space Exploration

Our Moon, an isolated, rocky celestial body that is Earth's only natural satellite, is a familiar object in our sky. An oddity amongst other moons in the Solar System, our Moon is the largest in size compared to its host planet. The Moon is thought to be a result of a catastrophic collision between the early Earth and a Mars sized proto-planet named Theia, approximately 4.5 billion years ago (Herwartz et al., 2014). According to this giant impact theory, the Moon should be made up of materials from both Theia and the proto-Earth. The evidence for this is found in the small difference in the isotopic oxygen makeup between the Earth and the Moon (Herwartz et al., 2014). This is contrary to what was believed previously, that the isotopic oxygen ratios between the Earth and Moon were the same.

Not only is the Moon an integral part of life on Earth, it is also a primary driving factor for space exploration. In 1961, President Kennedy declared "*I believe that this nation should commit itself to achieving the goal, before this decade is out, of landing a*

man on the Moon and returning him safely to Earth” (John F. Kennedy, special message to Congress on urgent national needs, 25 May 1961) and with this, what eventually became known as the Apollo program was born.

While the Apollo missions helped provide an insight into the history of our Moon and the Solar System, the termination of the program in 1972 also left us with many unanswered questions. Why is the far side of the Moon so different than the near side? How much water is on the Moon? What is the origin of the Moon (and by extension the Earth)? And most relevant to this thesis, what are the sources, dynamics, and evolution of the delicate lunar atmosphere?

Humanity will eventually return to the Moon. We will explore regions with possible water, map and mine the mineral composition (especially rare Earth metals), and study the lunar environment and its interaction with the Sun. Our return to the Moon will also focus on learning how to use the Moon for potential colonization, and how to apply that knowledge to the colonization of our Solar System. In fact, the Moon’s proximity to Earth makes it the ideal “laboratory” and test bed for the development of instruments, geophysical stations, robotic outposts, in-situ resource utilization, deployment of large infrastructures, and life science laboratories. Furthermore, it is anticipated that the Moon can be used as a platform to prepare humans to visit Mars. For example, the lunar platform can be used to train humans how to use available resources to replenish essential supplies from local materials, such as rocket fuel and oxygen.

In addition, since the Moon has a crustal magnetic field much weaker than Earth’s magnetic field, its surface is constantly bombarded by solar wind ions. This allows for the study of the effects of space weather on Solar System bodies similar to that of the Moon and will in turn help us understand more about the Sun.

Intimate knowledge of the lunar environment will help us further space exploration, evaluate the impacts of space weather, and contribute to our understanding of our place in the Solar System.

1.2. The Lunar Exosphere and a History of its Study

It is a widely held belief that the Moon has no atmosphere owing to its lack of clouds and hazes, both of which are optical phenomena indicative of an atmosphere. While this assumption is understandable, it is technically incorrect. The Moon in fact has a very thin, tenuous atmosphere similar to that of a cometary coma (Stern, 1999).

A number of direct in-situ observations of this tenuous atmosphere were made during the Apollo era. For example, the Apollo 17 mission's Lunar Atmospheric Composition Experiment (LACE) instrument detected small amounts of atoms/molecules including helium, neon, argon, possibly molecular hydrogen (Hoffman et al., 1973). The results of LACE and other Apollo experiments are summarized in the review by Stern (1999) which also includes the Suprathermal Ion Detector Experiment (SIDE) (Apollo 12, 14, 15), Charged Particle Lunar Environment Experiment (CPLLE) (Apollo 14), and Cold Cathode Gauge Experiments (CCGEs) (Apollo 12, 14, 15). The Apollo landing sites are shown in Figure 1.1.

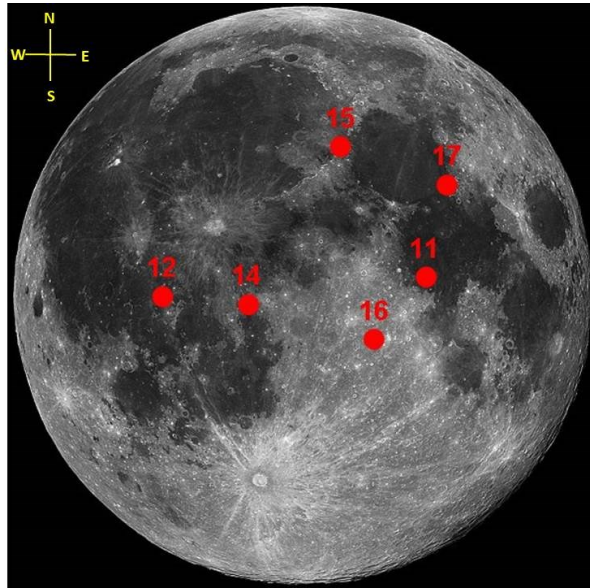


Figure 1.1: Image of the lunar near side with the landing sites of the various Apollo missions (Phillip and Barry, 2005). Note that the directions are labeled in selenographic coordinates.

Table 1.1: Detected Surface Boundary Exospheres and some of their known data adapted from Stern (1999).

Object	Species Detected	Gravity, cm s ⁻²	Total detected Surface Number density, cm ⁻³
Mercury	He, Na, K	372	8 x 10 ⁴ (day)
Moon	He, Ar, Rn, Po, Na, K	163	2 x 10 ⁵ (night)
Io	SO ₂ , SO, S, O, Na, K, Cl	187	10 ¹³ (max)
Europa	O, Na	281	2 x 10 ⁴
Callisto	H	121	2 x 10 ⁴

The Moon's atmosphere is known as a Surface Bounded Exosphere (SBE) and is similar to that of Mercury and other small Solar System objects. SBEs are found commonly on small cosmic bodies since their gravity is insufficient to retain a conventional atmosphere. As such, a SBE consists of an almost 'airless' body where energetic particles removed from the surface have a minuscule probability of colliding with each other before escaping into space or returning to the surface. The lunar SBE is scientifically interesting because it acts as a nearby laboratory that will help us understand and model other SBEs throughout the Solar System. In fact, SBEs are one of the most common types of atmosphere found in our Solar System. Some examples of detected SBEs are summarized in Table 1.1.

An SBE is continuously lost and replenished by processes discussed later in this section. Studying the lunar SBE provides essential data about the chemical makeup of the Moon's exosphere. Understanding the temporal and spatial variations of the various chemical species in the lunar exosphere provides valuable information about other small bodies in the Solar System and may also help provide insight on the origins of polar ice on the Moon. According to a white paper submitted by Neal et al. (2011) to the NASA Science Mission Directorate, lunar studies can answer questions about (1) the impact history of the inner Solar System, (2) the dynamics of the lunar exosphere and space weathering of the regolith, (3) lunar differentiation and by extension, terrestrial planet

differentiation. These questions are paramount in understanding the near lunar environment and thus our near space environment, Earth's history, and our existence on Earth.

1.2.1. First Ground-Based Observations of the Lunar Sodium and Potassium Exosphere (Late 1980's to Early 2000's)

Following a hiatus after Apollo in the study of the lunar atmosphere, a major break-through was achieved in 1988 when Potter and Morgan (1988a) made ground based observations of the sodium D1 (5895.9242 Å) and D2 (5889.9509 Å) doublet and potassium D1 (7698.96 Å) line emissions in the lunar exosphere from the McDonald Observatory (TX) and National Solar Observatory (NSO), Kitt Peak (AZ). Motivation to make lunar exospheric observations in sodium and potassium came from the discovery of these two species in Mercury's exosphere by Hunten et al. (1988). Although sodium and potassium are only minor constituents in the lunar atmosphere (Table 1.2) their ability to scatter sunlight efficiently, owing to their large scattering cross sections, make them the only species currently detected from Earth. As such, the entire body of remote lunar exospheric research conducted focuses on sodium and potassium, with more observations made for sodium. The main findings from Potter and Morgan from their 1988a study are summarized in Table 1.2.

Table 1.2: Comparison of parameters between sodium and potassium (Potter and Morgan, 1988a)

Parameter	Na	K
Limb brightness (kRayleighs [*])	3.8 ± 0.4	1.8 ± 0.4
Zenith column densities (above subsolar point) (atoms cm ⁻²)	8 ± 3 x 10 ⁸	1.4 ± 0.3 x 10 ⁸
Surface densities (atoms cm ⁻³)	67 ± 12	15 ± 3
Scale Height (km)	120 ± 42	90 ± 20

*1 Rayleigh = (10⁶/ 4π) photons⁻¹cm⁻²steradian⁻¹s⁻¹

In their 1988b paper, Potter and Morgan obtained scale heights for sodium from emissions observed at altitudes up to 1200 km above the subsolar lunar limb during third quarter phase. They concluded that since the intensity of the sodium emission is larger than predicted from the scale height and surface density measurements derived from previous low altitude sodium measurements (Potter and Morgan, 1988a), the lunar exosphere must have a “hot” and “cold” component. The two component model explained the “hot” component as being a result of sodium atoms that are liberated from the lunar regolith through an energetic source mechanism such as micrometeorite impact vaporization or sputtering by solar wind ions. The “cold” component was due to sodium atoms that have been thermally accommodated to the surface (Potter and Morgan, 1988b).

This two component atmosphere model was also used by Sprague et al. (1992) to explain a wide range of inferred scale heights, equivalent temperatures, and surface number densities for both sodium and potassium. Sprague et al. (1992) presented scale heights at the subsolar point in the range of 119 - 611 km for sodium and 85 - 154 km for potassium. The lower end of their scale height ranges agree with the scale heights presented by Potter and Morgan (1988a) summarized in Table 1.2 here. Sprague et al. (1992) also reported surface number densities for sodium and potassium of 6-34 atoms cm^{-3} and 9-10 atoms cm^{-3} respectively, and are lower than the surface densities presented by Potter and Morgan (Table 1.2). Potassium abundances were measured up to 190 km above the lunar surface by Kozlowski et al. (1990) and they also found that the potassium vertical profile was best fit by a two-component model.

Sprague et al. (1992) concluded that the atmosphere in the sub-solar region is dominated by thermal desorption (a process by which atoms are released when lunar regolith is heated), which provides a scale height corresponding to the surface temperature of the Moon (~ 400 K). In regions further out from sub solar regions (where it is cooler), the atoms tend to linger on the surface longer and are released by energetic photons incident upon them (process known as photodesorption) which gives the released atoms a higher velocity distribution (Sprague et al. 1992).

Sprague et al. (1992) also provided a latitudinal dependence of sodium scale height, implying the presence of competing source mechanisms with varying solar zenith angle. Similar evidence was provided by Mendillo et al. (1993) and Potter and Morgan (1998b), indicating that sodium abundances decreased as a function of solar zenith angle. In 1998, Potter and Morgan (1998b), measured the latitudinal dependence of sodium density and found that the sodium density peaked near the equator and fell off with an increasing latitude. Their results were best fit with a cosine squared or cubed latitudinal dependence. Findings presented by Mendillo (1995) and Mendillo et al. (1997b) showed that a simple cosine dependence did not fit their data adequately and instead they proposed that the efficiency of the process that generates sodium varies with a higher powered cosine dependence with latitude. This result was in agreement with Potter and Morgan's (1998b) results. Mendillo et al. (1997) also presented a study on the modeling of the Moon's extended sodium atmosphere and found similar results to a two component atmosphere. They concluded from their model that the extended sodium coma was produced by only the high speed tail population of the 1400 K Maxwellian distribution.

Mendillo et al. (1991) reported the detection of an extended sodium emission out to almost 7000 km or 4 lunar radii on the dayside and up to 15-20 lunar radii on the nightside (see Figure 1.2 and Figure 1.3). These figures agree with the earlier spectroscopic results from Sprague et al. (1992) that showed the polar sodium abundance in the lunar atmosphere is only 1/3 of that of low altitudes.

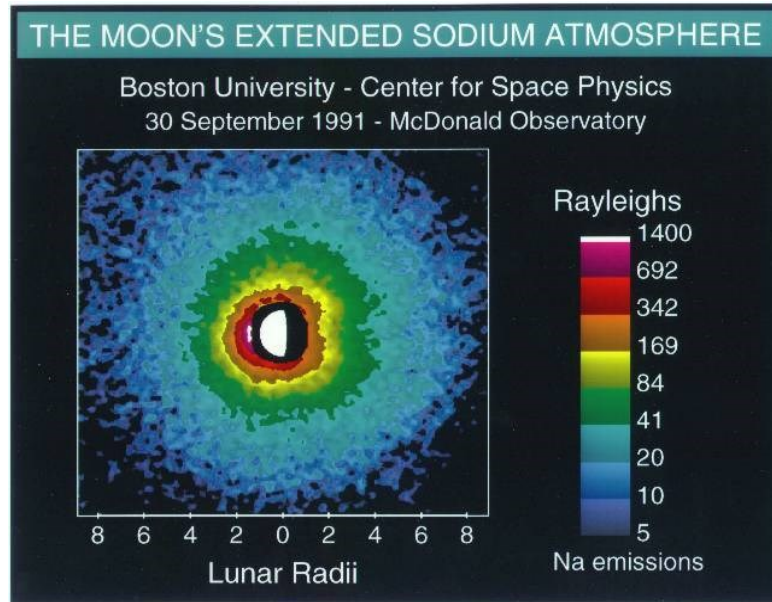


Figure 1.2: The lunar extended sodium atmosphere taken at third quarter (Mendillo et al., 1991)

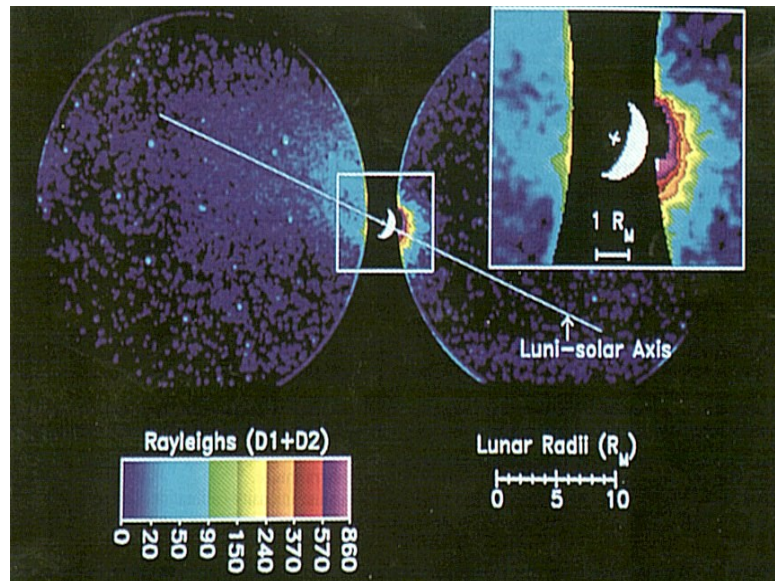


Figure 1.3: Image of the lunar sodium atmosphere 5 days after new Moon (Mendillo et al., 1991)

In 1999, Mendillo et al. (1999) reported on the lunar sodium atmosphere during four lunar eclipses between 1993 and 1997. Their results indicated the sodium atmosphere of the Moon when inside the magnetotail is comparable in abundances near first and third quarter. They inferred that sputtering by solar wind ions is not a dominant source mechanism for releasing sodium atoms. Results obtained by Potter et al. (2000) showed the sodium density is higher before entering (ingress) the Earth's magnetotail (near full Moon phase \pm 3 days) than after leaving (egress) the magnetotail, suggesting the solar wind did in fact have a significant role in the production of the lunar sodium exosphere. They proposed the role of the solar wind ions is to mobilize sodium and bring it to the surface of the Moon, where photodesorption by UV photons can inject it into the exosphere (Potter et al., 2000).

1.2.2. The Lunar Sodium and Potassium Exosphere: The Current State of Affairs

There have been several post-Apollo robotic missions to the Moon dedicated to studying its surface and atmospheric composition. Those missions are briefly outlined here and their relevant results discussed. The missions include: Chandrayaan-1, Lunar Reconnaissance Orbiter (LRO), Kaguya, Lunar Atmosphere and Dust Environment Explorer (LADEE), and Chang'e 3.

The Indian Space Research Organization's (ISRO) Chandrayaan-1 orbiter launched on September 19, 2008 and its mission objectives included gathering information about the mineralogical, topological, and geological aspects of the Moon. Its main findings included the discovery of water molecules on the polar regions of the lunar surface (Agle & Brown, 2009).

LRO, launched on June 18, 2009, was the first mission of NASA's robotic lunar exploration program. LRO's scientific goals were to map the lunar surface and scout for potential future landing sites in terms of surface roughness, available resources, and radiation environment. According to the data collected from LRO's neutron detector,

strong spikes in hydrogen indicated water ice and hydrogen may be found in permanently shadowed craters and nearby regions (Mitrofanov et al., 2012; Hayne et al., 2015).

The Japanese Kaguya (formerly known as Selene) was launched on September 14, 2007 and its main science objectives were to perform a global survey of the Moon, obtain abundances of elements present on the surface, obtain data on mineral compositions, gravity, and to observe the plasma environment (Kaguya, 2014). The Kaguya mission's findings include gravity field models of the lunar far side (Namiki et al. 2009) and improved global topography map of the lunar surface showing the presence of thorium, potassium, oxygen, magnesium, silicon, calcium, titanium, and iron (Uranium Found on Moon, 2009). Results from the Kaguya mission ranging from December 2008 to June 2009 suggest a spherical symmetry distribution of the sodium exosphere with a temperature range of 2400 – 6000 K on the lunar nightside (Kagitani et al., 2010). In the same study, Kagitani et al. (2010) suggest an inhomogeneous source distribution of photon-stimulated desorption (PSD) on the surface as a possible explanation for the variation in sodium density.

NASA's Lunar Atmosphere and Dust Environment Explorer (LADEE) mission, launched on September 7, 2013, had science objectives of determining the global density, composition, and temporal variability of the lunar atmosphere, and determining the size, charge, and spatial distribution of electrostatically charged dust particles. Some of LADEE's findings include an observed increase in sodium in the lunar exosphere coincident with the Geminids meteor shower, increased light scattering due to dust, and possible detection of iron and titanium in the exosphere (Elphic, 2014). LADEE is a relatively new mission and only a few of its findings are published.

On December 1, 2013, the China National Space Administration (CNSA) launched Chang'e 3 and included China's first lunar rover, Yutu or 'Jade Rabbit'. The scientific objectives of the mission include gathering information about the topography, metal composition, Sun-Earth-Moon near space environment, and geography of the lunar surface and lunar astronomical observation (ZeZhou et al., 2013). There are no published results to date and the Yutu rover has been immobile since January 25, 2014.

1.2.3. Source Mechanisms of the Lunar Sodium Atmosphere

Possible source mechanisms of the lunar exosphere are: (1) thermal desorption, (2) micrometeorite impact vaporization, (3) photon-stimulated desorption (PSD), (4) charged particle sputtering (by high energy particles from the solar wind), and (5) electron-stimulated desorption. Once released from the lunar surface, the sodium atoms can be lost through several mechanisms and must be continuously replenished. These loss mechanisms include: (1) gravitational escape, (2) ionization loss, and (3) solar radiation escape, and (4) gravitational capture. A full review of the above mentioned processes can be found in the review by Stern (1999). Figure 1.4 depicts a global view of the source and escape mechanisms highlighted in Figure 1.5. Although, both figures show a general picture of the source and escape mechanisms in the context of Mercury, they can be used to picture the same processes on the lunar SBE as Mercury's tenuous atmosphere is a close analog to the lunar atmosphere. A diagram showing the ballistic motion of the released sodium atoms is shown in Figure 1.6.

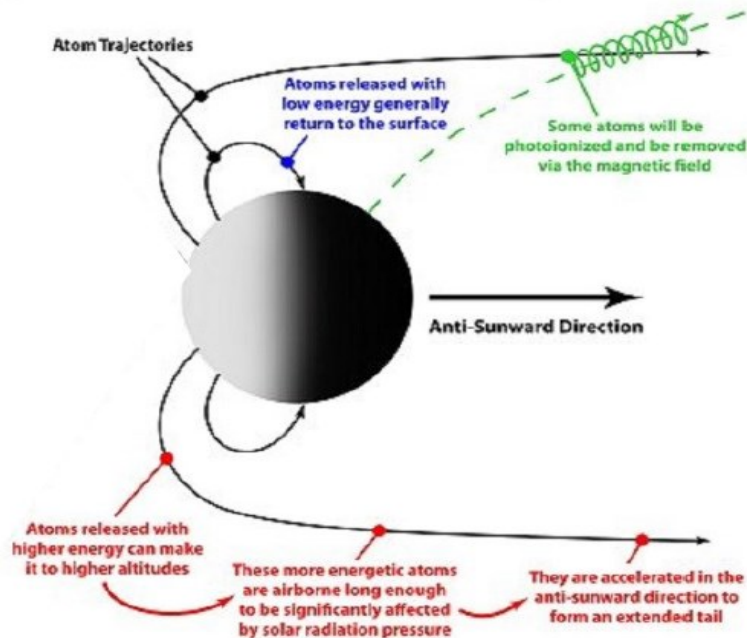


Figure 1.4: Source, sink, and escape mechanisms of Mercury's SBE. This schematic can be used to depict the dynamics of the similar lunar SBE (Phillips, 2009).

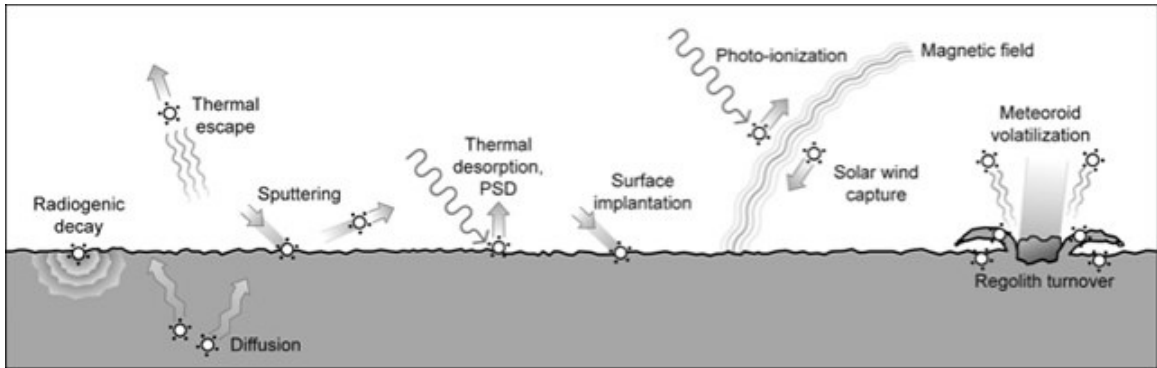


Figure 1.5: Close-up schematic of the source, sinks, and escape mechanisms discussed above in context of Mercury's SBE (MESSENGER Mission).

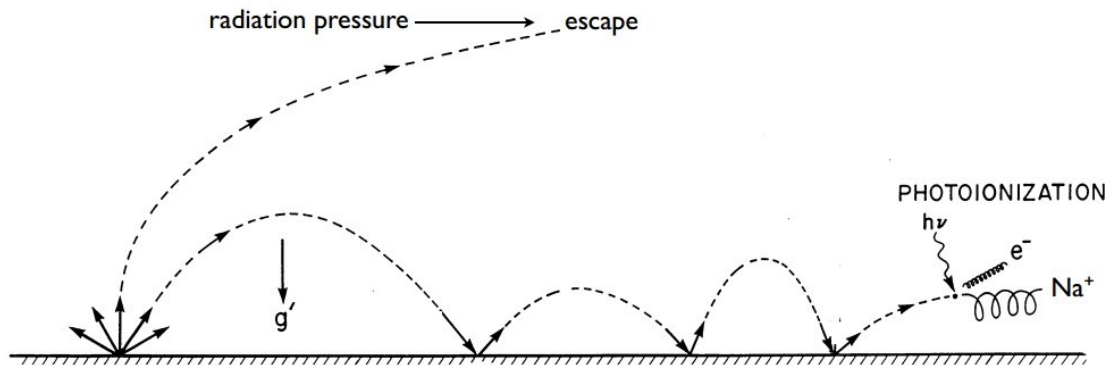


Figure 1.6: Schematic depicting the dynamics of transport in the lunar sodium exosphere. As adapted from Smyth and Marconi (1995) and reproduced in Stern (1999).

The lunar SBE is formed by source mechanisms that cover a wide range of release velocities and ejection rates acting on different surface regions (Kagitani et al., 2010) and atoms released by these mechanisms are coined “source atoms” by Smyth and Marconi (1995). Source atoms that encounter the surface can have one or more ballistic hops and are called “ambient atoms” (Smyth and Marconi, 1995). Thermal desorption is the process by which atoms and molecules sublime (Stern, 1999). Thermal desorption follows an ensemble distribution (Stern, 1999) and causes atoms to move in a ballistic motion about the surface (Sprague et al., 1992). Large fractions of ejected atoms from impact vaporization and ion sputtering escape the lunar gravity resulting in a corona, or partly escaping exosphere (Sarantos et al., 2010). Impact vaporization has important contributions over the terminator and the polar regions, especially when a cosine squared dependence on the solar zenith angle is assumed (Sarantos et al., 2010). As explained in Section 1.1.1, the cosine squared (or higher power) is a better fit to sodium abundances as a function of latitude. Micrometeorite impact can produce a vapor atmosphere and a source of hot or molten surface material that will eventually outgas until it reaches thermal equilibrium (Stern, 1999). Increase in content of sodium atoms in the lunar exosphere is expected during meteor showers due to the increased intensity of meteor bombardment (Smith et al., 1999). In one study, an enhancement in the extended lunar sodium tail was detected after the maximum of the Leonid 1998 meteor shower (Smith et al., 1999).

The importance of “sodium sputtering” caused by solar photons interacting with the surface of Mercury was first suggested by (McGrath et al., 1986). Their results were later extrapolated to explain the sputtering of sodium and potassium on the Moon by (Kozlowski et al., 1990). Desorption is the process by which a substance, in this case sodium atoms, are released from or through the pores of a surface. When the lunar regolith is irradiated by solar photons, their energy is sufficient to liberate the sodium atoms from the surface through desorption. This photodesorption is used to explain the release of atoms adsorbed on the surface with energies of approximately 4 - 1.5 eV by photons of wavelength in the 3000 - 8000 Å range (Sprague et al., 1992).

PSD and ion sputtering are expected to be the main source mechanisms if their densities vary as the cosine of the latitude since the fluxes of the solar photons and solar wind ions per unit lunar surface follows a similar law (Yokota et al., 2014). According to Yakshinskiy et al. (1999) the expected temperature of a PSD source (ignoring the tail made of non-thermal neutrals) is on the order of 1200 K. Mendillo et al. (1999) suggested that (PSD) dependent on solar-zenith angle over the sunlit hemisphere accounts for 85% of the source mechanisms that contribute to the extended sodium atmosphere. Tenishev et al. (2013) also concluded that PSD is the dominating source process that exceeds the rate of meteoritic impact vaporization by factor of about 8 - 9.

Charged particle sputtering is the process by which energetic solar wind particles (electrons, protons, and alpha particles) hit the lunar regolith and release atoms into the lunar exosphere. Kinetic energies of solar wind ions are approximately 1 keV/amu, where amu is an atomic mass unit (Killen et al., 2012). Killen et al. (2012) presented results that suggest that increased sputtering during a (coronal mass ejection) CME could cause (1) the total atmospheric sodium content to increase by 14.5 times the ambient atmosphere and (2) the scale height of the atmosphere to increase, due to the higher energy sodium atoms from charged particle sputtering compared to PSD.

The Moon spends approximately 5-6 days inside the Earth's magnetosphere and during this time the lunar surface is both shielded from solar wind particles and exposed to high energy magnetospheric particles. When the Moon's orbit intersects the Earth's plasma sheet, fluxes of energetic electrons and ions energized by plasma processes such as magnetic reconnection and turbulence are expected to bombard its surface and strongly interact with the lunar exosphere (Sarantos et al., 2010). Energies of particles in the current sheet plasma are on the order of 3 keV (Slavin et al., 1985). The energetic particles found in the plasma sheet are known to cause "priming" of the lunar surface which allows PSD to effectively release sodium atoms from the surface more efficiently (Sarantos et al., 2010). The model presented by Sarantos et al. (2010) indicates that plasma sheet ion induced effects doubles the PSD efficiency for flux typical of the solar wind at 1 AU. Furthermore, the model shows that the enhancement in relative efficiency of PSD due to the bombardment of the lunar surface by plasma sheet ions is

approximately two times higher than the enhancement of PSD due to bombardment by solar wind ions. Sarantos et al. (2010) concluded that PSD is the major source of the lunar sodium exosphere and has both temporal and spatial variation due to the variability of the ion influx to the lunar surface. The dependence of PSD efficiency on ion sputtering and position of the Moon in the lunar orbit shown by Sarantos et al. (2010) is confirmed in the study done by Tenishev et al. (2013). Furthermore, a two-step process comprising of priming the lunar surface and release of atoms by PSD is agreement with previously mentioned cosine squared (or higher powered) dependence of sodium abundances with latitude.

1.2.4. Sink and Transport Mechanisms of the Lunar Atmosphere

The sink mechanisms of the lunar exosphere include: (1) gravitational escape, (2) ionization loss, (3) solar radiation escape, and (4) gravitational capture. These processes are highlighted in Figures 1.4 – 1.6 in the previous section. Gravitational escape is the process by which atoms or molecules with radial velocities greater than the escape velocity of the Moon (2.38 km s^{-1}) are lost from the surface. Atoms or molecules with escape velocities greater than that of the Moon are lost from the surface while those with a smaller escape velocity are pulled back onto the surface.

Ionization loss is the process by which ionized atoms escape the lunar surface due to being accelerated at speeds exceeding the escape velocity of the Moon by means of the solar wind electric field (Stern, 1999). Ionization sources include photoionization by solar photons and solar wind particles. In other words, these atoms are swept away by the solar wind. The first ionization potential for sodium and potassium is 5.14 eV and 4.34 eV, respectively. According to Stern (1999), the most dominant and fastest ionization process is photoionization. The lifetime of sodium and potassium atoms due to photoionization in the sunlit side of the lunar atmosphere is on the order of 42 hours (Huebner, 1992; Combi et al., 1997; Cremonese and Verani, 1997; Wilson et al., 2003).

Once released the atom can either undergo gravitational escape or gravitational capture, depending on its kinetic energy. If the ambient atom is not captured or partially captured by the surface, it will form the ambient atmosphere (Smyth and Marconi, 1995). In the case of sodium, most neutral atoms injected into the exosphere have initial energies that are not sufficient for gravitational escape from the lunar surface (Tenishev et al., 2013). According to Tenishev et al. (2013), only about 10 % of the neutral sodium atoms have enough energy for gravitational escape and the rest move along trajectories that intersect with the lunar surface where they bounce or become bound to the lunar regolith.

Atoms released from the surface can also be pushed away by solar radiation pressure. Solar radiation pressure provides acceleration to atoms and molecules thereby increasing their escape rates (Stern, 1999). Solar radiation pressure is also what causes the Moon to have a sodium “tail”. Depending on the radial component of the heliocentric velocity, neutral sodium atoms can be accelerated in the anti-solar direction by solar radiation pressure, allowing atoms with speeds close to escape velocity to increase their velocities by a gain in momenta and thus enabling them to escape the lunar gravity and move into the sodium tail (Tenishev et al., 2013; Wilson et al., 2003).

Energetic ambient atoms from the dayside atmosphere on long ballistic orbits can directly populate the nightside atmosphere, while less energetic ambient atoms in the dayside atmosphere can populate the nightside atmosphere by lateral transport that may be enhanced by solar radiation pressure acceleration (Smyth and Marconi, 1995). Atoms that are liberated from the surface will either stick to the surface or move independently from one point to another by a series of ballistic hops. The number and shape of these ballistic hops are determined by the relevant forces acting upon each atom (gravity and solar radiation pressure), the nature of the gas-surface interactions (dependent on local temperatures and compositions), and the various operative loss processes (Smyth and Marconi, 1995). If the ballistic component of these liberated atoms is not captured by the surface, an ambient atmosphere is formed (Smyth and Marconi, 1995). These atoms in the atmosphere can then be lost due to solar radiation pressure. Subsequently, low energy atoms on the nightside atmosphere can populate the dayside atmosphere and can be slowed down due to solar radiation acceleration (Smyth and Marconi, 1995).

Furthermore, atoms on the nightside may be captured by the surface and returned to the dayside due to the rotation of the Moon. Atoms on the dayside can undergo photoionization and be lost due to either magnetospheric convective loss or recycling to the lunar surface by gravitational capture (Smyth and Marconi, 1995). PSD is considered to be the dominant source mechanism for generating the lunar alkali exosphere (sodium and potassium) as shown by the results of Sprague et al. (1992), Mendillo et al. (1998), and Sarantos et al. (2010), and if not replenished, PSD would deplete the surface alkalis (Yokota et al., 2014).

In their study, Yokota et al. (2014), present latitude and longitude distributions of Na^+ and K^+ fluxes from the Moon derived from the Kaguya low-energy ion data. From their model, they concluded that lunar surface abundances of sodium and potassium decreases to approximately 50% at dusk compared to dawn. They also inferred from their data that the surface abundance of sodium and potassium need to be supplied during the night to explain the lunar exosphere with dawn-dusk asymmetry. In addition, they suggest that to maintain the exosphere with this dawn-dusk asymmetry, the lunar surface needs a supply of approximately 70% of the sodium and potassium surface abundance at dawn during one lunar day. Tenishev et al. (2013) suggest that the total recycle rate of the exospheric sodium is $1.15 \times 10^{23} \text{ s}^{-1}$ which gives an escape rate from the exosphere on the order of $5.3 \times 10^{22} \text{ s}^{-1}$. The replenishing processes suggested by Yokota et al. (2014) are (1) grain diffusion, (2) migration/recycling of the exosphere, and (3) supply by micrometeorites. Stern (1999), in his review, summarizes reservoirs/replenishing processes for sodium and potassium as coming from the lunar regolith, meteorites, comets, and from sputtering by solar wind ions.

Observed variations in longitude, phase angle (i.e. position of Moon in its orbit), CME events, and meteor showers, all provide valuable data that can be used to model the lunar exosphere, thereby gaining an understanding of it.

1.2.5. Direct Temperature Measurements

Temperatures discussed in previous sections are all scale height derived while results presented in this thesis are direct temperature measurements. Scale height measurements can be used to infer the gas temperature from the following equation:

$$H = \frac{kT}{Mg} \quad [\text{km}] \quad \text{Eq. 1.1}$$

where H is the scale height, k is the Boltzmann constant, T (K) is the temperature, M is the atomic mass of the species in kg, and g is the surface gravity of the Moon (1.63 m s^{-2}). For a summary of temperatures for sodium from the studies mentioned above, refer to Table 1 in Sarantos et al. (2010). Temperatures in Table 1 (Sarantos et al., 2010) are for sodium observations made above the lunar equator and range from 476 K to 2900 K.

An instrument that can make direct temperature measurements was built and implemented by Ronald J. Oliverson, Fred L. Roesler, and Edwin J. Mierkiewicz. A direct comparison of sodium temperature versus lunar phase angle during the waning phase of the Moon has been presented by Mierkiewicz et al. (2014). A plot from their paper is shown below in Figure 1.7. These are direct temperature measurements (based on the assumption that bulk motion does not widen the line profile), instead of scale height derived temperatures (e.g. Potter et al., 2000). In their study, Mierkiewicz et al. (2014) observed a decrease in temperature from 3260 K near full Moon to 1000 K at a phase angle of 42° . They directly compared this result to scale height derived temperatures obtained by Potter et al. (2000), which also suggested that scale height derived exospheric temperatures for sodium decreased with increasing phase angle. Mierkiewicz et al. (2014) found that their line width derived temperatures at waning phase angles matched the waxing phase temperature results of Potter et al. (2000), but not their waning phase temperatures. Mierkiewicz et al. (2014) also concluded that since their measured exospheric temperatures are larger than expected for sodium atoms thermalized to the lunar surface temperature of approximately 400 K that the source of those exospheric sodium atoms must be due to some other energetic source mechanism such as PSD, which is in agreement with previous work from Sarantos et al. (2010).

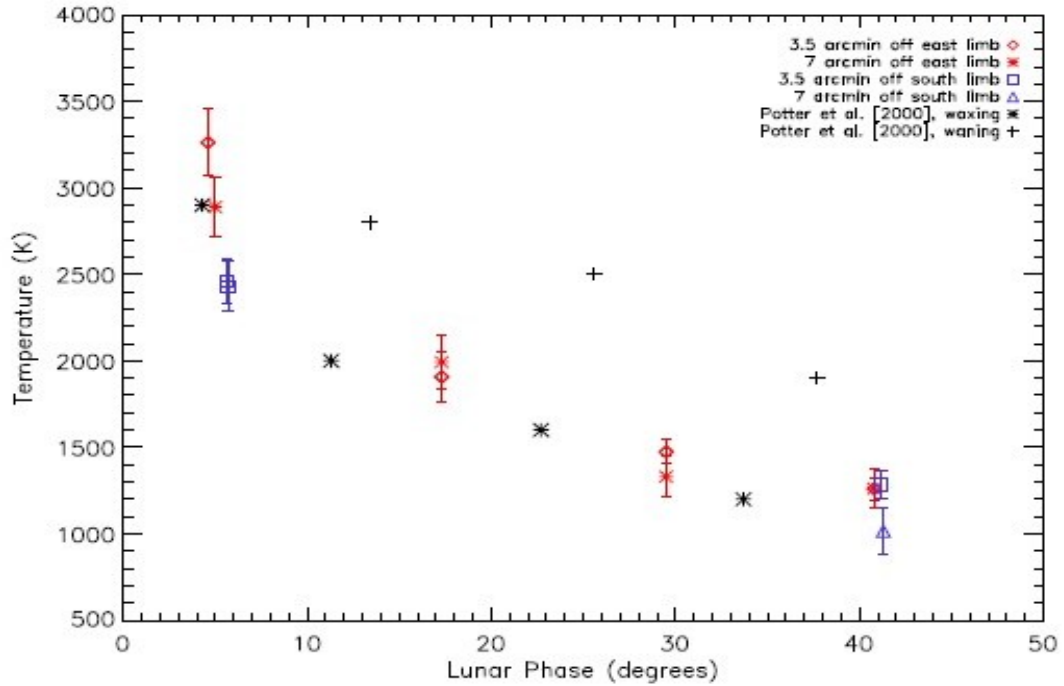


Figure 1.7: Comparison of direct temperature observations made by Mierkiewicz et al. (2014) and those determined by Potter et al. (2000).

1.3. Differences between Exospheric Sodium and Potassium

From Table 1.2 it can be seen that the measured limb brightness of sodium is almost 3 times that of potassium and its scale height is almost twice that of potassium. Clark et al. (1995) provides a brief summary of the differences between potassium and sodium abundances and their implications on the lunar atmosphere. Clark et al. (1995) uses information from a lunar potassium abundance map obtained from the Apollo GRS experiment to explain the variation in surface abundances between sodium and potassium. They report that potassium has a unimodal surface distribution to the first order and the primary high potassium is centered on 5 to 10 degrees west longitude north and south of equator, and covers approximately a quarter of the western side. They also mention that modest increases in potassium are associated with the lunar maria.

1.3.1. Potassium and KREEP

On the selenographic north west quadrant of Figure 1.1, it can be seen that the surface has more maria and is home to a large portion of a mixture of elements. This region is known as K-potassium, REE-rare Earth elements, P- phosphorus (KREEP). KREEP is significant because it contains heat - producing elements such as uranium, which decays into thorium and eventually into potassium. This radioactive decay sequence indicates that regions home to KREEP should have more potassium than the rest of the lunar surface. The Lunar Prospector (LP) Gamma-Ray spectrometer (GRS) found that thorium and potassium are highly concentrated in the western maria region on the nearside and less concentrated in the south pole Aitken basin (Lawrence et al. 1998). A map made by the LP GRS showing high thorium concentrations of the Moon which indicates the locations of KREEP is shown in Figure 1.8. The Kaguya GRS also mapped the global distribution of thorium and found that the western maria in the nearside is more abundant than that in the farside (Hasebe et al., 2008). All these differences in lunar topography and geology can have an effect on the observed potassium and sodium in addition to the variations with phase angle and longitude discussed earlier.

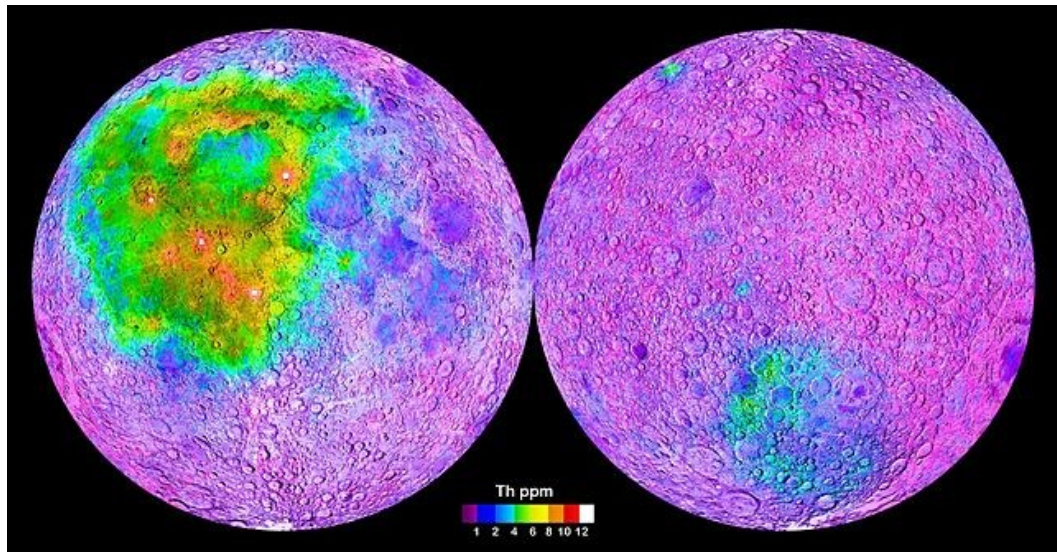


Figure 1.8: Thorium concentrations on the Moon as mapped by the Lunar Prospector with the regions with highest amounts of thorium (KREEP) regions on the near side corresponding to the regions with the most maria in Figure 1.1 (map made by Lunar Prospector).

1.4. Significance of Study

New observations of both sodium and potassium over a wide range of lunar phases and solar cycles will lead to a better understanding of the lunar exosphere, including its source, sink, and escape mechanisms on both short and long timescales. New potassium and sodium observations will further our understanding of the dynamics that govern the lunar SBE and eventually more distant SBEs. As the majority of previous observations emphasized sodium, more potassium observations may also help disentangle different physical processes. For instance, potassium is predominantly found in the KREEP regions and sodium has a more symmetrical distribution.

The results I present in this thesis are from measuring sodium and potassium line profiles and interpreting line width as temperature, whereas all the temperatures discussed earlier were scale height derived. The data presented here are a continuation of the direct temperature measurements made by Mierkiewicz et al. (2014) and Oliverson et al. (2012). My observations span the period from November 2013 to May 2014, with sodium observations made from the lunar limb to up to 1-2 lunar radii away in both the equatorial and high latitude regions. Potassium observations were also made off the limb of the Moon. The data presented in this thesis are unique in that they contain line profile measurements of both potassium and sodium emissions.

CHAPTER 2

2. Telescope and Instrumentation

2.1. Telescope

All observations for my thesis were made from the National Solar Observatory (NSO) McMath-Pierce Solar Telescope (MMP), Kitt Peak, Arizona (Figure 2.1) using the Main telescope, feeding a Fabry-Perot spectrometer (FPS) located at the telescope's north Port.

The NSO MMP facility houses three telescopes, the Main, and the East and West Auxiliaries (Figure 2.2). Each telescope is a three mirror design with the optical layout for all three telescopes shown in Figure 2.3; telescope optical parameters are summarized in Table 2.1. The light from the heliostat (#1 mirror) is bounced down the tunnel onto the #2 mirror, and then reflected about 1.5 degrees below the polar axis to the #3 mirror which then bounces light down into the observing room. The #1 and #3 mirrors are both flat and the #2 mirror is the focusing mirror. The #1 mirrors are located on top of the solar tower approximately 30 m above the ground. The tunnel is over 150 m in length with 60% of it lying below ground, including the observing room. The portion of the tunnel above ground is painted with a special infrared reflective paint (containing titanium particles) and cooled with a glycol-water radiator system to maintain a constant temperature in the tunnel. The #2 mirrors are moved up or down the tunnel to focus each telescope. The #3 mirror of the Main telescope is moved to different ports to feed various instruments within the observing room, while the East and West Auxiliary telescopes have fixed ports (Pierce, 1964).

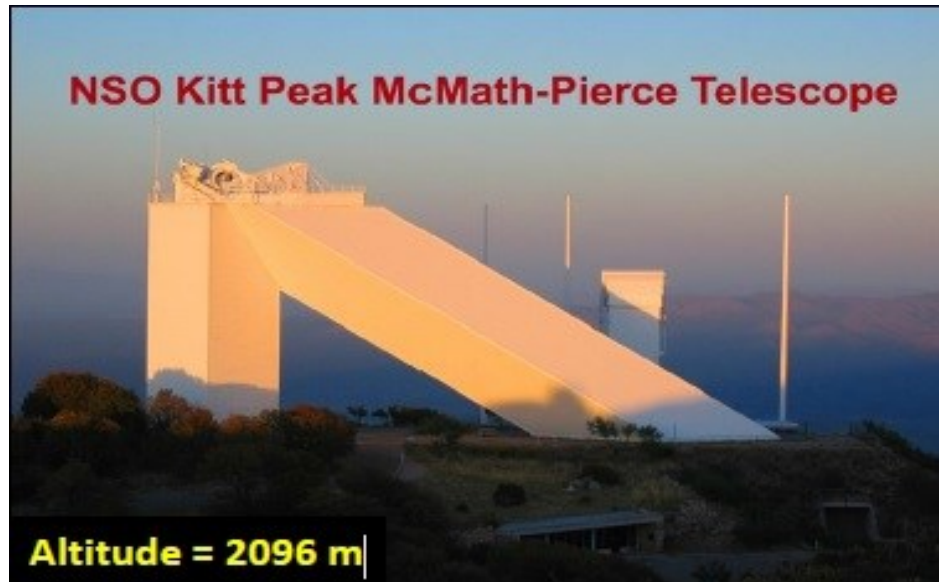


Figure 2.1: The McMath-Pierce Solar Telescope at Kitt Peak, Arizona. The #1 mirrors on top of the solar tower are at an altitude of 2096 m. The entrance to the MMP facility is seen in the bottom center.



Figure 2.2: View of the #1 mirrors for the Main, the East auxiliary, and West auxiliary as seen from inside the telescope, viewing straight up the tunnel. The cover for the #1 mirror is open while the #1 mirror covers are closed for both auxiliary telescopes.

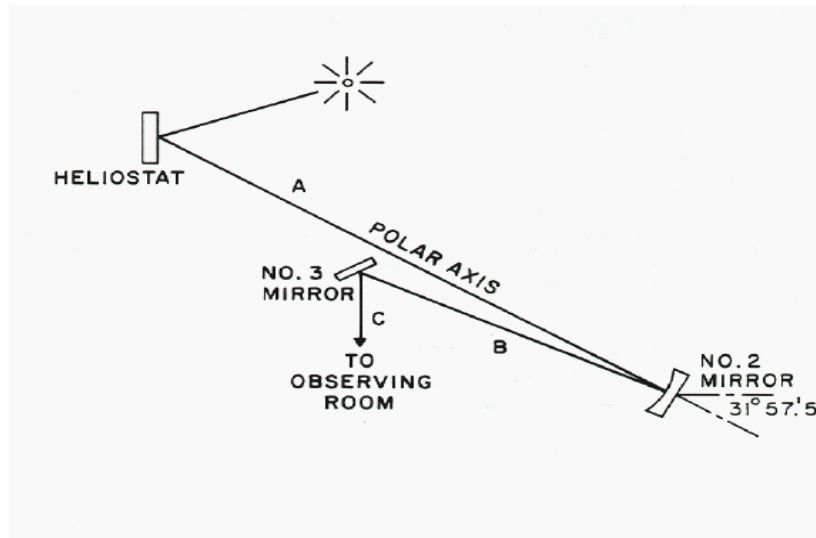


Figure 2.3: Optical layout of three mirror telescope system showing the path of incident and reflected light beam (NOAO/AURA/NSF).

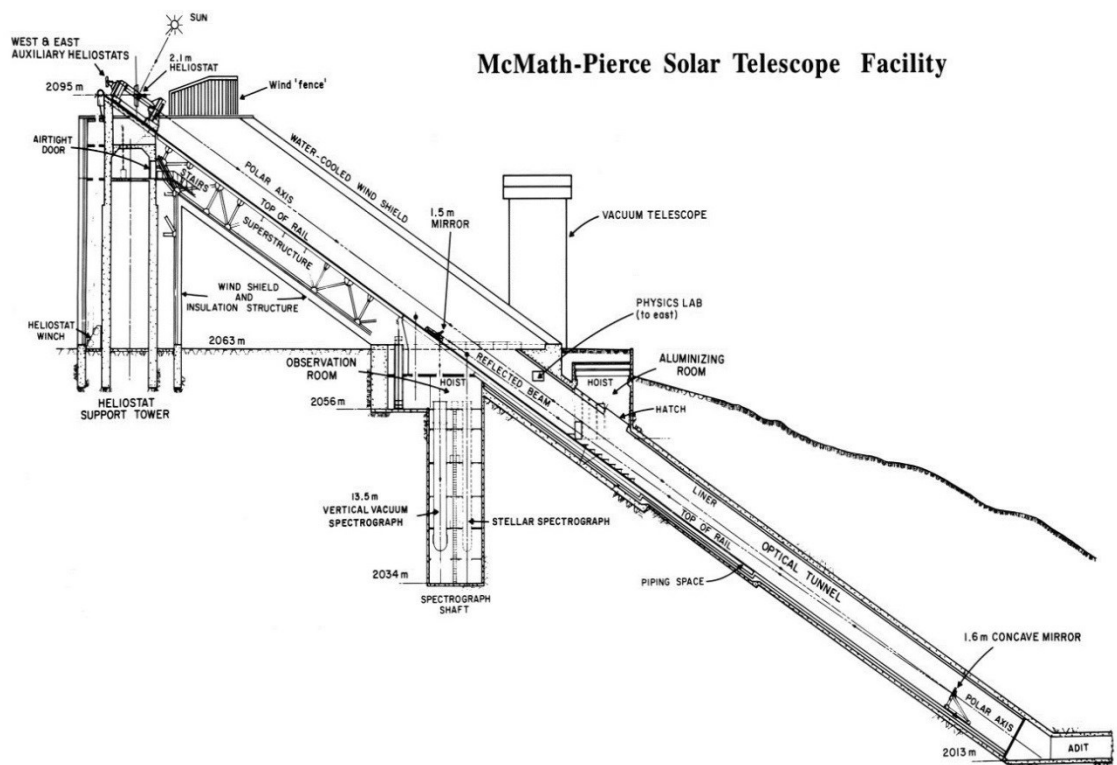


Figure 2.4: Schematic of the McMath-Pierce solar telescope facility showing the 3 mirror system and the path of the reflected beam (NOAO/AURA/NSF).

Table 2.1: Optical parameters of the McMath-Pierce telescope facility as adapted from Pierce (1964) and (NOAO/AURA/NSF).

Telescope	Main	East	West
Normal Distances (m) (refer to Figure 2.3)			
A	136	91	88
B	75	30	27
C	9	9	9
Diameters (m)			
Heliostats (#1 mirror)	2.03	0.91	0.91
#2 mirror	1.6	1.07	0.91
#3 mirror	1.52	0.61	0.91
Clear Aperture	1.6	0.81	0.81
Focal Length(m)	87.0	40.37	35.6
f-ratio	54	50	39
Image Diameter(m)	0.82	0.37	0.33
Plate Scale (arcsec/mm)	2.37	5.11	5.82

2.2. Fabry-Perot Spectrometer (FPS)

The ability to make high spectral resolution observations in studying the lunar sodium and potassium exosphere is possible due to the wide field, high spectral resolution capabilities of the Fabry-Perot spectrometer (Roesler, 1974; Hernandez, 1986; Tufté, 1997). Additionally, using two-dimensional detectors such as charge coupled devices (CCDs) allows all wavelengths within a desired spectral interval to be recorded simultaneously (Coakley et al., 1996).

2.2.1. Fabry-Perot Spectrometers, A Brief Introduction:

The Fabry-Perot spectrometer was designed in the late 19th Century by two French physicists at the University of Marseilles, Alfred Perot and Charles Fabry. The FPS makes use of wave interference phenomena due to multiple wave reflections between two highly parallel, reflective glass plates, with a small space, d , between them (Figure 2.5). The etalon plates are usually made of fused silica with their inside surfaces coated on one side with highly reflective, multi-layer dielectric coatings (Roesler, 1974).

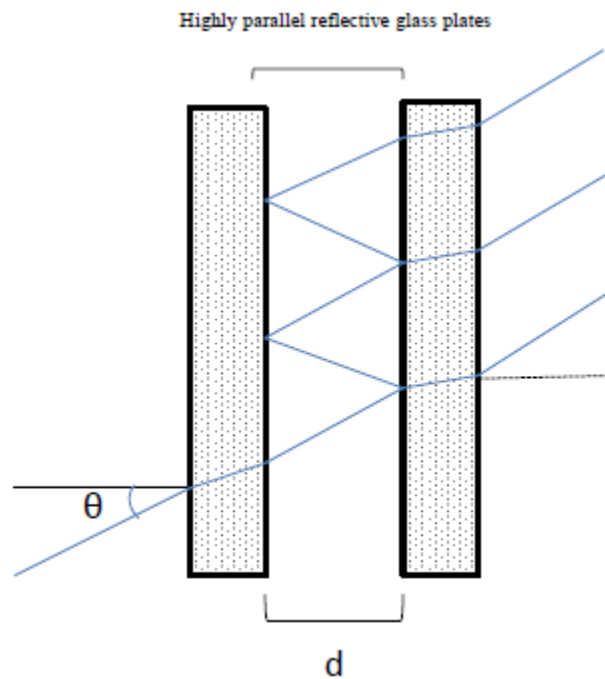


Figure 2.5: Schematic showing multiple wave reflections of an incident light beam within two highly parallel glass plates (etalons).

The interference pattern produced in a FPS is in the form of circular fringes due to the circular symmetry of the system. The condition for constructive interference is given by:

$$2nd\cos\theta_t = m\lambda \quad \text{Eq. 2.1}$$

where m is the order number, λ is the wavelength, n is the refractive index of the gap between the etalons (the refractive index for air is 1), and θ_t is the angle of the transmitted ray. Alternatively, taking σ to be the inverse wavelength in vacuum (i.e. the vacuum wavenumber) the above equation can be written in terms of σ as follows:

$$2nd\sigma\cos\theta_t = m. \quad \text{Eq. 2.2}$$

From equations, 2.1 and 2.2, it can be seen that the Fabry-Perot fringe pattern exhibits periodic behavior, meaning that a single wavenumber appears multiple times at specific angles. Alternatively, multiple wavelengths can be transmitted at a given θ_t , refractive index n , and optical spacing d , each in a different order m . Therefore, it is important to minimize the number of unwanted orders and ideally, limit it to just one order. To accomplish this objective, one must limit the wavelength or wavenumbers to a Free Spectral Range (FSR). The FSR specifies what range of wavenumbers can be observed without having any orders overlap and is the distance between the m^{th} and $(m^{th} + 1)$ order. The change in wavenumber that is necessary to shift the fringe pattern by one fringe or change the order by one unit is defined as the FSR, Q , and is written as follows:

$$Q_\sigma = \frac{1}{2nd}. \quad \text{Eq. 2.3}$$

The resolving power of the Fabry-Perot is the smallest wavelength difference that can be resolved when the distance between two closely spaced, equal intensity emission peaks is equal to their Full-Width Half Maximum (FWHM). Resolving power is written as follows:

$$R = \frac{\lambda}{\Delta\lambda_{FWHM}} = \frac{\sigma}{\Delta\sigma} \quad \text{Eq. 2.4}$$

where $\Delta\lambda_{FWHM}$ is the smallest resolvable wavelength difference.

The actual resolving power of a FPS will be less than the theoretical resolving power, R_o , due to the etalons not being perfectly flat or parallel. A parameter that is closely related to the resolving power, R , is the finesse, N_R , and is defined by the reflectivity. The reflectivity, \mathcal{R} , is a parameter that does not affect FSR but can affect the

sharpness of the interference fringes. Etalons with high reflectivity produce sharp peaks with narrow widths and in the ideal case, the Fabry-Perot etalons would have very high reflectivity and thus would transmit a very sharp image. It is therefore desirable to have etalons with high reflectivity. In reality however, the sharpness of the images is affected by the actual reflectivity of the etalons. The finesse is defined as the ratio of the separation between adjacent bright peaks (maxima) to the FWHM and can be written in terms of the reflectivity as follows:

$$N_R = \pi (\mathcal{R}^{1/2}) / (1 - \mathcal{R}). \quad \text{Eq. 2.5}$$

The finesse of an instrument can also be written as the ratio of the FSR to the FWHM:

$$N_R = \frac{Q}{\Delta\lambda_{FWHM}}. \quad \text{Eq. 2.6}$$

In practice, the finesse is limited by the etalons not being perfectly parallel and flat and also due to the coatings on the etalons not being perfectly flat.

2.3. Fabry-Perot Spectroscopy for the Study of Lunar Exospheric Emissions

Observations of lunar sodium and potassium exospheric emissions at high spectral resolution require an instrument with high signal to noise capabilities, efficient scattered light rejection, high throughput, and a well-defined instrumental profile (IP). The FPS with its wide field capability meets the requirements to investigate the lunar exosphere by measuring sodium and potassium spectral line profiles to determine the temporal and spatial variations of effective temperatures and velocities. The FPS consists of two etalons arranged in series, a combination that results in high spectral purity and contrast by extending the FSR, and suppressing the broad Lorentzian wings of a single etalons transmission function (Roesler, 1974). The second etalon also sharpens the common transmission peak of the two etalon system (Roesler, 1974). All these aspects of a dual etalon FPS helps meet the challenge of accounting for hyperfine structures ($\sim 1 \text{ km s}^{-1}$ line width) in the process of deconvolving observed line profiles, thermal widths ($\sim 1 - 3 \text{ km s}^{-1}$), non-thermal features ($\sim 1 - 3 \text{ km s}^{-1}$), and terrestrial sodium airglow emissions (Mierkiewicz et al., 2014).

The emission lines that are observed for studying the lunar sodium and potassium exosphere are listed in Table 2.2 while the wavelengths of the calibration lamps are listed in Table 2.3. The wavelengths listed in Table 2.3 are the mean wavelengths of the hyperfine sodium and potassium lines. The D2 line for both potassium and sodium is brighter than the D1 line. For a mesospheric terrestrial measurement, the sodium D2 line is brighter than the D1 line by a factor of 1.2 – 1.8 (Slanger et al., 2005) while in the local thermodynamic equilibrium the ratio is 2. Due to an overlap of the potassium D2 line with a strong atmospheric O_2 absorption line (Bleeker and Huber, 2012), the potassium D2 emission is very hard to detect. For this reason, the potassium D1 line was studied instead of the D2 line.

Table 2.2: Table of sodium (Juncar et al., 1981) and potassium emission lines (Fujii and Takashi, 2005) lines.

Emission Line	D1 Wavelength (Å)	D2 Wavelength (Å)
Na	5895.9242	5889.9509
K	7698.9646	7664.8991

Table 2.3: Table of sodium and potassium calibration lamp source lines with their respective wavelengths.

Calibration Source Lines	Wavelength (Å)
Na D2	5889.9509
Th I (Na)	5891.4510
K D1	7698.9646
Th I (K)	7647.3800

2.3.1. UW/GSFC FPS optical layout

The FPS is stationed below the Main #3 mirror at the north Port. A white foam core board at the top of the instrument defines the telescope focal plane. A guide camera is placed in the tunnel, 3.2 m above the instrument, looking down at the focal plane where the Moon is imaged. Light passes through a 3 arcmin entrance aperture, although occasionally the field of view (FOV) was decreased to 1 or 2 arcmin in diameter.

The FPS optical layout and ray tracing diagram are shown in Figure 2.6. The entrance lens, L1 images the #2 mirror (and the #1 mirror) at the iris above field lens L2. Together, L2 and the Fabry-Perot collimating lens, L3 image the sky between the Fabry-Perot etalons. The iris on top of L2 is a pupil stop that is used to assist in the alignment of the telescope and the instrument axes; the iris is also useful as it helps reject stray light. The FPS collimating lens, L3 directs parallel light through narrowband filters and the FP chambers. The camera lens, L4 focuses the parallel beam onto to the CCD (charged coupled device) detector. The lens specifications are found in Table 2.4. It is important to

note that the sky is not imaged onto the detector; instead, the image of the #2 mirror is conjugate with the FP ring pattern at the detector. Figure 2.7 shows a picture of the entire FPS with the front covers removed and a close up picture of the FP chambers.

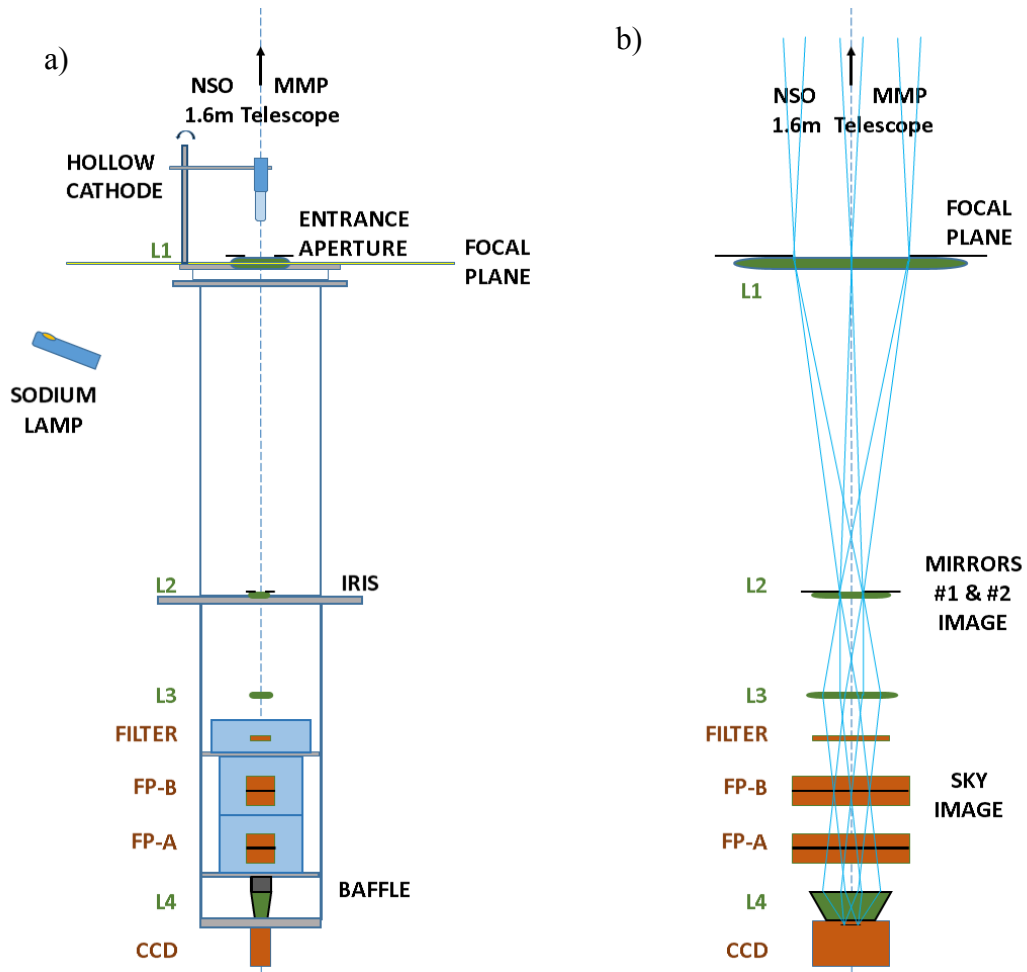


Figure 2.6: (a) Schematic of the FPS showing individual components and the optical axis. (b) Ray tracing diagram with horizontal axis expanded by a factor of 4.

Table 2.4: Table of lens parameters

Lens	Focal Length (mm)	Diameter (mm)
L1 (entrance lens)	762	152.4
L2 (field lens)	750	58
L3 (FP collimating lens)	308	59
L4 (camera lens/ ring imaging lens)	200	50

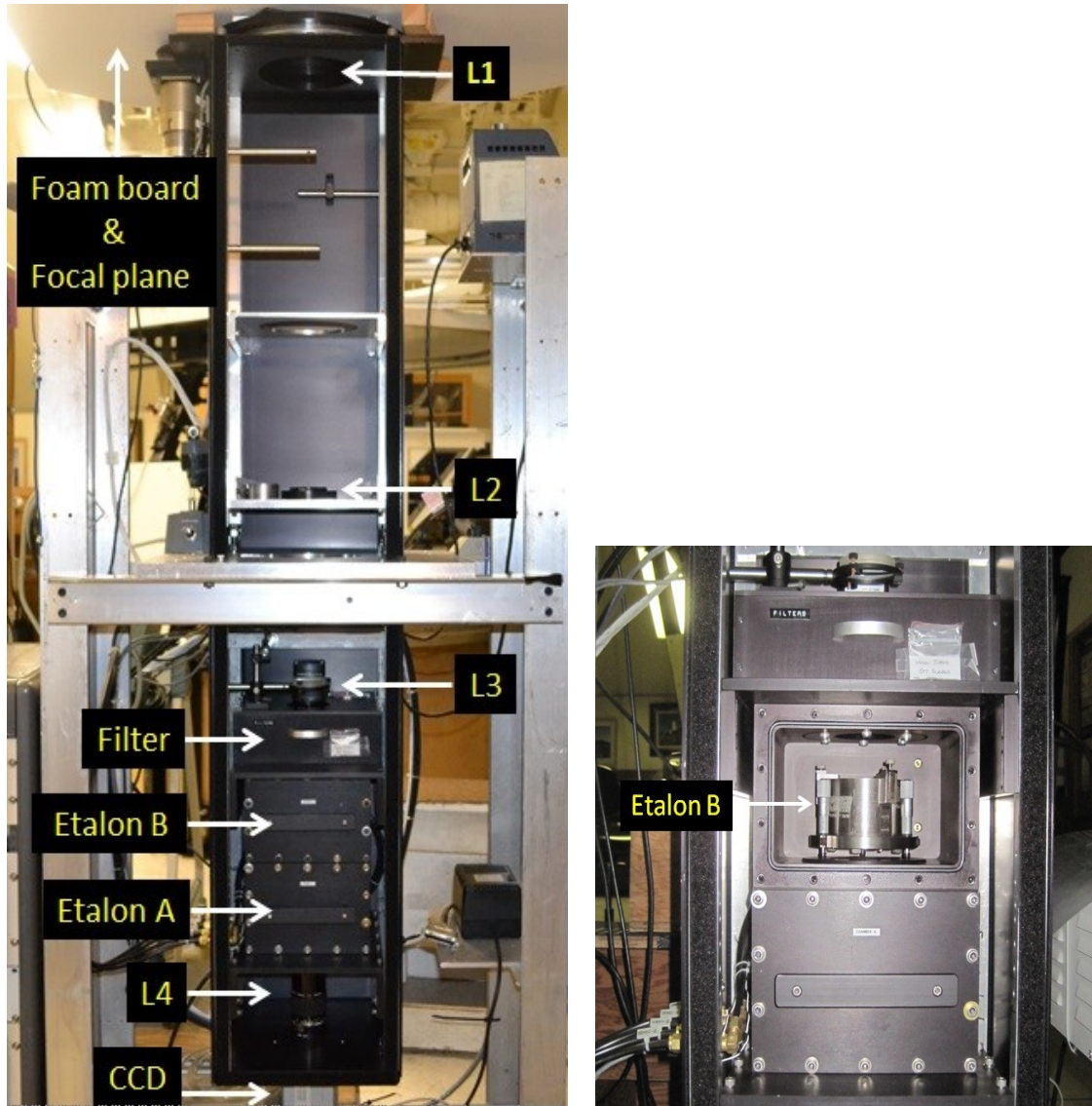


Figure 2.7: The UW/GSFC 50 mm dual etalon FPS situated at the MMP north Port. The FPS etalon is shown with the front covers taken off.

2.3.2. UW/GSFC dual etalon Fabry-Perot

The UW/GSFC dual etalon FPS was built at the University of Wisconsin, Madison to observe the neutral oxygen and carbon emissions of comet Hale-Bopp from the MMP north Port (Oliversen et al., 2012). The FPS was modified to observe the lunar sodium and potassium exosphere by changing etalon spacing and coupling optics. The Fabry-Perot etalon specifications are listed in Table 2.5. The FPS operates in the annular summing mode which allows for the entire spectral range of interest to be imaged onto a CCD camera (Coakley et al., 1996). Table 2.6 summarizes the CCD specifications.

The FP dual etalon spectrometer consists of two etalons made from fused silica with highly reflective (91 ± 1 % near Balmer α 6563 Å) broadband ($\sim 4800 - 9500$ Å) multi-layer dielectric coatings on their interior faces (Mierkiewicz et al., 2014). The higher resolution etalon is A while the lower resolution etalon is B. Specific narrowband filters are used for observing sodium and potassium emissions in order to isolate specific emission lines and minimize the number of adjacent orders being transmitted. The orders passed are wavelength and etalon dependent and are calculated using the following equation

$$\frac{\Delta\sigma}{\sigma} = \frac{\Delta\lambda}{\lambda} \tag{Eq. 2.7}$$

where $Q = \Delta\sigma$.

The number of orders passed by each filter is calculated for etalon A and is summarized in Table 2.7 along with the specifications of the narrowband filters. The narrowband filters are 2 cavity filters and the wavelength coverage listed in Table 2.7 corresponds to the FWHM of the filter.

Table 2.5: Table of parameters for the 50 mm dual etalon Fabry-Perot Spectrometer

FPS parameter		Na	K
Wavelength (Å)		5889.9506 Å	7698.9646 Å
Resolving Power/ Resolution		180,000 (1.7 km/s)	180,000 (1.7 km/s)
Wavelength Coverage (Å)		0.8	1.0
d (cm)	Etalon A	0.4	0.4
	Etalon B	0.176	0.176
Wavenumber FSR (cm ⁻¹)	Etalon A	1.25	1.25
	Etalon B	2.84	2.84
Wavelength FSR (Å)	Etalon A	0.43	0.74
	Etalon B	0.98	1.68
Field of View (FOV)		3 arcmin **	3 arcmin **
Annular Summing Mode		0.3097 km/s/bin	0.3097 km/s/bin
Spectral Bin Size			

** 3 Arcmin FOV is approximately 336 km at a mean lunar distance of 384,400 km (variable by $\pm 7\%$). Occasionally a FOV of 2 arcmin was used.

Table 2.6: Table of parameters for CCD detector

CCD Parameter	
Detector	Andor 912BV
Array size	512 x 512
Pixel Size	24 μm
Shift Speed	44.975
Read Rate	50 kHz
Temperature (Camera)	-80 ° C (Water cooled)
File Format	FITS unsigned 16-bit image

Table 2.7: Table of parameters for narrowband filters

Filter Name	Center Wavelength (\AA)	Bandpass (\AA)	Orders passed (Etalon A)
Na D2 (ANDV11321)	5890	4	9
H-alpha (ANDV13296)	6563	5.5	10
Th I (ANDV13404)	7647	5.5	7
K D1 (ANDV13173)	7699	5.5	7

It is important to note, unwanted light will still appear in each FPS image in the form of ghosts, reflected ring features, and stray light. There are different types of ghosts and one such family belongs to light from suppressed orders getting through and appearing in an image. Table 2.7 shows the number of orders passed for Na and K from their respective narrowband filters. The orders passed are etalon dependent, and the orders shown in Table 2.7 are calculated for the high resolution etalon. For instance, nine orders are passed by the sodium narrowband filter which means that ghosts from up to nine suppressed orders can appear in an image. The high resolution etalon passes more orders than the low resolution etalon. The ratio of orders passed for etalon A and etalon B is in a 4/1.76 ratio. Another family of ghosts arises due to reflections between multiple surfaces within the FP such as reflections off the back part of the etalons, reflection

between the etalons, reflections off the narrowband filter surface etc. These ghosts are symmetric about the optical axis and can be mitigated by making the outside surfaces (uncoated) of the etalons to be slightly wedged in order to move the ghosts away from the optical axis to make off-axis ghosts.

2.4. Focus and Collimation

As its name implies, the MMP Main is often used during the day to study the sun. After the solar astronomer is finished, typically mid-afternoon, the #3 mirror is moved to the north Port, the location of our FPS. This also required the #2 mirror to be moved about 5m up the tunnel for focus and to adjust the tip/tilt (collimation) of the #2 and #3 mirrors in order to align the telescope axis with the FP optical axis. The focus is usually adjusted on the sun by focusing sunspots on the white foam card, but if done at night, the craters on the Moon are used. The telescope collimation is accomplished by looking at the image of the #2 and #1 mirrors at the instrument pupil stop (located at L2). After removing the iris and L2 lens, the image of the #2 mirror is centered at the L2 position (Figure 2.6) using a high precision centering template (i.e., circular paper with a ~0.5 mm aperture) to define the optical axis by adjusting the tip/tilt of the #3 mirror. The #1 mirror was pointed at a declination above 0° to give a foreshortened view of the #1 mirror allowing one to see the #1 mirror yoke as viewed by the #2 mirror. The tip/tilt of the #2 mirror is adjusted to make the yoke appear symmetric on both sides of the image. To check the alignment and field rotation, the telescope is moved several hours in hour angle and the collimation is tweaked if necessary to make sure the initial symmetry of the image is retained. The iris is adjusted to fit the pupil size and location when collimation is done. The collimation can also be tweaked at night, by looking at the Moon and ensuring the illumination of the mirrors are symmetric.

2.5. Pressure Tuning and Ring Radius

Pressure tuning is done to correctly align the transmission peaks of the two etalons at specific wavelengths. The etalons are housed in individual chambers, filled with dry nitrogen. By adjusting the pressure of an etalon in the FP chamber, the wavelength transmitted at a particular angle can be altered. This procedure is called tuning. Each FP etalon is ‘tuned’ using standard emission line calibration sources. Figure 2.8 shows an image of the calibration sources. Figure 2.9 shows a raw ring image of the sodium calibration lamp emission.

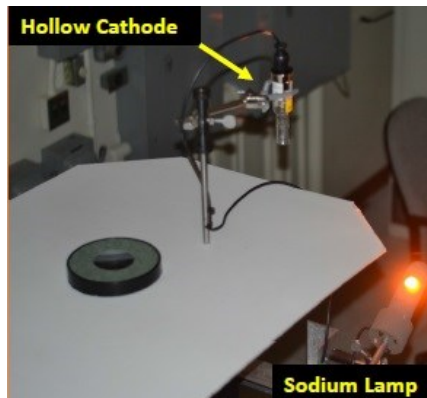


Figure 2.8: Calibration setup showing white foam board at the focal plane. The sodium “Gates” lamp (orange lamp at the bottom) reflects light off a card covering the ceiling port for wavelength calibration. The hollow cathode lamp with a diffuser is placed over the aperture for instrumental profile and stability measurements.

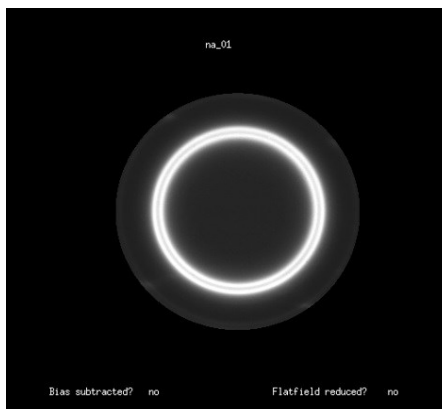


Figure 2.9: A raw FPS ring image of the sodium calibration lamp. Integration time: 10 seconds, date: February 19. (filename: na_01.fits).

For a given wavelength, etalon A is set at a pressure that determines the correct ring radius (angle); in terms of wavelength, we place the wavelength of interest in the middle of the spectral window. Etalon B is adjusted to match the radius (angle) of etalon A. This is done by adjusting the optical distance (nd) of etalon B by varying the pressure of the nitrogen gas between the plates. By determining the required pressures for etalon A and etalon B for a specific wavelength, the transmission peaks from each etalon can be correctly aligned.

The Fabry-Perot interference fringe pattern wavelength varies as radius squared (r^2). Therefore, operating in the FP annular summing mode makes use of the fact that equal area annuli correspond to equal spectral intervals.

Using Equation 2.2 and rearranging to get, $\frac{m}{2nd} = \sigma \cos \theta_t$, and assuming $n = 1$, $\theta = 0$ and $\sigma = \sigma_o$, we have

$$\sigma_o = \sigma \cos \theta_t. \quad \text{Eq. 2.8}$$

For small angles ($\cos \theta = 1 - \left(\frac{\theta^2}{2}\right)$), the wavenumber range $\Delta\sigma$ from the axis out to angle θ_t can be written as follows:

$$\frac{\Delta\sigma}{\sigma} = \frac{\sigma - \sigma_o}{\sigma} = \frac{\theta_t^2}{2}. \quad \text{Eq. 2.9}$$

As seen from equation 2.9, the wavelength varies with the square of the radius as

$$r = f_{\text{camera}} * \theta \quad \text{Eq.2.10}$$

where r is the radius on the CCD, f_{camera} is the focal length of the camera, and θ is the angle.

2.6. Dispersion

The spectral dispersion (velocity per spectral bin) is constant in velocity space or wavenumber. The instrument dispersion was determined by finding A and B pressures which included both sodium and thorium lines in the same order. The dispersion is calculated using the centroid (position in bins) of the thorium line and the sodium self-reversal feature.

The dispersion is given by:

$$\frac{\Delta\lambda'}{\lambda} = \frac{Th(\text{\AA}) - Na(\text{\AA})}{\Delta bins} \quad \text{Eq.2.11}$$

Using the relation,

$$\frac{\Delta\lambda'}{\lambda} = \frac{Velocity' \left(\frac{km}{s} \right)}{c}$$

we can get the following equation:

$$Velocity' = \frac{\Delta\lambda' * c}{Na(\text{\AA})} \quad \text{Eq.2.12}$$

where, $c = 299,729 \text{ km s}^{-1}$, $Th = 5891.451 \text{ \AA}$, $Na = 5889.9509 \text{ \AA}$. The prime indicates per bin.

The average dispersion was calculated from 5 measurements taken in March 2012, April 2014, and May 2014. The dispersion values calculated 2 years apart show that the dispersion was stable. A sample spectrum used to calculate the dispersion is shown in Figure 2.9. The average dispersion value is $0.3097 \pm 0.0006 \text{ km/s/bin}$. Note that ghosts are visible in Figure 2.10 due to the blocking filters transmitting some adjacent orders. In addition, an argon line at 5888.584 \AA is also present in the spectrum. These ghosts had to be fit in order to properly fit the entire dispersion spectrum. I will discuss the fitting methodology I used for the sodium data reduction in Chapter 4.

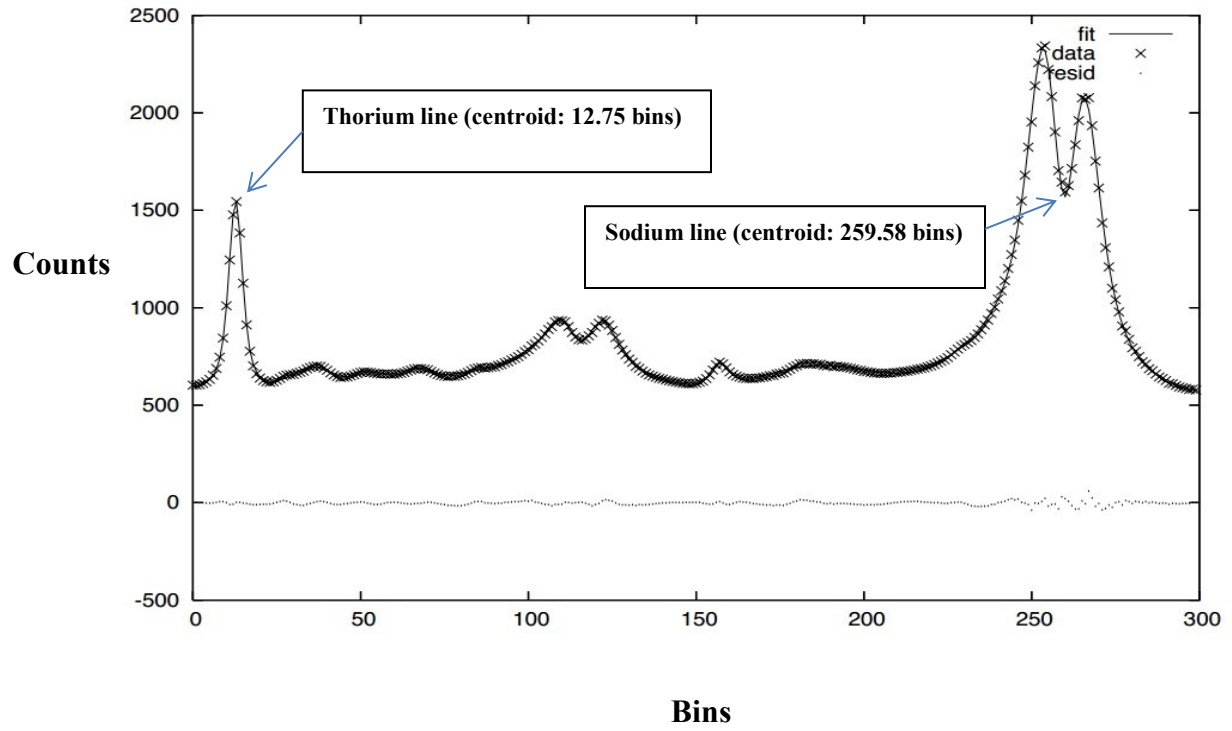


Figure 2.10: ThNa spectrum with fit for March 2012. This spectrum was used to determine the position of the Th I line and the Na self-reversal centroid in order to calculate the dispersion. The same was done in April 2014.

CHAPTER 3

3. Observations

The sodium and potassium observations for this thesis were conducted monthly from November 2013 to May 2014, with the exception of March 2014. I was directly involved in each of these six observing runs, with observing support from (in alphabetical order): Nick Derr, Chad Freer, Maggie Gallant, Edwin Mierkiewicz, Ron Oliverson, Sara Rosborough, Lori Spalsbury, Maurice Wilson.

A summary of the data collected is shown in Table 3.1; for a complete listing of all observations used in this thesis, refer to Appendix A. All data are concurrent with the LADEE mission instrument testing and science phase. The LADEE mission was launched on September 7, 2013 (UTC) and entered into lunar orbit on October 6, 2013 (UTC). The mission had a 128 day science phase and ended in a planned crash onto the far side of the moon on April 18, 2014 (UTC).

Table 3.1: Summary of data runs

Month	Year	Run	Nights with Data	Full Moon Date
November	2013	11/16 – 11/22	3	November 17
December	2013	12/13 – 12/20	6	December 17
January	2014	01/10 – 01/21	11	January 16
February	2014	02/11 – 02/22	8	February 14
April	2014	04/14 – 04/22	7	April 15
May	2014	05/09 – 05/20	10	May 14

Observations were made off the limb of the Moon, moving from selected craters in one of the four cardinal directions. The field of view (FOV) was positioned from tangent to limb out to 2 lunar radii. Additionally, observations were also taken on the central highlands, (near Moon center) and on the sky background (Section 3.2.2). A typical observing run is held during a full Moon period, spanning 7-11 days. Observations are made pre-magnetotail (waxing) passage, during magnetotail passage (full) where the Moon spends 5-6 days inside the magnetotail (phase angle less than 40°), and post-magnetotail passage (waning). During the April 2014 observing run, the full Moon observations coincided with a lunar eclipse.

3.1. Observational Setup

A typical night's setup involved adjusting the telescope focus and collimation as needed, Fabry-Perot tuning, and wavelength calibrations. The main telescope is slewed to the Moon either manually or using the telescope 'preset' command, however, final acquisition may require looking back up the telescope axis and moving the Moon to the North Port. The image of the Moon, as seen in Figure 3.1, is projected onto the white foam board on top of the instrument.

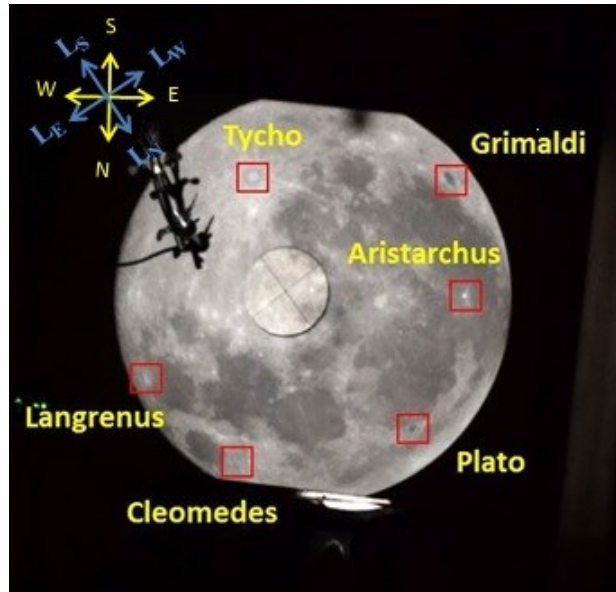


Figure 3.1: Image of the Moon as projected on top of instrument. All major craters used for observations are labeled. The telescope coordinates are depicted by the yellow arrows. The selenographic coordinates are depicted by the blue arrows where the east and west directions are laterally reversed. Both coordinate systems rotate as a function of telescope hour angle (HA). The cross hairs are used for centering on desired locations on the Moon and help the observer to guide the telescope.

3.2. Observing Methodology

Building on the work of Mierkiewicz et al. (2014), my sodium and potassium observations were made off the lunar limb with a 3 arcmin FOV; a small number of observations with a 2 arcmin FOV were also made. Initially the telescope was centered on one of six easily identifiable craters (refer to Figure 3.1) and then moved in a cardinal direction to the lunar limb. Several observations were then made off the chosen limb in a sequence of offsets in Right Ascension (RA) or Declination (Dec). All observations were made with the telescope tracking at the lunar rate.

Most of these observations were made off the sunlit side of the moon, but occasionally near the time of full Moon observations were also made off the terminator.

It is important to note that the east/west references are made with respect to geographic coordinates. In selenographic coordinates, the west limb as observed from Earth is the Moon's east longitude and vice versa.

Sodium observations were made at the respective Fabry-Perot etalon A and B pressures, sodium filter, and CCD camera focus set at infinity. Potassium observations were made in a similar fashion but with potassium specific pressures, filter, and camera focus.

3.2.1. Observational Sequence, Drift, and Telescope Guiding

A typical observing sequence would begin by moving the telescope via the computer controlled 'preset' command, allowing the telescope to slew to the general vicinity of the Moon. Final acquisition and setup was accomplished by manually moving the telescope. A guide camera, mounted in the tunnel above the north Port, aided in tracking during exposures.

Once centered on a particular crater (using a 7 arcmin centering disk), the telescope was then moved in a cardinal direction to the limb and finally to a specific offset location from the limb. Table 3.2 lists the centering craters and subsequent directions of telescope motion. As indicated in Table 3.2, offsets were made up to 1 minute (occasionally 2 minutes) off the equatorial limbs (east or west). Offsets off the high latitude/polar regions go out to 10.5 arcmin. Figure 3.2 shows an example of the FOV with the lunar limb at edge of field lens, east of the Aristarchus crater.

Table 3.2: Table of major and minor craters used for observations, their positions, and telescope offsets by region.

Crater	Region	Coordinates (° Latitude, ° Longitude)
Grimaldi	Equatorial	68.3 W , 5.5 S
Aristarchus	Equatorial	47.4 W , 23.7 N
Copernicus	Equatorial	20.0 W , 9.7 N
Tycho	High Latitude	11.1 W , 43.4 S
Plato	High Latitude	9.3 W , 51.6 N
Langrenus	Equatorial	61.1 E , 8.9 S
Taruntius	Equatorial	46.5 E , 5.6 N
Petavius	Equatorial	60.4 E , 25.3 N
Cleomedes	Equatorial	55.5 E , 39.2 N
Messala	Equatorial	59.9 E , 39.2 N
Offsets for equatorial craters (RA: Seconds/minutes of time)	1.5 arcmin*, 3.4 arcmin** , 28 seconds, 42 seconds, 1 minute, 2 minute***	
Offsets for high latitude craters	1.5 arcmin, 3.4 arcmin, 7.5 arcmin, 10.5 arcmin	

* FOV at limb

** FOV at field lens edge

*** 120 seconds was used occasionally if emissions were significantly strong.



Figure 3.2: The 3 arcmin entrance aperture of the instrument is shown positioned at the limb east of Aristarchus crater. The image is a nonlinear sketch that shows the aperture mask and Moon. The centering disk with the cross hairs is not shown here but during an observation taken off the Aristarchus crater it would be positioned on Plato or Grimaldi for guiding. The hollow cathode assembly is seen in the upper left quadrant.

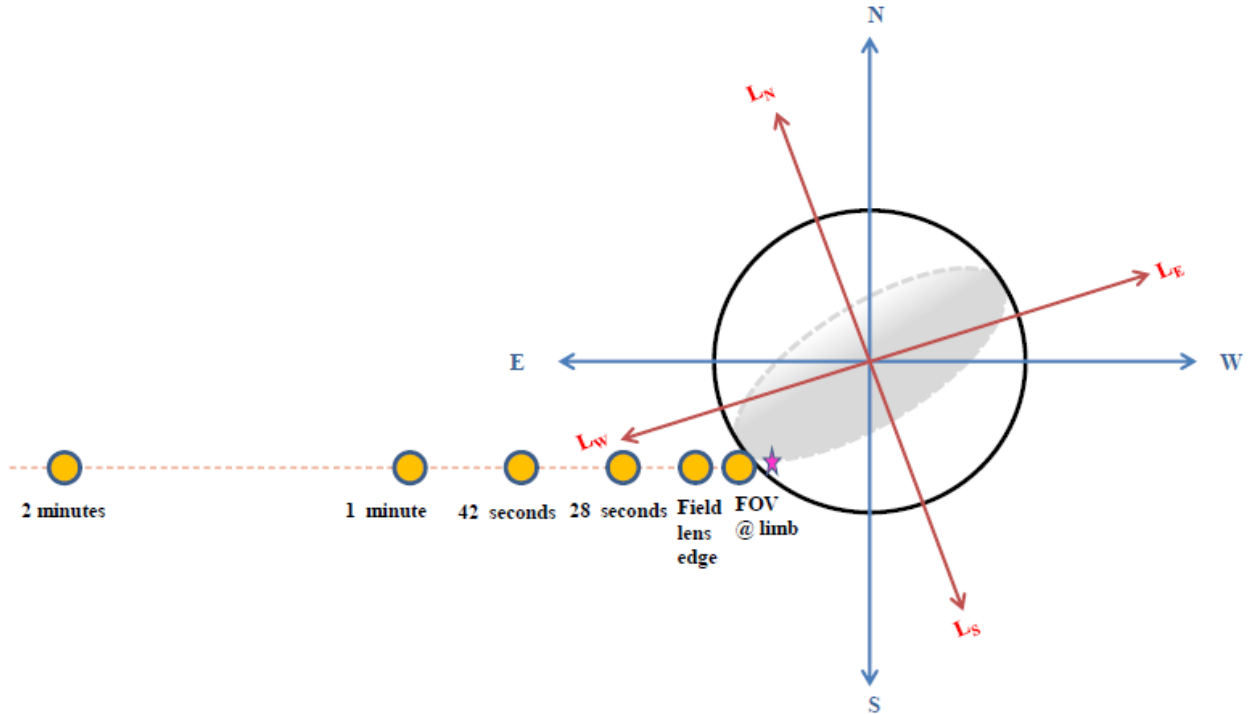


Figure 3.3: Schematic of observations, with different offsets, made off the Grimaldi limb (pink star denotes Grimaldi crater) on the selenographic west limb of the Moon.

As seen in Figure 3.3, once centered on Grimaldi, the telescope is offset in RA to the limb and an exposure is taken. The procedure is repeated for each additional offset. A typical sequence of observations made off of an Equatorial limb follows the offsets listed in Table 3.2 and depicted in Figure 3.3. Observations made at the field lens edge are 3.44 arcmin FOV from the limb. The field lens diameter is 6 7/8 inches and the telescope plate scale is 1 arcmin / inch. The telescope is centered back on the crater before each offset. Note that the offsets east or west are in seconds and minutes of time while observations made off the north and south limbs are declination offsets in arcseconds and arcmin. The conversion from arc seconds to seconds of time and vice versa is given by:

$$\text{Arcsec} = (\text{seconds of time}) * 15 * \cos(\text{Dec}) \quad \text{Eq.3.1}$$

$$\text{Arcmin} = (\text{minutes of time}) * 15 * \cos(\text{Dec}) \quad \text{Eq.3.2}$$

There are two types of motion that are introduced when observing on the Moon. First, the 23° tilt between the celestial and the ecliptic coordinates introduces a sampling variation in latitude. The 5° angle between the ecliptic and the lunar equator also introduces a sampling variation in lunar latitude, but to a lesser extent. Therefore, craters near the lunar limb are chosen to minimize the latitudinal drift during offsets. Second, the ~13°/day (~0.55 °/hr) eastward motion of the Moon must be tracked. This latter type of motion is compensated by the telescope tracking rates (thumbwheel adjustments). The remaining differential motion is compensated by using a guide crater to adjust the telescope.

Once the telescope has been moved in RA or Dec to the desired offset location, the cross hairs, as seen in Figure 3.1, are placed on a chosen guide crater. A guide crater is usually a small bright spot or crater on the Moon that is easy to guide on. In certain situations where the major offset craters are not visible due to the phase of the Moon, , another offset crater close to the terminator is chosen. When an observation is made off the terminator, offsets are made directly off the crater. Some craters that have been used include Messala, Petavius, Copernicus, and Taruntis. These minor offset craters are also used to make observations to increase latitudinal coverage.

3.2.2. Sky Background

After each lunar observing sequence, a sodium sky background is usually taken. Figure 3.4 shows a raw sky background image for sodium; a corresponding ring-summed spectrum can be found in Chapter 4. After the sky background, a thorium scan is taken and the observing room temperature and the humidity are noted. The sodium sky background is usually taken 40 minutes east or west of the Moon center and is a 5 or 10 minute exposure. Terrestrial sodium can be a source of contamination (Chapter 4) for observations made at one lunar radius or more away from the lunar limb. The intensity of the terrestrial sodium nightglow varies seasonally and nightly. The terrestrial sodium emission can vary by up to a factor of two nightly and even seasonally (Gardner et al., 1986; Marsh et al., 2013; Alan Liu, private communication). The sodium nightglow layer peaks at an altitude of 90 ± 5 km. The source of these sodium atoms is ablation of tonnes of interplanetary dust that enters Earth's atmosphere daily (Slanger et al., 2005). Other sources could be volcanic dusts and particles from the oceans (Umberto, 2002). The terrestrial potassium layer is collocated with the sodium at $90 \text{ km} \pm 10 \text{ km}$. The potassium to sodium ratio is about 1%, and as such, the terrestrial potassium glow is considerably weaker and is not detected in sky background observations.

The next chapter will focus on the analysis of the data collected through the observation methodology discussed in this chapter.

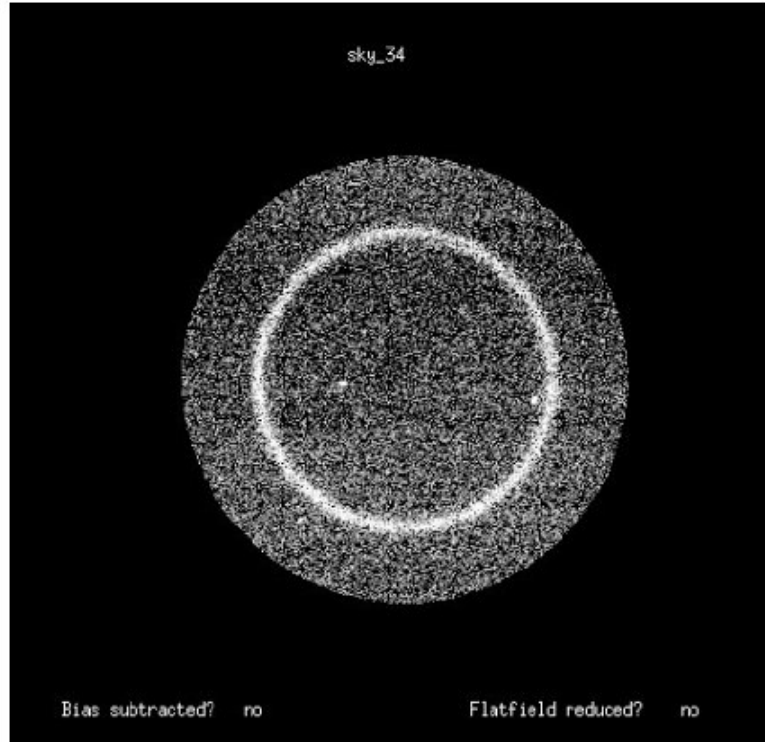


Figure 3.4: Sodium sky background raw Fabry-Perot image. The ‘bright’ (nonlinear contrast stretch) central fringe is the terrestrial sodium glow. Date taken: May16, 2014, integration time: 300 seconds. (filename: sky_34.fits).

CHAPTER 4

4. Data Reduction

The sodium and potassium data are reduced in the Interactive Data Language (IDL) and the normal data reduction steps include: (1) bias subtraction, (2) flat-field correction, (3) instrumental profile (IP) creation, and (4) data fitting. The Andor CCD camera operates in a mode with a “baseline” clamp, where the bias is automatically removed at the end of each exposure. A constant DC offset of 300 is added by this mode, which is removed during the data reduction.

An internal flat-field (diffusely illuminated screen placed 2.4 m above the instrument focal plane) does not adequately represent light coming from the telescope, especially due to the highly reflective #1 mirror support structure scattering light into the main beam. Dome flats are not possible due to the solar telescope’s unique design. Sky flats cannot be used due to spectral signatures in the sky and due to the sky illuminating the reflective support structure from all directions. We found the internal flat-field correction to overcorrect at increasing ring radii, leading to a systematic error and thus data are not flat-field corrected.

An IDL summing code is used to convert FP ring images into 1-D spectra. The 1-D spectra are then fit with a multi - component model (Section 4.2) using the nonlinear least squares fitting code, VoigtFit, of R.C. Woodward (private communication).

4.1. Fabry-Perot CCD Annular Summing Technique and Code

Annular summing makes use of the property that equal area annuli in a Fabry-Perot ring pattern correspond to equal spectral intervals. This property, and its direct relation to the condition for constructive interference for a Fabry-Perot, is discussed in Chapter 2. The basic idea is that by averaging the pixels in an annulus with a specific radius (i.e. angle) from the center of the ring pattern, the raw FP ring image can be disassembled and reassembled into a 1-D spectrum.

The following equations, as shown by Coakley et al. (1996), detail the annular summing technique. The outer angular radius for the Nth annulus in a ring pattern is given by

$$\theta_N = (\sqrt{N})\theta_1 \quad \text{Eq. 4.1}$$

where θ_1 is the outer angular radius for the first element and θ_N is the outer angular radius for the Nth element on the FP fringe pattern. Likewise, for $r = f_{\text{camera}} * \theta$ the outer radius of the Nth annulus on the CCD is given by

$$r_N = (\sqrt{N})r_1 \quad \text{Eq. 4.2}$$

where r_1 is the radius of the pixel that marks the central spot of the fringe pattern. For all data presented in this thesis r_1 is 12. For this value of r_1 , a total number of data points of 136 data points are in the ringsummed spectra.

The ring summing code determines the radial distance of the center of each pixel from the ring center of the FP ring image. The ring center is determined from calibration rings by finding which x and y coordinates produce a peak with the highest intensity and the narrowest FWHM (Full Width Half-Maximum). Each of these pixels is then sorted into the appropriate spectral bins, where each bin corresponds to an equal area spectral interval. The intensity is summed per bin and each bin is then divided by the number of pixels used in the sum (Coakley et al., 1996). This corrects any slight difference in the number of pixels in each annulus. From Equations 4.1 and 4.2, the average number of pixels per given bin can be written as πr_1^2 .

Figure 4.1 shows a raw FP ring image for a Th I scan. Note that Figure 4.1 contains the Th I emission (seen as the bright circle) and ghosts in the form of fainter rings. The FP ghosts appear due to the Th I line being transmitted in unwanted orders of both etalons and other emission lines being transmitted through the order sorting filters. In this case, the most probable other lines are an Ar I line at 5888.591 Å and a weaker Th I line at 5889.953 Å. The Ar I line is a result of the fill argon gas in the HC lamp becoming excited. In addition, the Th I line is also seen in other orders due to the close proximity of the next order (only 0.43 Å away in Etalon A). Figure 4.2 shows its corresponding ring summed 1-D spectrum.

The ring summing code (originally written by Edwin J. Mierkiewicz and later modified by Nick J. Derr) also performs a filtering routine that removes any hot pixels using a 3-sigma filter. For each equal area bin, any pixel with a count rate of 3-sigma away from the average pixel value of the bin is removed. This filtering routine is performed 4 times, after which the average value per equal area bin is plotted as a function of bin number in order to obtain a 1-D spectrum.

An important consideration related to the pixel to bin assignment and spacing of the annuli in the fringe pattern is digitization. A Fabry-Perot fringe pattern has concentric fringe patterns that grow closer when going further out from the central spot due to the radius squared relationship to wavelength. Since the outer rings are closer to each other, it is possible for multiple rings to pass through a single pixel. However, the pixel will only be assigned to closest ring or bin. The consequence of this is digitalization resulting in increased noise due to sampling fewer pixels and a decrease in spectral resolution at large ring radii. A r_1 value of 12 was chosen in order to increase the sampling space and thus increase the average number of pixels per bin, which in turn reduces the effects of digitalization. For an elaborate discussion on the Fabry-Perot CCD annular summing technique refer to Coakley et al. (1996).

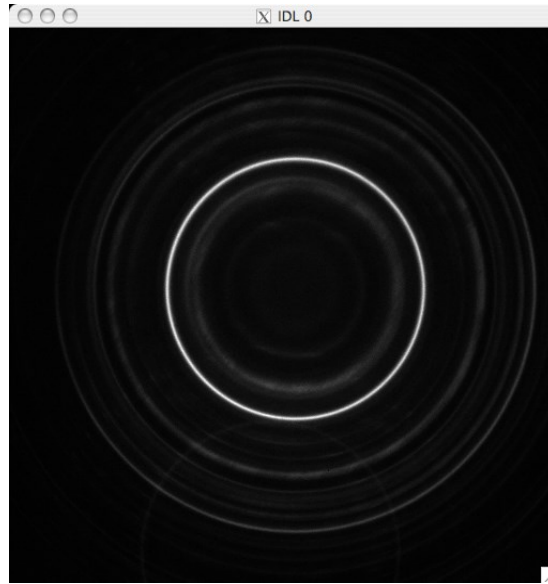


Figure 4.1: Thorium hollow cathode lamp fringe pattern with the bright central fringe representing the Th I line at 5891.451 \AA . Date: February 19, 2014 , integration time: 30 seconds. (filename: th_02.fits).

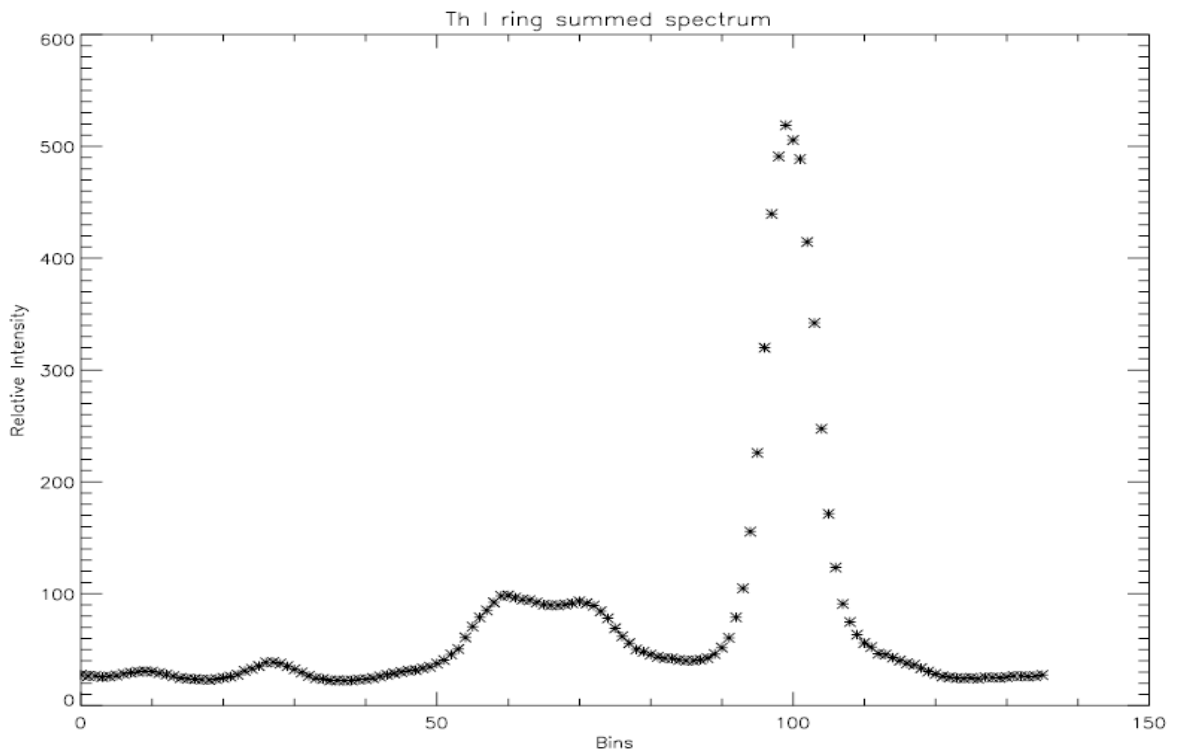


Figure 4.2: Ring-summed spectra of the ring image shown in Figure 4.1. The large peak is the strong Th I line at 5891.451 \AA while the smaller, weaker peaks are the ghosts.

4.1.1. Camera Focus

From January 2014 – May 2014, the CCD camera focus was changed between sodium and potassium images. This change in focus had not been done for previous measurements. A suspicion that the spectral resolution should be higher at potassium wavelengths lead to a study that ultimately determined that a change in camera focus narrowed the potassium instrumental profile FWHM by about $\sim 20\%$. A typical camera lens is designed to be confocal in the visible light region ($4000 - 7000 \text{ \AA}$) while the potassium wavelength (7698.9647 \AA) lies outside this range. The system was initially designed to have the camera lens (L4) set at infinity for sodium (5889.9509 \AA) and for this reason the width of the K IP is slightly larger when the camera lens was not set at the potassium focus. The potassium focus was determined by measuring the FWHM of the Th I line at 7647 \AA over a range of the camera focus values. Once the correct potassium focus was determined, all new data was taken at this new focus. Sodium results are only compared to the potassium data taken at the correct focus.

The focus is changed when switching from observing in sodium (Na D2, Th I (Na)) to potassium (K D1, Th I (K)) or vice versa. Additionally, every time the focus is changed, the ring center for the sodium or the potassium calibration images differ slightly from the ring center value prior to focus change. The appropriate updated ring center is used when doing the ring sum to create the 1-D spectra.

4.2. Instrumental Profile (IP)

Any spectrometer will mark observations with its distinct spectral signature known as the instrumental profile, $I(\lambda)$. The IP is a measure of the response of the instrument to a δ -function input spectrum. Practically, the function input is a narrow spectral line with an intrinsic width which is much narrower than the spectral resolution of the instrument. When a light source is viewed through an instrument, the resulting spectrum is the convolution of the IP, $I(\lambda)$, and the source spectrum, $f(\lambda)$, as follows:

$$F(\lambda) = [f(\lambda) * I(\lambda)]. \quad \text{Eq. 4.3}$$

It is, in theory, possible to deconvolve a well-known IP using Fourier Transforms but this method is complicated and very sensitive to noise. In VoigtFit, a convolution of the model and its derivatives with the IP is performed in order to fit the convolved model to the data (R. C. Woodward, private communication).

4.2.1. IP construction

The narrow line used for empirically determining the sodium IP is the Th I line at 5891.451 Å, obtained by using a Thorium Hollow-Cathode (HC) lamp. A HC lamp consists of an anode, a cathode, and a fill gas (usually a noble gas, in this case, argon). HC lamps operate by applying a high voltage between the anode and the cathode causing the fill gas to become ionized. The ions in the plasma are then accelerated towards the cathode causing atoms to sputter off the thorium cathode. These atoms are excited due to collisions with other atoms and ions in the plasma. The decay from their excited states is very rapid. The HC lamp excitation mechanism and the large atomic mass of thorium (236 amu) greatly reduce the effects of thermal broadening. In this case, the intrinsic thorium line width is much, much smaller than the FPS instrument resolution. Another advantage of using thorium is the large number of visible and infrared (IR) lines. Therefore, thorium is commonly used in spectroscopy for wavelength calibration.

The thorium lines of interest are isolated by using narrowband filters and tuning the etalons. These narrowband filters are discussed in Chapter 2. Thus, a single thorium HC lamp is used for determining the IP for both sodium and potassium images. For sodium, there are two thorium settings. The first thorium setting has the etalon A pressure fixed at the sodium pressure in order to conduct stability measurements. The second thorium setting has the etalon A and etalon B pressures reduced by 120 torr to get an IP at the sodium wavelength (ring radius). This is called a reduced ring thorium image (5891.451 Å). Figure 4.3 shows an image of the reduced ring thorium and Figure 4.4 shows its corresponding fitted spectrum.

The reduced thorium spectrum includes the thorium emission and several ghosts. The entire spectrum is fit in VoigtFit using 7 components and the Th I line is then isolated by removing unwanted components. The residuals of the fit contains the isolated Th I line and the continuum as seen in Figure 4.5. The centroid position of the Th I line in the main fitted spectrum (Figure 4.4) is rounded off to the nearest bin number and pairs of bin values at ± 10 , ± 15 , and ± 20 bins from the centroid position are compared to find the best starting and ending bin number that will determine the IP range. The bin value

pairs are usually the same (± 15) except for occasional cases where a different range is chosen. The best pair is selected when the intensities of the lower and upper bound on the bin range are closest to each other so that there are no abrupt changes between the IP and the continuum. Once a suitable pair of bins with similar intensities are chosen, five data points above and below that bin range are fixed to the intensity value of the bin number used to define the lower bound of the chosen bin pair. Figure 4.6 shows an IP with both ends fixed at one intensity value and is exported into VoigtFit to have its area normalized to one (Figure 4.7).

The IP is used empirically within VoigtFit when fitting all data. For potassium, there are no useful thorium lines within the potassium filter bandpass so a separate filter and thorium line 50 Å blueward (Th I line at 7647.380 Å) is used for the potassium IP construction. A very prominent argon I (7635.106 Å) line shows up in the thorium image and affects the tuning and IP construction. The thorium IP for potassium is constructed by restricting the range to exclude the strong argon I line. A full description of the IP construction for potassium is found in Nick Derr's senior thesis (2015).

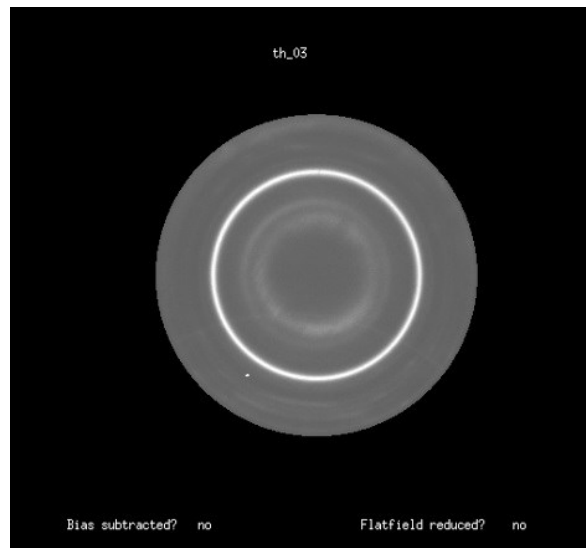


Figure 4.3: Fabry-Perot ring image for a reduced ring thorium calibration scan. Date: April 19, integration time: 30 seconds. (filename: th_03.fits).

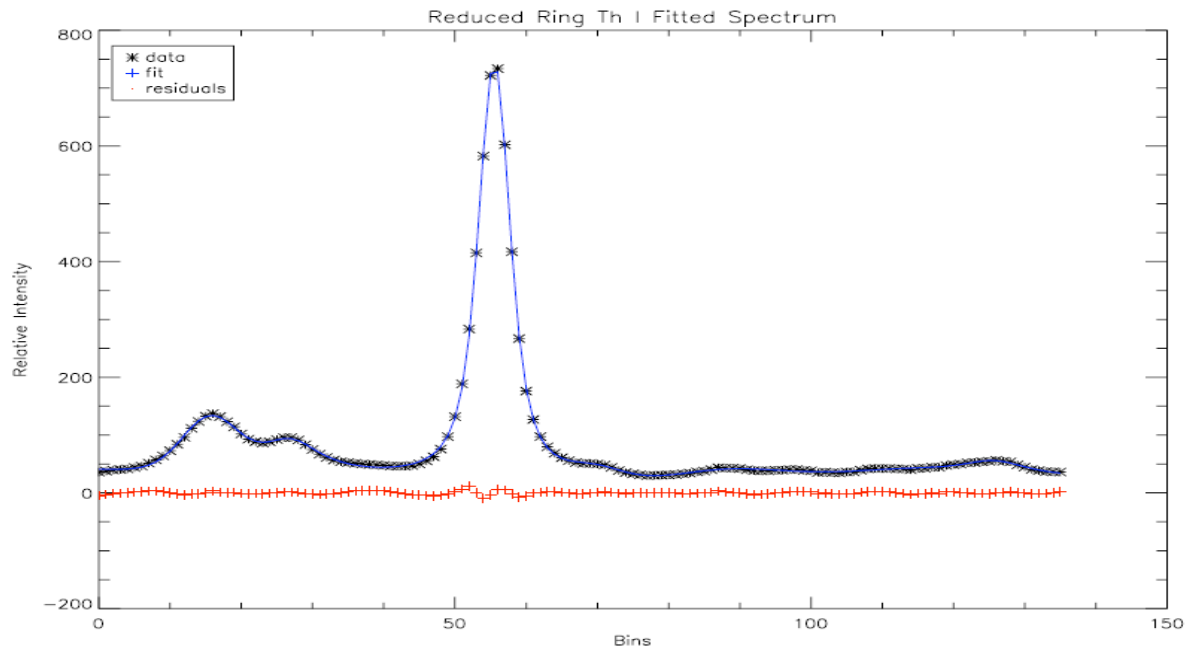


Figure 4.4: Fitted spectrum of a reduced ring thorium image for the ring image shown in Figure 4.3. The large peak is the bright Th I emission at 5891.451 \AA and the weaker emissions are ghosts from light of other orders getting in and also a weak argon I line.

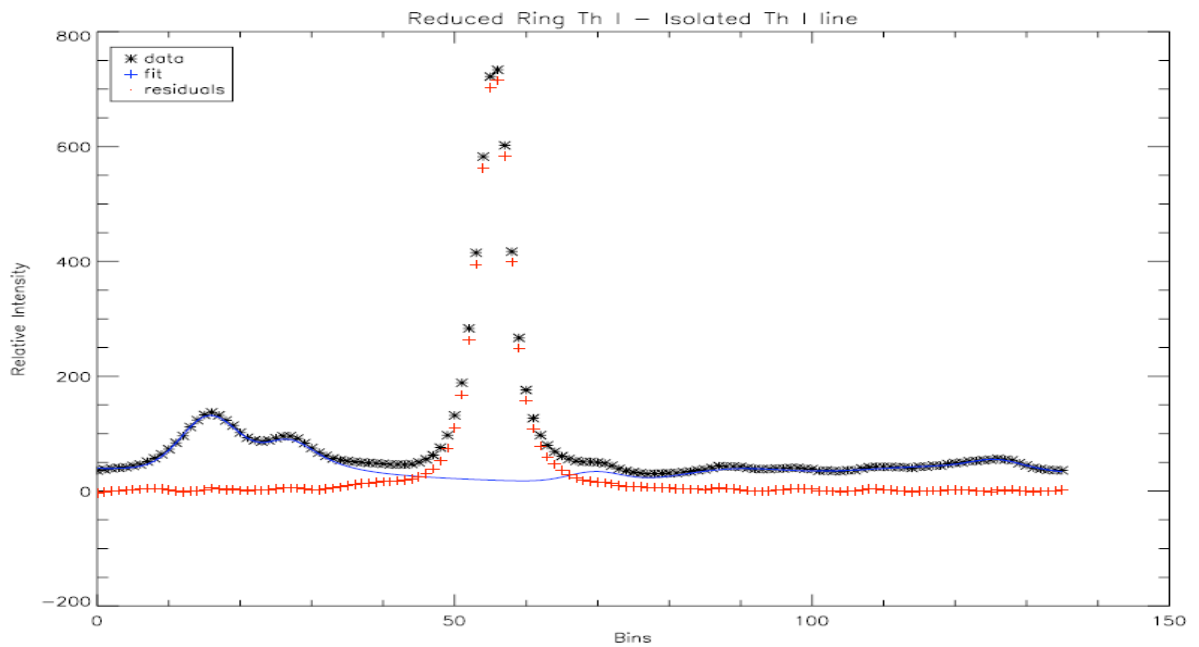


Figure 4.5: The reduced ring image with the corresponding fitted spectrum as shown in Figure 4.4 with the six ghosts removed. The residual of the fit here only contains the background and the isolated Th I.

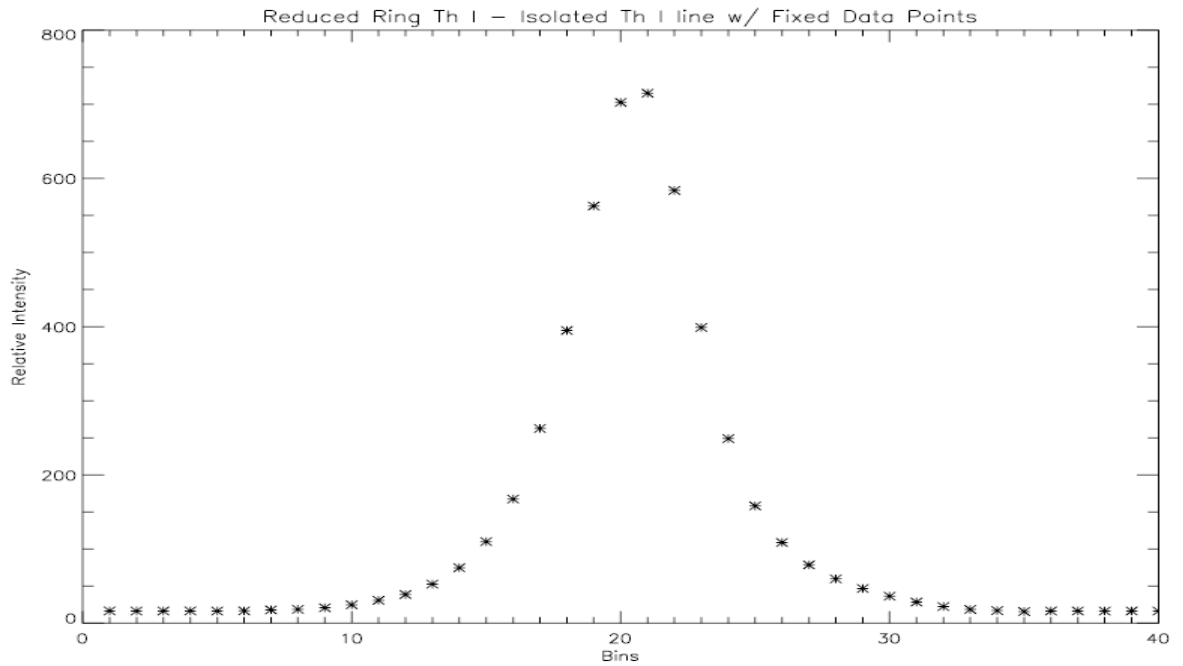


Figure 4.6: The isolated Th I line seen as a residual in Figure 4.5 with 5 data points on both ends fixed to a single value.

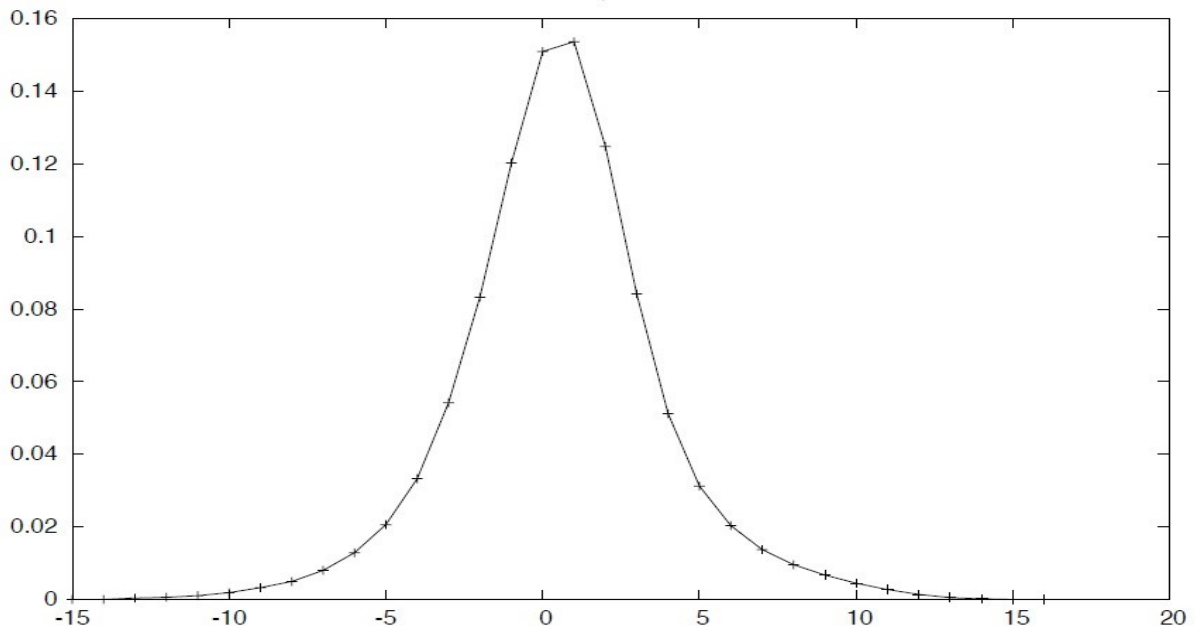


Figure 4.7: The IP created by using the file shown in Figure 4.6. The area is normalized to 1 in VoigtFit. Note that this is just a zoomed in plot of Figure 4.6 with a different x-axis.

4.2.2. Stability and Reliability of the IP

In order to assess the stability and reliability of the FPS, the variation in the IPs over the course of a run and months was analyzed. Observations of the Th I lines were taken nightly to monitor both wavelength and IP stability. The FP tune is sensitive to changes in temperature so monitoring the behavior of the IPs over the course of an observing run provides a good way of assessing the stability of the instrument and the reliability of the data. The instrument itself is anchored to a concrete pad on the north Port and is disconnected from the observatory floor. This means that the instrument experiences no external vibrations that could affect the IP. There are slight changes in ring center (prior to focus change and post focus change) but the ring center itself is very reproducible when the focus is kept constant. Every time the focus was changed, the calibration images were used to update the ring centers.

Figure 4.8 shows the Doppler and Lorentzian width of the IPs taken on each night for all the observing runs. The IPs stay consistent throughout all months with an average Doppler Width of 3.01 ± 0.20 bins with an RSD (Relative Standard Deviation) of 6.8 % and an average Lorentzian Width of 3.60 ± 0.15 with a RSD of 4.3%. The IPs have remained consistent and the FP is thus highly stable, as expected from not moving the instrument for over 3 years and the maximum temperature variation being between 14° C to 22° C. There is some minor variability in the stability of the instrument due to the two torr deadband in the pressure control system for each FP chamber.

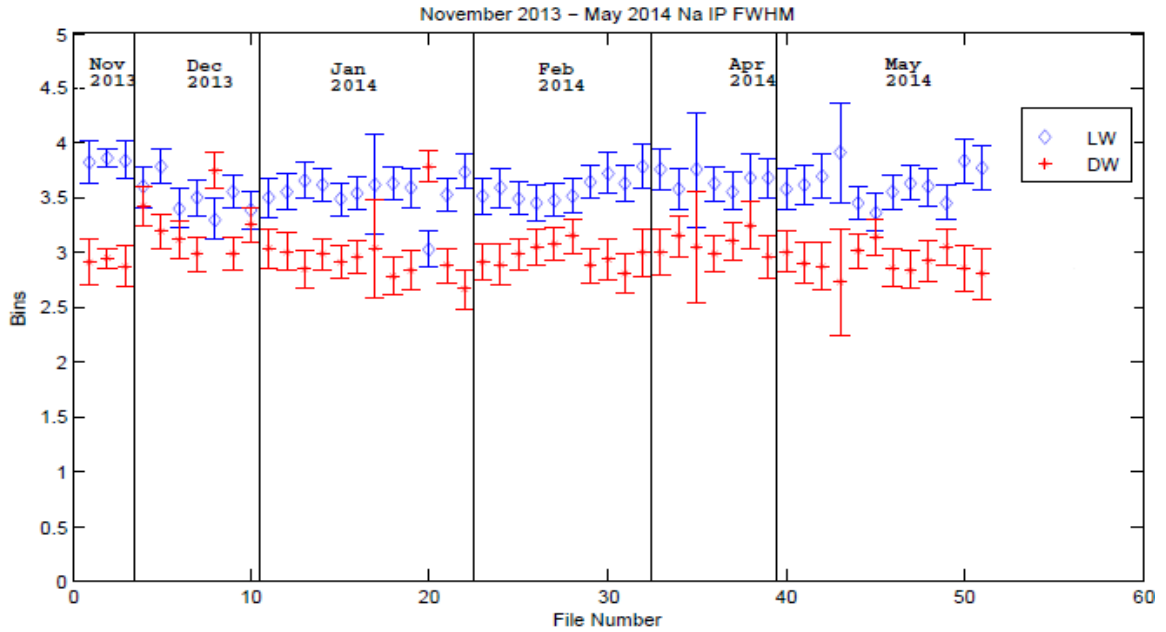


Figure 4.8: Plot showing the FWHM (Doppler (DW) and Lorentzian (LW)) for all the IPs from November 2013 – May 2014.

4.3. VoigtFit and Fitting Model

The ring summed spectra are fit using VoigtFit. VoigtFit is a nonlinear least squares fitting package developed by R. Carey Woodward. The sodium and potassium spectra are fit with a model composed of several Voigt profiles and a sloping background. A sample ring summed sodium spectrum is shown in Figure 4.9 and it is replotted in Figure 4.10 with a false zero point in order to show its absorption and emission features more clearly. Figure 4.11 shows the corresponding fitted spectrum of Figure 4.9. The Voigt profile is a line profile resulting from the convolution of a Lorentzian and Gaussian profile, both of which are naturally occurring line profiles in spectroscopy. The Voigt profile is characterized by four parameters. In VoigtFit these are the centroid position, area (intensity), the Gaussian width, and the Lorentzian width. VoigtFit can fit a spectrum with up to 12 Voigts, each consisting of the four parameters listed above.

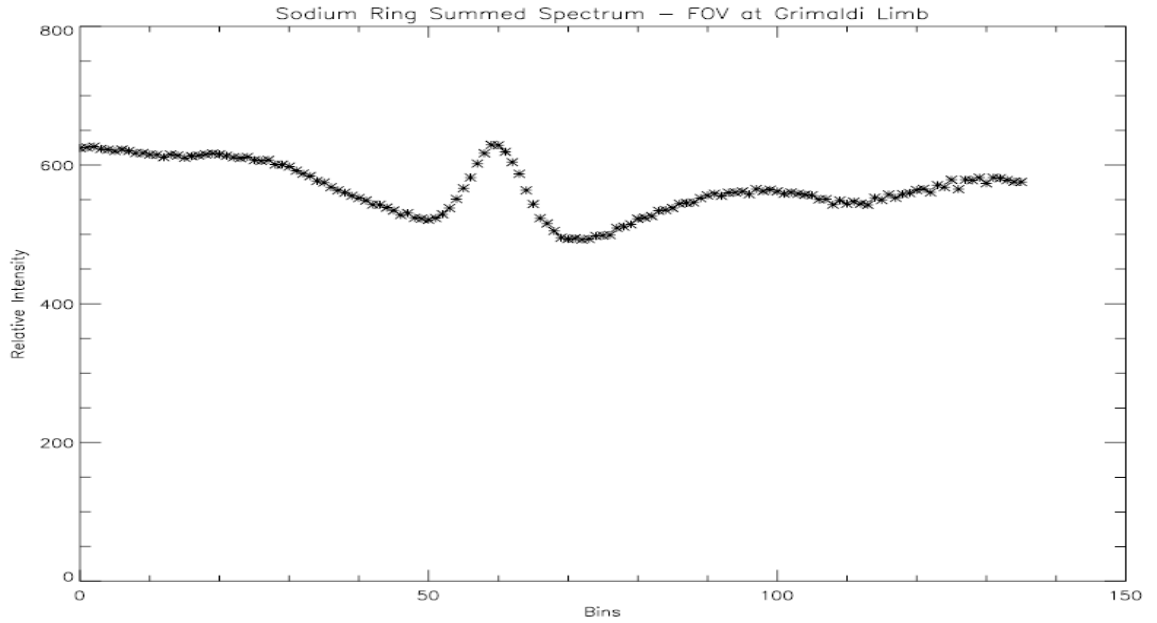


Figure 4.9: Ring-summed spectrum of a lunar sodium image taken on February 19 at the limb off the Grimaldi crater. Integration time: 300 s, time taken: 8:37 UT. (filename: moon_14.fits).

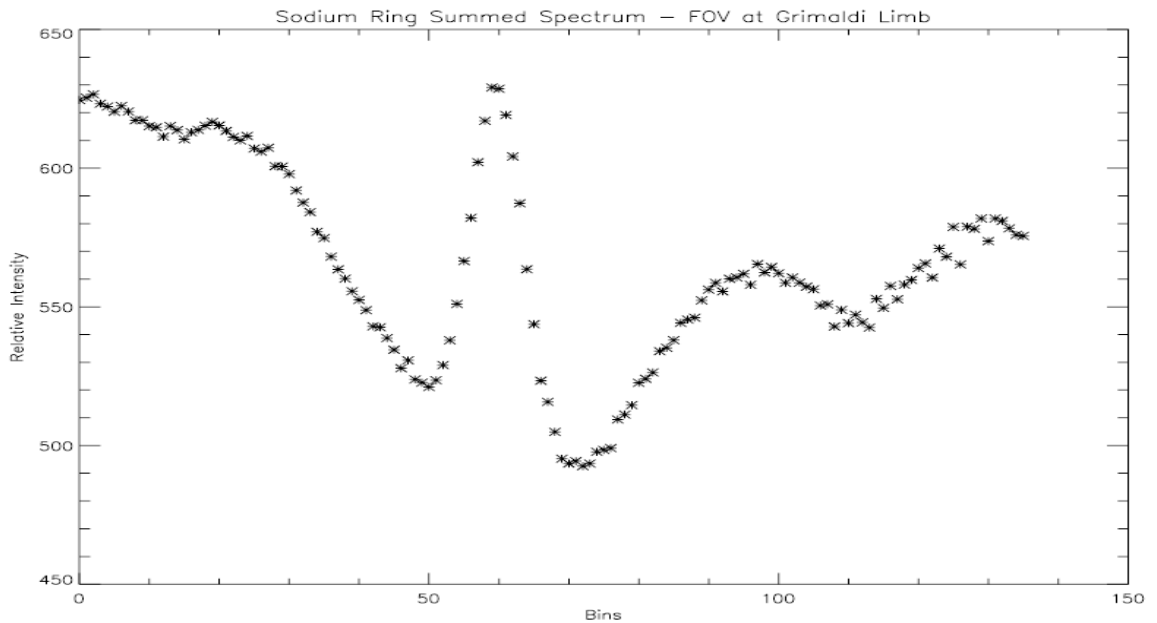


Figure 4.10: Lunar Sodium spectrum shown in Figure 4.9 plotted with a false zero. The emission and absorption features are seen more clearly here.

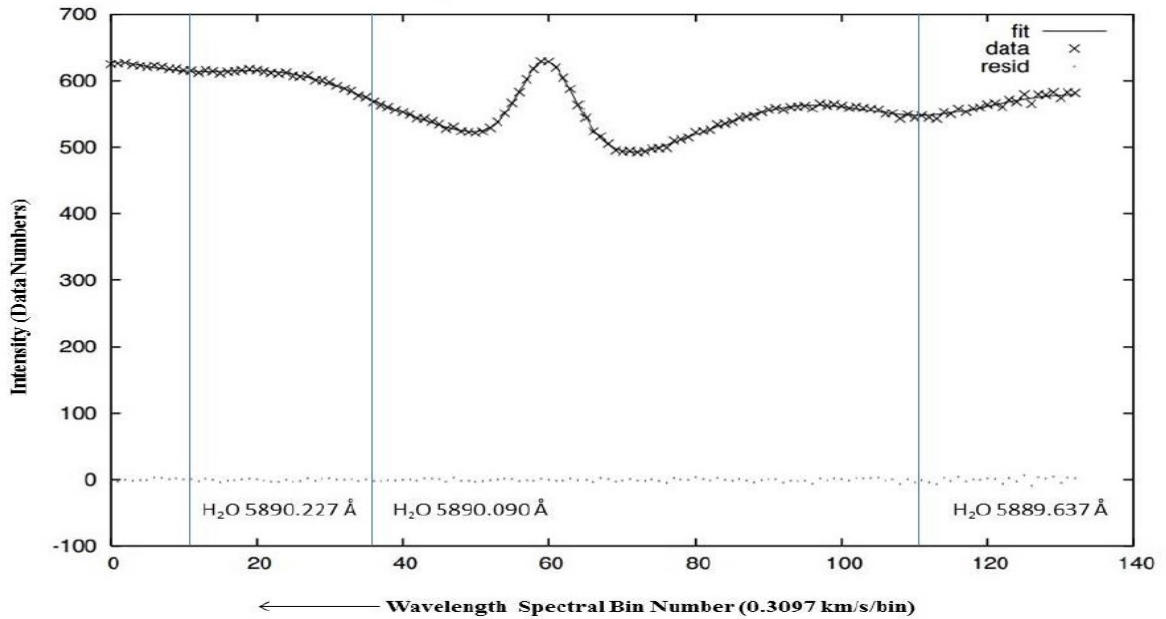


Figure 4.11: Lunar sodium spectrum shown in Figure 4.9, fir with VoigtFit, shown in Figure 4.9. The sodium spectrum consist of a solar Na Fraunhofer absorption feature (5889.9509 Å), 3 terrestrial water absorption features (marked by the blue lines), and the lunar hyperfine s-resolved sodium emission doublet (5889.9386 Å, 5889. 9584 Å) in a 3:5 intensity ratio.

4.3.1. Fitting Model for Lunar Sodium Spectra

Table 4.1 shows a sample fit file for the sodium spectrum shown in Figure 4.11, with all the Voigt parameters listed. Under the ‘status’ column, ‘free’ signifies a parameter that is free to move around while ‘fixed’ implies that the parameter is at a fixed value. Parameters with the word ‘link’ are linked to each other. For example, link (2) would mean that the parameter is linked to the same parameter of Voigt 2. As seen in Table 4.1, Voigt 3 and 4 are linked with each other (Voigt 4 is linked to Voigt 3 as signified by link (3) in centroid position, width, and area. Likewise, the widths of Voigt 5 and Voigt 6 are linked by width, and area to Voigt 2. Negative areas indicate an absorption feature while positive areas are emission features.

Table 4.1: Table summarizing the corresponding fit parameters for the spectrum in Figure 4.10.

Parameter	Value	Status	Uncertainty
Voigt 1			
Centroid	64.36	Free	0.1950
Doppler Width	39.54	Free	0.5344
Lorentzian Width	0	Fixed	0
Area	-5761	Free	86.21
Voigt 2			
Centroid	110.62	Free	0.3515
Doppler Width	20.89	Free	0.9348
Lorentzian Width	0	Fixed	0
Area	-977.8	Free	72.11
Voigt 3			
Centroid	58.61	Free	0.05809
Doppler Width	5.687	Free	0.2774
Lorentzian Width	0	Fixed	0
Area	907.9	Free	24.52
Voigt 4			
Centroid	61.86	Link (3)	0.05809
Doppler Width	5.688	Link (3)	0.2774
Lorentzian Width	0	Fixed	0
Area	544.7	Link (3)	14.71
Voigt 5			
Centroid	9.487	Free	0.5844
Doppler Width	21.99	Link (2)	1.200
Lorentzian Width	0	Fixed	0
Area	-734.8	Link (2)	76.68
Voigt 6			
Centroid	39.02	Free	0.6139
Doppler Width	21.9874499	Link (2)	1.20012994
Lorentzian Width	0	Fixed	0
Area	-734.878035	Link (2)	76.6805252
Continuum			
Offset	650.282563	Free	2.31457889
Slope	-0.492958444	Free	0.0116651948

The model for fitting sodium spectra contains six lines and a continuum. A bias of 300 is subtracted from all raw images before fitting the spectra. The six components are: The sodium D2 S-resolved hyperfine structure is fit with two emissions components at 5889.936 Å and 5889.9584 Å that are linked in a 3:5 ratio (McNutt and Mack, 1963), a single component to fit the solar Fraunhofer absorption line at 5890.9509 Å, and three components to fit the terrestrial water absorption lines (McNutt and Mack, 1963) at 5890.227 Å, 5890.090 Å, and 5889.637 Å (Figure 4.10).

The observed depth of the solar Fraunhofer D line is significantly filled in, approximately 70% of the continuum value, compared to the measured depth of 5% of the spectral continuum. Parasitic light is the primary contamination. Parasitic light is unwanted continuum light getting into the instrument due to scattered light from the Moon and from light transmitted through unwanted orders. Another contribution, much smaller than the effects of parasitic light, is the filling of the Fraunhofer line due to Brillouin scattering (Potter et al., 1984) which is on the order of a couple of percent. The terrestrial sodium emission, as seen in Figure 4.12, is a minor contamination source to the total lunar emission for observation taken at 1 lunar radius or more. Sodium nightsky observations (taken 5 to 10 degrees from Moon center) indicate that terrestrial sodium emission is an insignificant contribution to the observed lunar emission for all observations less than one lunar radii away from the Moon's limb.

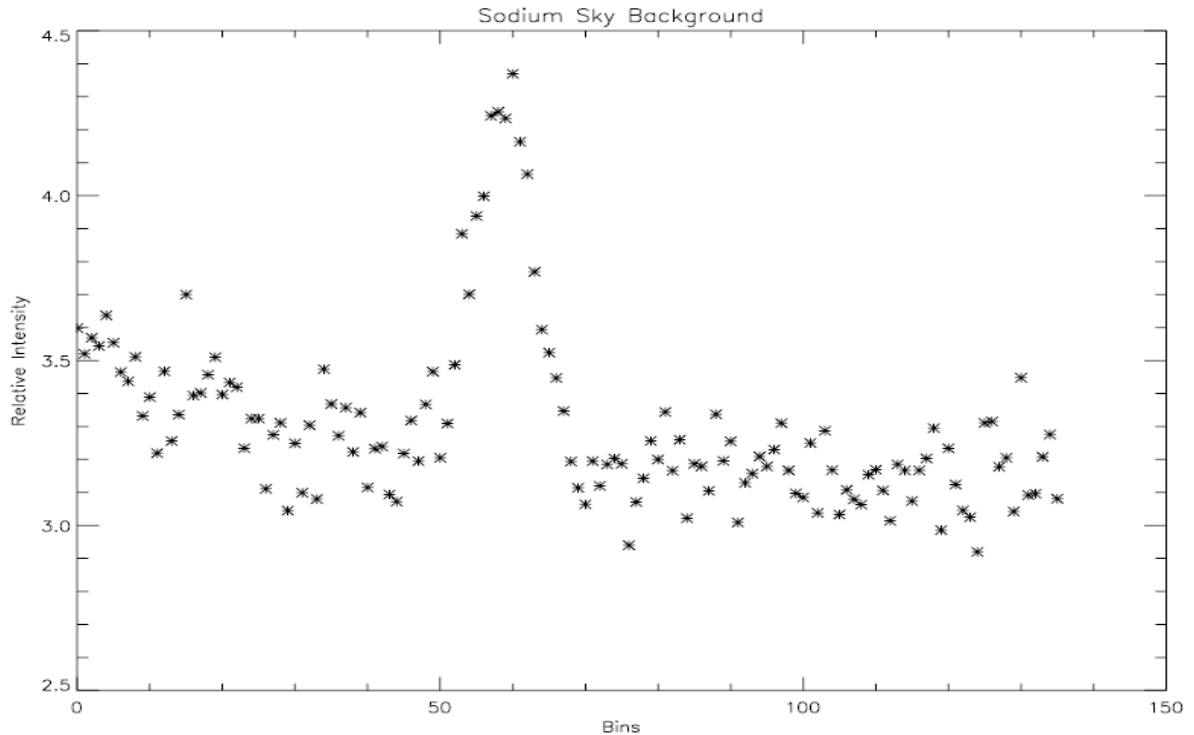


Figure 4.12: Sky background image taken 40 minutes west from the moon center. Integration time: 300 seconds, data taken: May 16, time taken: 07:41 UT.

4.4. Wavelength Calibration

The sodium wavelength calibration is determined by using the sodium “Gates” lamp. Due to the high densities and large oscillator strength of resonance transitions of the Sodium D lines, the sodium lamp produces D2 emissions with self-absorption. The self-absorption feature occurs due to sodium atoms in the center of the lamp being hotter than those around the edge. The photons emitted by the atoms in the center are absorbed by the surrounding atoms and are re-emitted in all directions. This means that the photons emitted by the atoms in the center are likely to never reach the edge of the tube and get out of the lamp. A sodium ring image and an example of what the self-absorption feature looks like is shown in Figures 4.13 and 4.14, respectively. The position of the sodium self-reversal feature combined with the Earth-Moon Doppler correction (obtained

from the JPL Horizons ephemeris program website) allows the determination of the sodium velocity in the lunar frame of reference.

The Thorium hollow cathode images determine the correct ring center for the Fabry-Perot interference pattern. Since the ring center changes when the CCD camera focus is changed, the thorium (Na) and sodium “Gates” lamp calibration images are used to define the ring center and each time the focus is changed, a new set of calibration images are taken. The same thing is done for potassium images except the thorium (K) hollow cathode lamp and a potassium hollow cathode lamp are used.

The thorium (Th I (Na)) calibration is done using a thorium hollow-cathode lamp measured at 5891.451 \AA and is used for determining ring centers and monitoring wavelength shifts. For potassium, the Th I (Th (K)) line at 7647.380 \AA is used to create the IP as shown in Derr (2015). For potassium lunar images, calibrations are done using a potassium lamp measured at 7698.9647 \AA . The potassium lamp is used for tuning the instrument to the potassium wavelength. The potassium calibrations are performed less frequently than sodium calibrations because potassium observations are fewer and typically taken over a smaller time interval due to a smaller scale height and the absence of a potassium tail. Since the sodium images span a large time interval, the Th (Na) measurements are made more frequently as to monitor any temperature shifts. Due to the stability of the FP, it is in theory possible to take the pressures from the previous night as a new set of values. In practice, however, calibration images taken with sodium and thorium lamps are done every night in order to verify the stability of the instrument. Most changes in pressure occur due to temperature variations and the reproducibility of the pressure system. Furthermore, ring centers must be redetermined once the CCD camera is refocused. My results obtained through the data analysis techniques discussed here are presented in the following chapter.

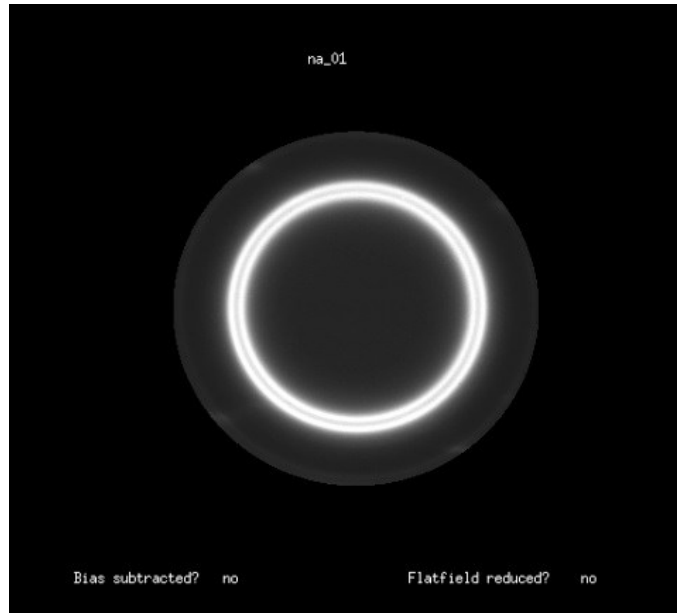


Figure 4.13: Fabry-Perot ring image of a sodium lamp calibration image. Integration time: 10 seconds, date: February 19, time taken: 4:03. (filename: na_01.fits).

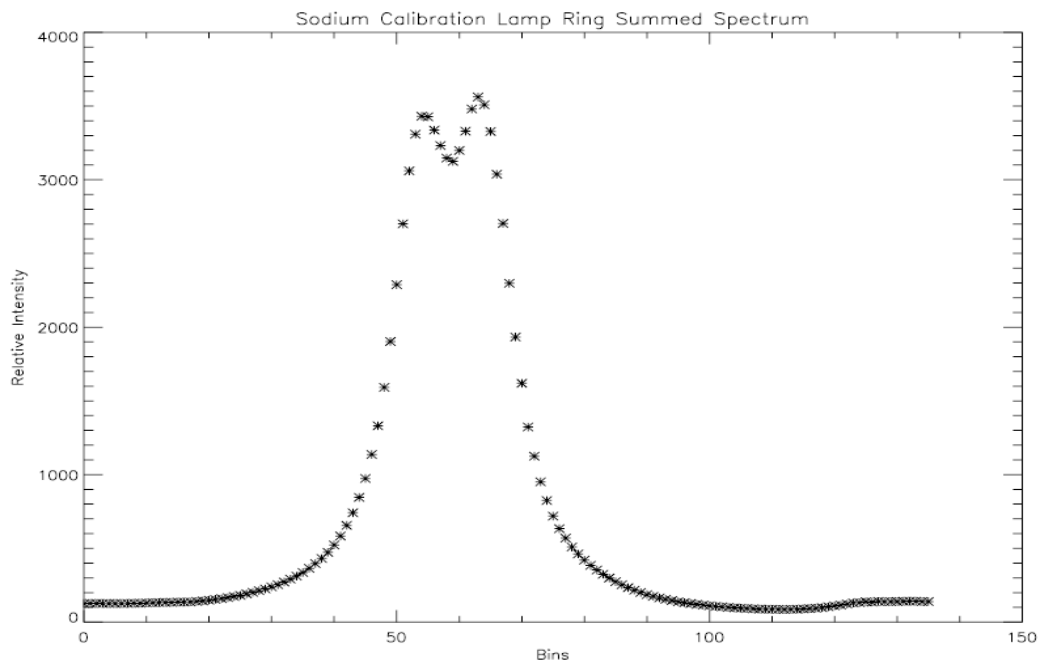


Figure 4.14: Ring-summed spectrum of the sodium lamp image seen in Figure 4.13.

CHAPTER 5

5. RESULTS

In the subsequent sections in this chapter, I present sodium line widths as a function of phase angle by month, distance from the limb, and sodium relative intensity as a function of distance off the limb. In Chapter 6 I will discuss the trends seen in this chapter with respect to previous work, recent lunar missions, and current knowledge about the possible source and sink mechanisms of the lunar exosphere. Chapter 6 also compares the potassium data to the sodium data.

The measured Doppler line widths along with observations parameters such as phase angle, temperature, and distance for each of the months are shown in Appendix A. The measured Doppler line width is related to effective temperature through the following relation,

$$\Delta\lambda_{FWHM} = 2\lambda_0 \sqrt{\frac{2kT \ln(2)}{mc^2}} \quad \text{Eq. 5.1}$$

where the $\Delta\lambda_{FWHM}$ is proportional to the square root of the temperature T of the emitting population (Mierkiewicz et al., 2012), from which the following equation can be obtained by using the mass of a sodium atom,

$$T_{eff} = 4.51 \times 10^{13} \left(\frac{\Delta\lambda_{FWHM}}{\lambda_0} \right)^2 \text{ [K]} \quad \text{Eq. 5.2}$$

where T_{eff} is the effective temperature, m is the mass of the atom in kg, k is Boltzmann's constant, c is the speed of light, $\Delta\lambda_{FWHM}$ is the Doppler broadened wavelength, and λ_0 is the rest wavelength of the sodium emission.

For non-relativistic limits, where $v \ll c$, the wavelength shift is,

$$\frac{\Delta\lambda}{\lambda} = \frac{v}{c} \quad \text{Eq. 5.3}$$

where v is the Doppler width in km s^{-1} and c is the speed of light in vacuum. The measured Doppler widths are converted into units of km s^{-1} by multiplying the measured line width by the dispersion value of $0.3097 \text{ km s}^{-1} \text{ bin}^{-1}$. Using Equation 5.3, Equation 5.2 can be written as follows,

$$T_{eff} = C(m) \times v^2 \quad \text{Eq. 5.4}$$

where $C(m) = 501$ for sodium and $C(m) = 850$ for potassium.

5.1. Line Width (FWHM) vs Phase Angle Dependence by Month

The line width results I show here are limited to observations taken within 28 seconds in RA (east and west) and 7 arcmin in dec (north and south) from the lunar limb. Equatorial regions refer to offset craters on the selenographic east limb (Langrenus and Cleomedes) and on the selenographic west limb (Grimaldi and Aristarchus). High latitude regions use Tycho as an offset crater on the south limb and Plato as an offset crater on the north limb. In all the plots that follow, data points are color coded by offset crater. Open symbols indicate before full Moon and closed symbols indicate after full Moon. The horizontal axis represents lunar phase angle where 0° correspond to full Moon, and 90° corresponds to 1st and 3rd quarter. Line widths will be discussed by month; global trends will be further discussed in Section 6.1.

The November 2013 data in Figures 5.1 and 5.2 for the equatorial and high latitude limbs indicate a decrease in line width following full Moon. There were no observations made off the limb near Cleomedes crater in November. Line widths are largest at low phase angles (close to full Moon) and smallest at high phase angles (post full Moon).

Line widths for both equatorial and high latitude limbs in December 2013, shown in Figures 5.3 and 5.4, increase during waxing phase and decrease post full Moon. Sodium derived effective temperatures are highest during magnetotail passage (phase angle $< \sim 40^\circ$ or full Moon ± 3 days).

January 2014 equatorial regions, shown in Figure 5.5, are similar to December 2013, but with a more exponential-like fall off in line width post full Moon. Line widths, and implied temperatures, are highest during magnetotail passage and lowest at large phase angles. The fall off in line width seen in the equatorial regions (Figure 5.5) is less apparent in the high latitude regions (Figure 5.6), but it can be seen that line widths increase going towards full Moon and decrease post full Moon.

For February 2014, the equatorial region (Figure 5.7) line widths are smaller at phase angles less than 10° (full Moon period) as compared to line widths at phase angles between $10 - 20^\circ$. This trend is contrary to other months where the line widths during full Moon were largest. Apart from data taken during full Moon, the falloff in line width is noticeable starting at phase angle $\sim 20^\circ$, where the Moon is still going through magnetotail passage. Post magnetotail passage temperatures fall off in a similar fashion to other months and exhibit a familiar exponential-like trend seen in the January 2014 equatorial data. The high latitude region shows a similar narrow line width at full Moon, different to what is seen for high latitude regions in other months. The fall off after magnetotail passage is, however, not as apparent as in the equatorial regions.

The falloff in line width is observed for both equatorial and high latitude limbs around phase angle 25° for April 2014 data (Figures 5.9 and 5.10), although data is limited. Note, line widths are quite narrow towards high phase angles.

For the May 2014 equatorial regions (Figure 5.11), line widths increase entering the magnetotail and fall during egress, with the largest values near full Moon. The same pattern is observed for all months except February. There is less scatter in the data in May compared to previous months and the exponential fall off in line width is more apparent. Note that the April 2014 and May 2014 data have less scatter and exhibit very narrow widths with smaller error bars than other months.

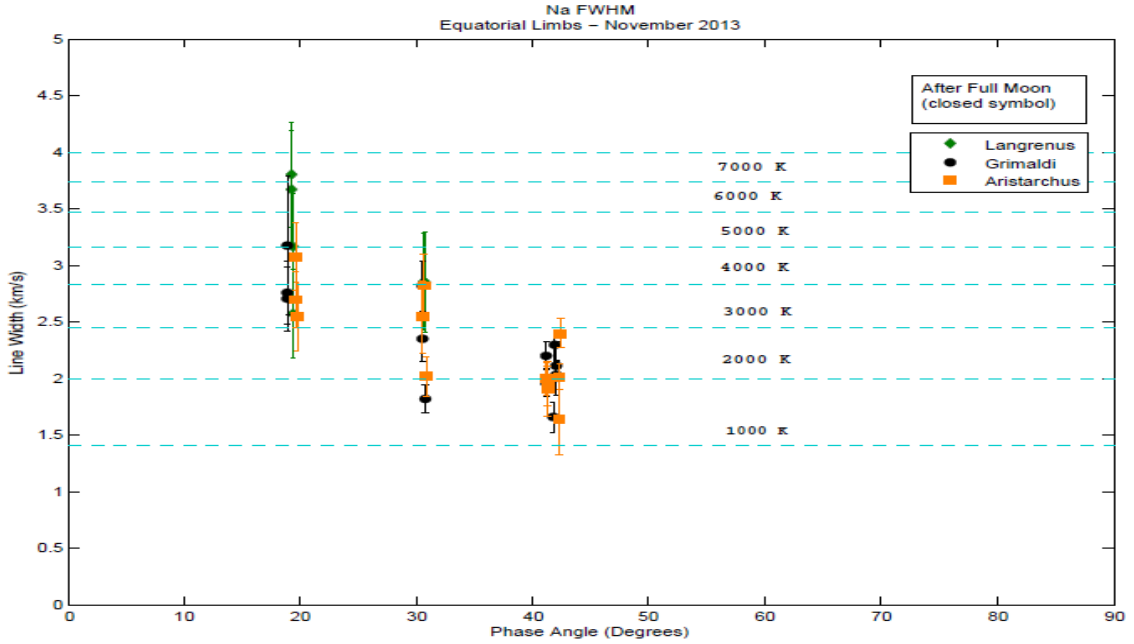


Figure 5.1: Equatorial Doppler width (FWHM) as a function of lunar phase angle for November-2013. Observations presented here were made at 1.5 arcmin, 3.5 arcmin, and 28 seconds of time from the east and west limbs. There are no pre full Moon data for the November 2013 run.

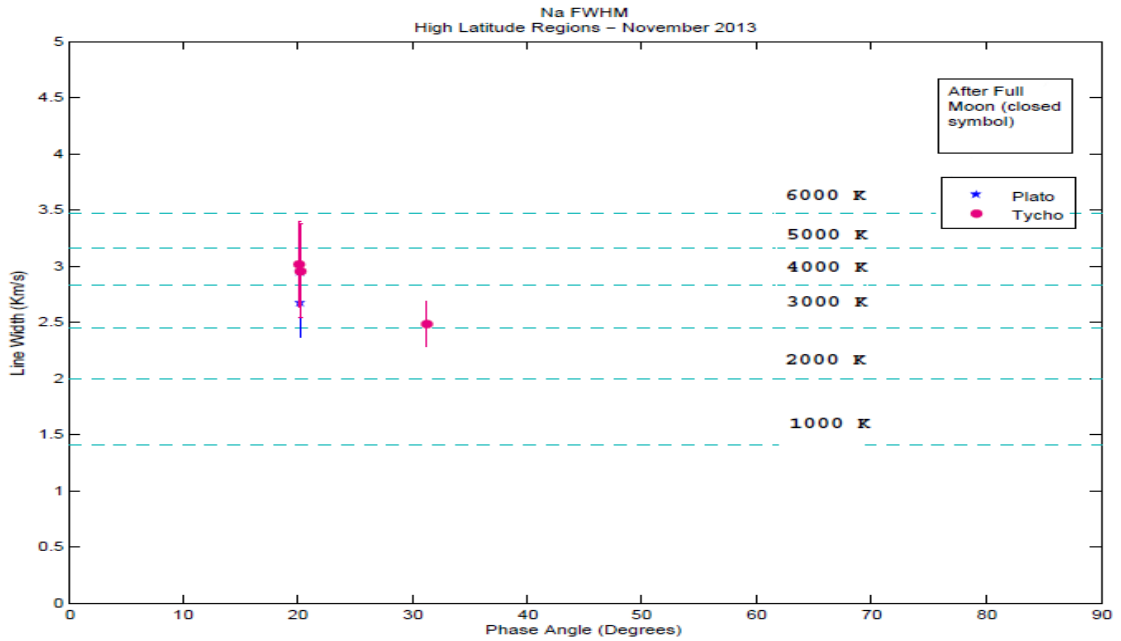


Figure 5.2: High Latitude Doppler width (FWHM) as a function of lunar phase angle for November-2013. Observations presented here were made at 1.5 arcmin, 3.5 arcmin, and 7 arcmin from the north and south limbs.

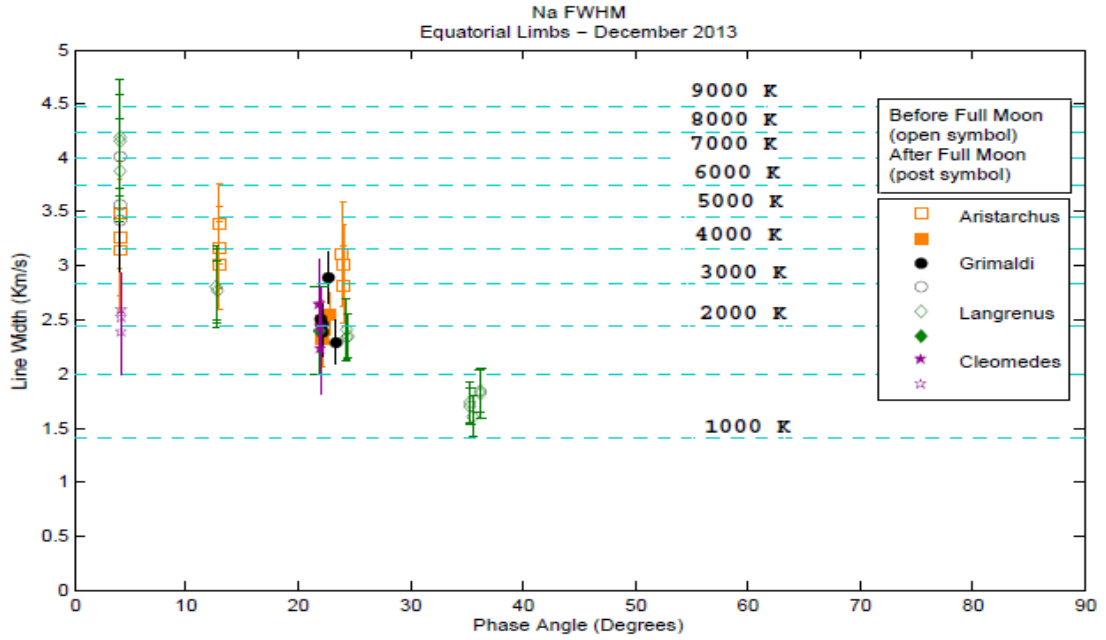


Figure 5.3: Equatorial Doppler width (FWHM) as a function of lunar phase angle for December-2013. Observations presented here were taken at 1.5 arcmin, 3.5 arcmin, and 28 seconds of time from the east and west limbs. Nearest observation to full Moon is at phase angle $\sim 4^\circ$.

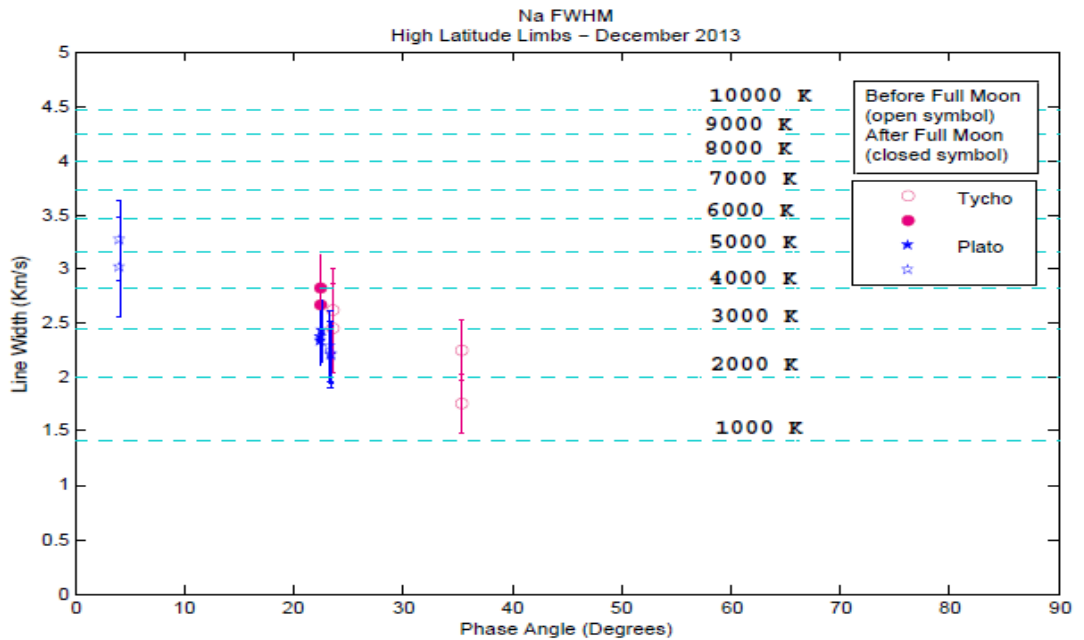


Figure 5.4: High Latitude Doppler width (FWHM) as a function of lunar phase angle for December-2013. Observations presented here were made at 1.5 arcmin, 3.5 arcmin, and 7 arcmin from the north and south limbs.

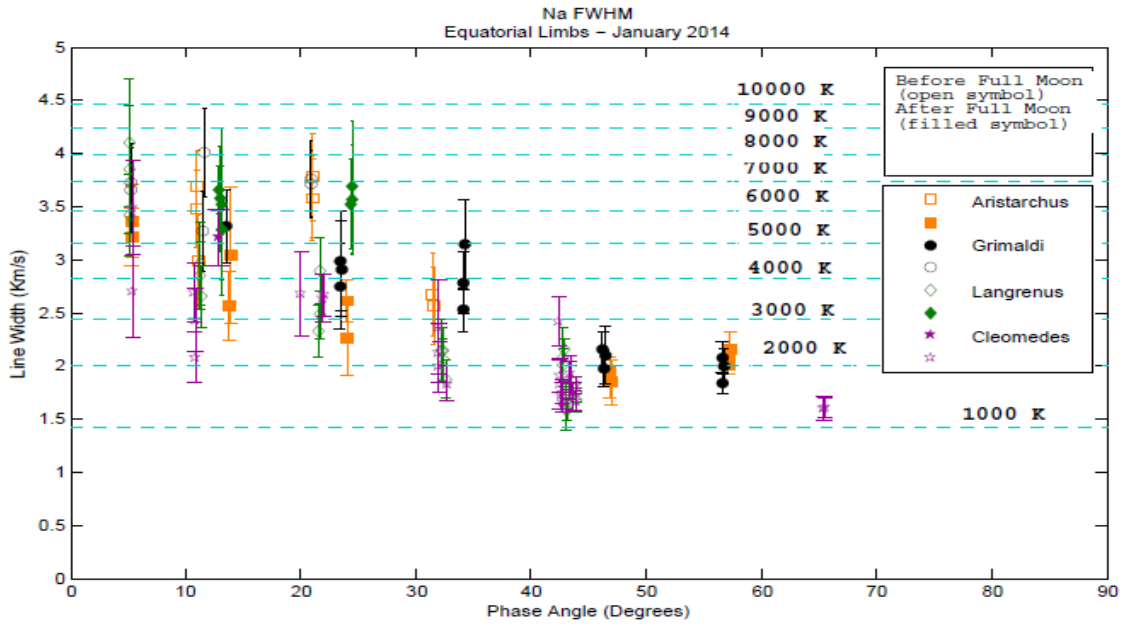


Figure 5.5: Equatorial Doppler width (FWHM) as a function of lunar phase angle for January-2014. Observations presented here were taken at 1.5 arcmin, 3.5 arcmin, and 28 seconds of time from the east and west limbs. Nearest observation to full Moon is at phase angle $\sim 5^\circ$.

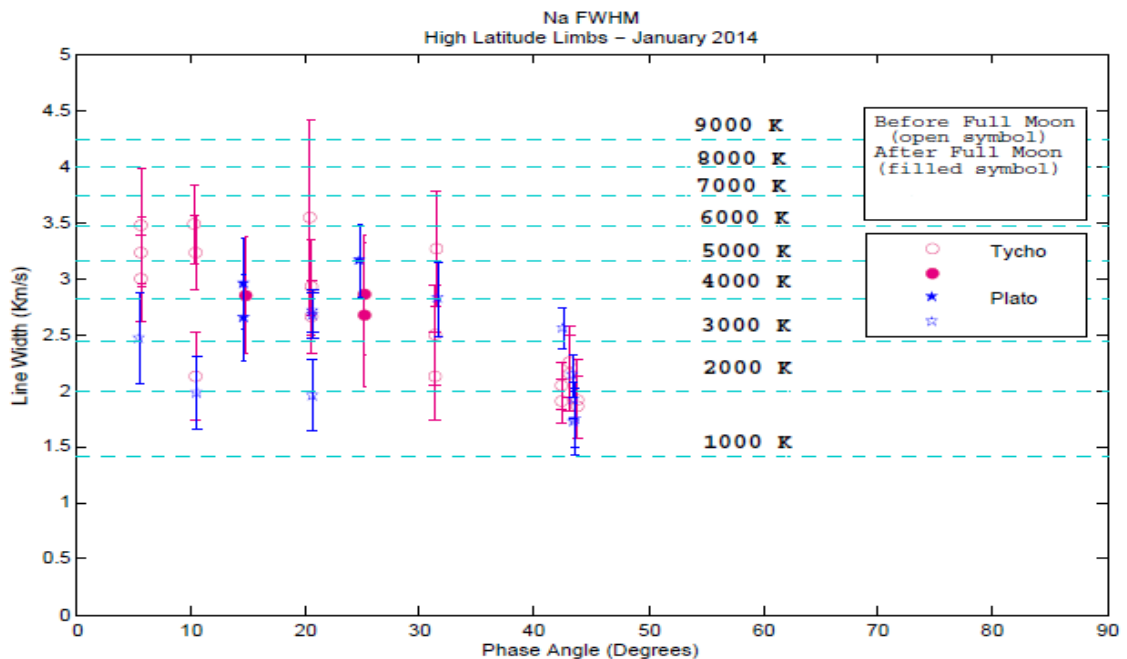


Figure 5.6: High Latitude Doppler width (FWHM) as a function of lunar phase angle for January-2014. Observations presented here were made at 1.5 arcmin, 3.5 arcmin, and 7 arcmin from the north and south limbs.

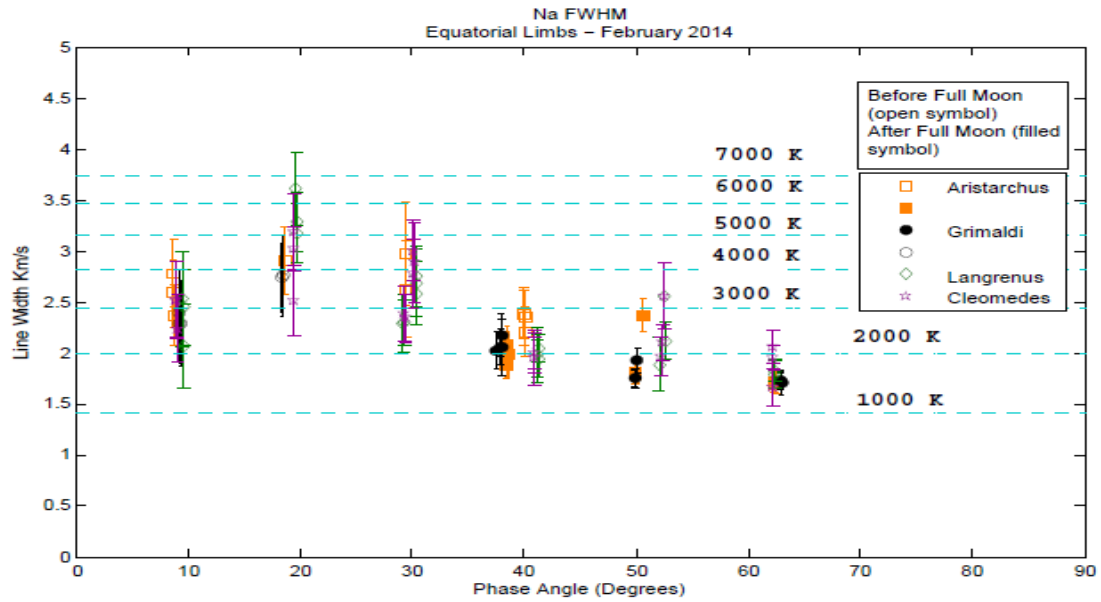


Figure 5.7: Equatorial Doppler width (FWHM) as a function of lunar phase angle for February-2014. Observations presented here were taken at 1.5 arcmin, 3.5 arcmin, and 28 seconds of time from the east and west limbs. Nearest observation to full Moon is at phase angle $\sim 9^\circ$.

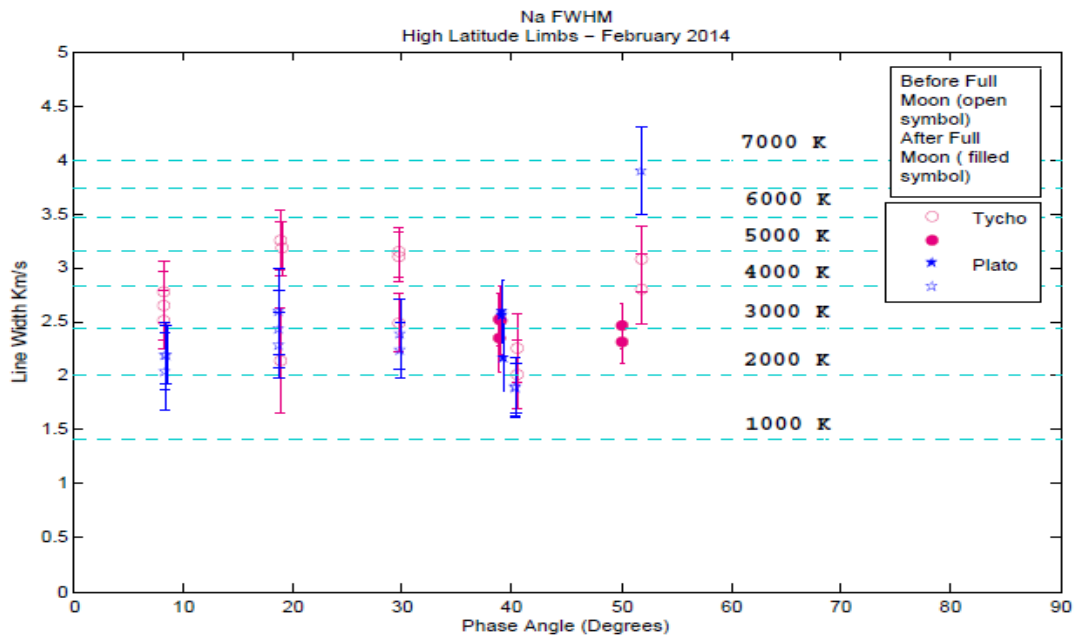


Figure 5.8: High Latitude Doppler width (FWHM) as a function of lunar phase angle for February-2014. Observations presented here were made at 1.5 arcmin, 3.5 arcmin, and 7 arcmin from the north and south limbs.

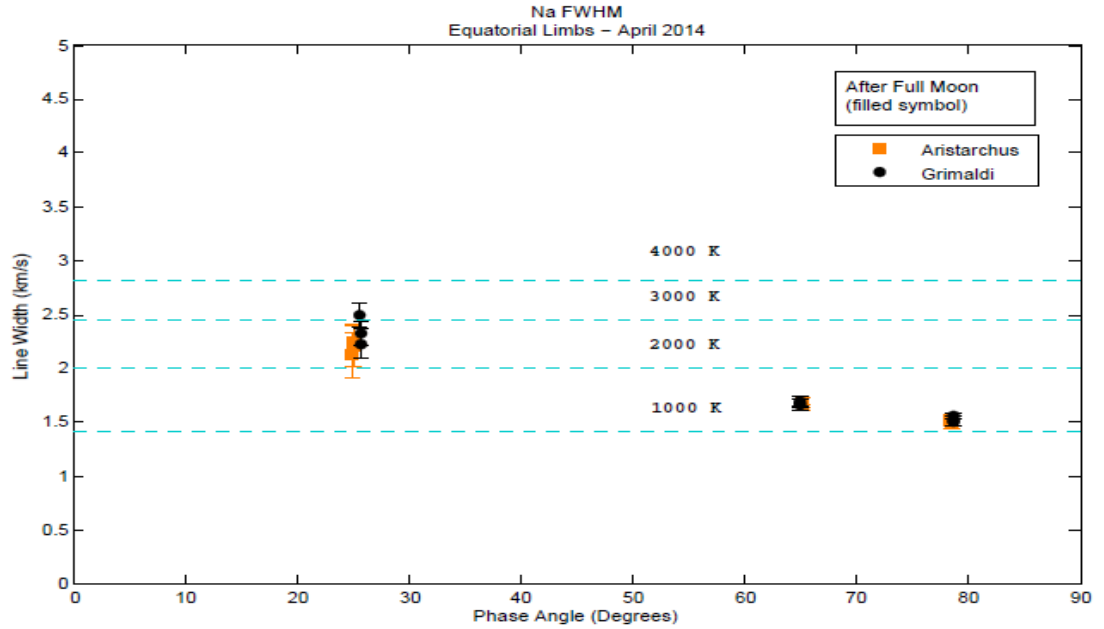


Figure 5.9: Equatorial Doppler width (FWHM) as a function of lunar phase angle for April-2014. Observations presented here were taken at 1.5 arcmin, 3.5 arcmin, and 28 seconds of time from the east and west limbs. Nearest observation to full Moon is at phase angle $\sim 2^\circ$.

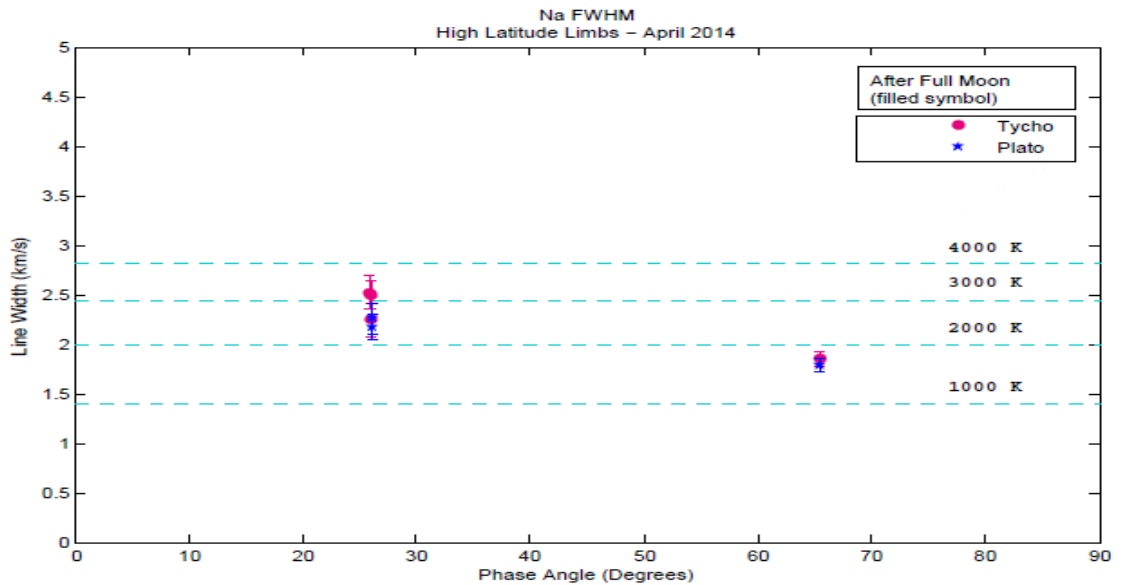


Figure 5.10: High Latitude Doppler width (FWHM) as a function of lunar phase angle for April-2014. Observations presented here were made at 1.5 arcmin, 3.5 arcmin, and 7 arcmin from the north and south limbs.

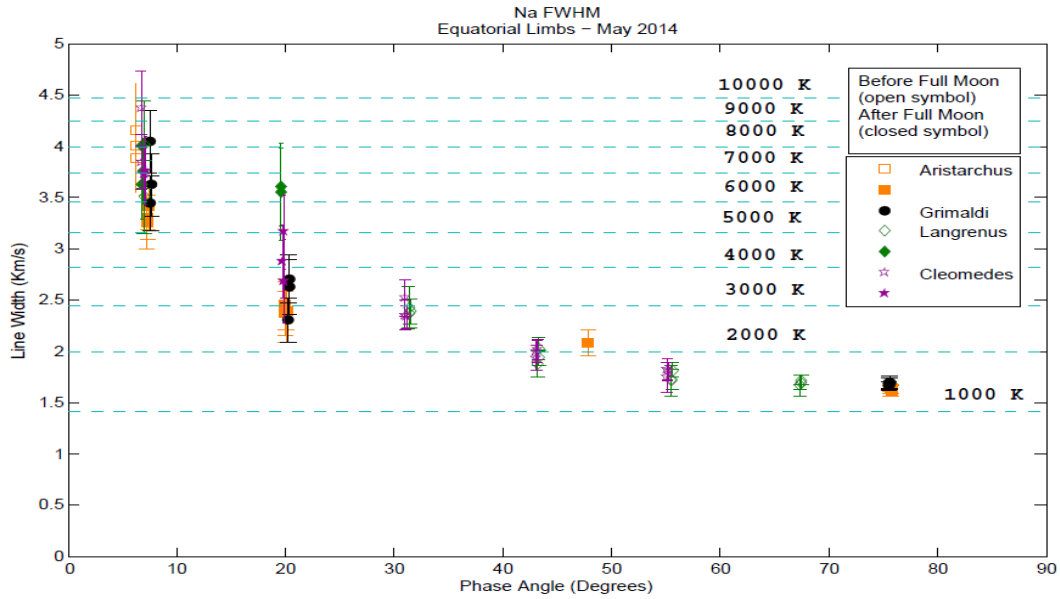


Figure 5.11: Equatorial Doppler width (FWHM) as a function of lunar phase angle for May-2014. Observations presented here were taken at 1.5 arcmin, 3.5 arcmin, and 28 seconds of time from the east and west limbs. Nearest observation to full Moon is at phase angle $\sim 6^\circ$.

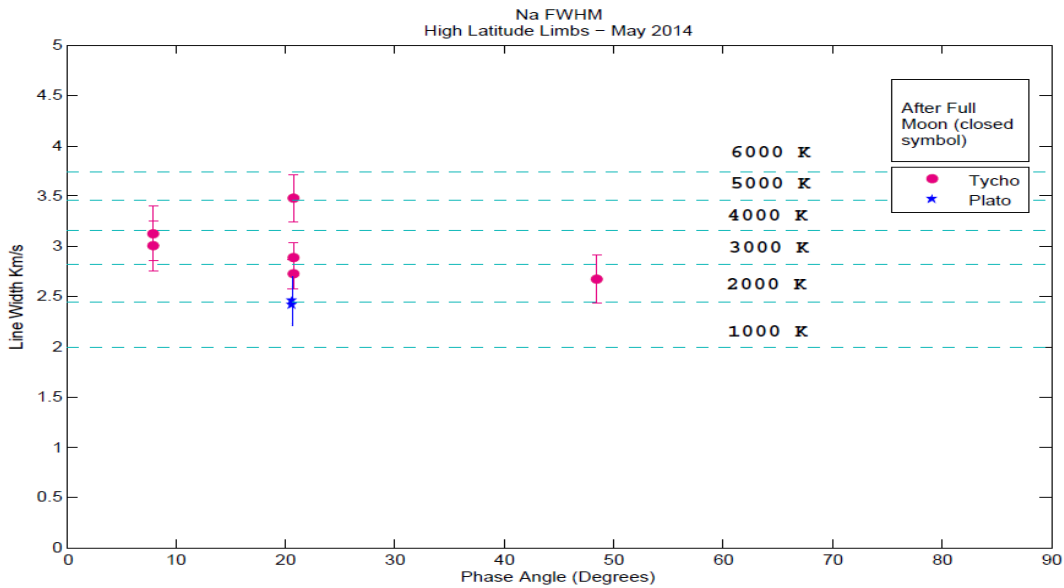


Figure 5.12: High Latitude Doppler width (FWHM) as a function of lunar phase angle for May-2014. Observations presented here were made at 1.5 arcmin, 3.5 arcmin, and 7 arcmin from the north and south limbs.

5.2. Line Width as a Function of Distance from the Limb

Figure 5.13 shows line width trends as a function of distance from the Moon for the high latitude and equatorial limbs (January 14, 2014). The line widths off Tycho (selenographic south limb) and Plato (selenographic north limb) are comparable for pointings less than 5 arcmin off the limb. For observations farther than 5 arcmin, Tycho offsets have larger line widths than Plato offsets. The line widths on the selenographic west limb (Aristarchus limb) are larger than those on the selenographic east limb (Langrenus limb).

Figure 5.14 shows the line width as a function of distance for the equatorial limbs on the selenographic east (Langrenus) and selenographic west (Grimaldi) limb of the Moon for May 10, 2014 and May 18, 2014, respectively. The Langrenus line widths are flat overall, while the line widths for Grimaldi offsets fall off slightly towards larger distances off the limb. The line widths, and thus temperatures, for the selenographic west limb (Grimaldi) are larger than their selenographic east (Langrenus) limb counterparts.

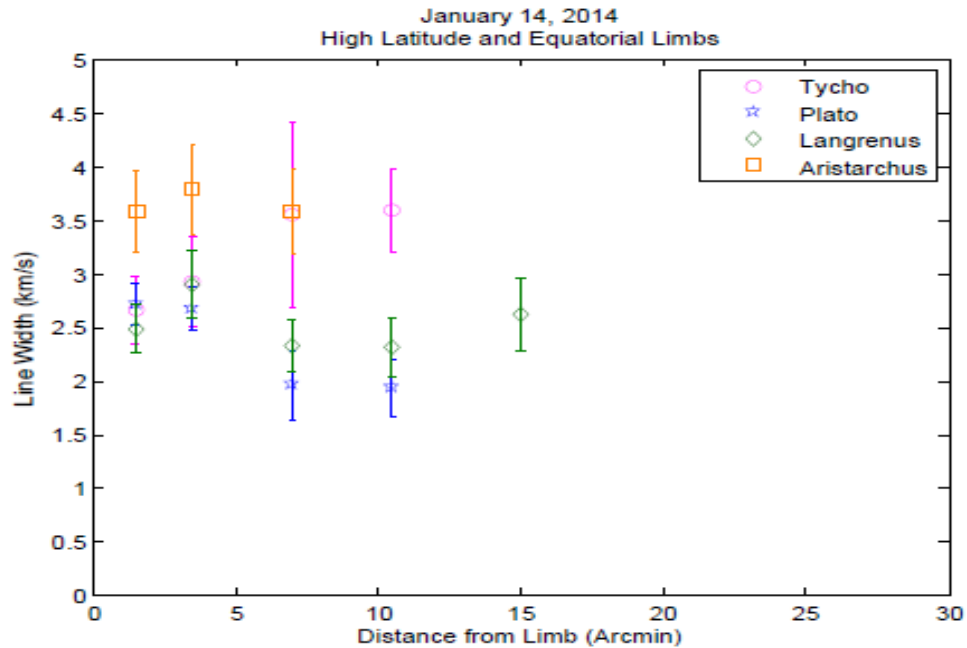


Figure 5.13: FWHM as a function of distance off the selenographic north (Plato limb), south limb (Tycho limb), west limb (Aristarchus limb), and east limb (Langrenus limb) on January 14, 2014.

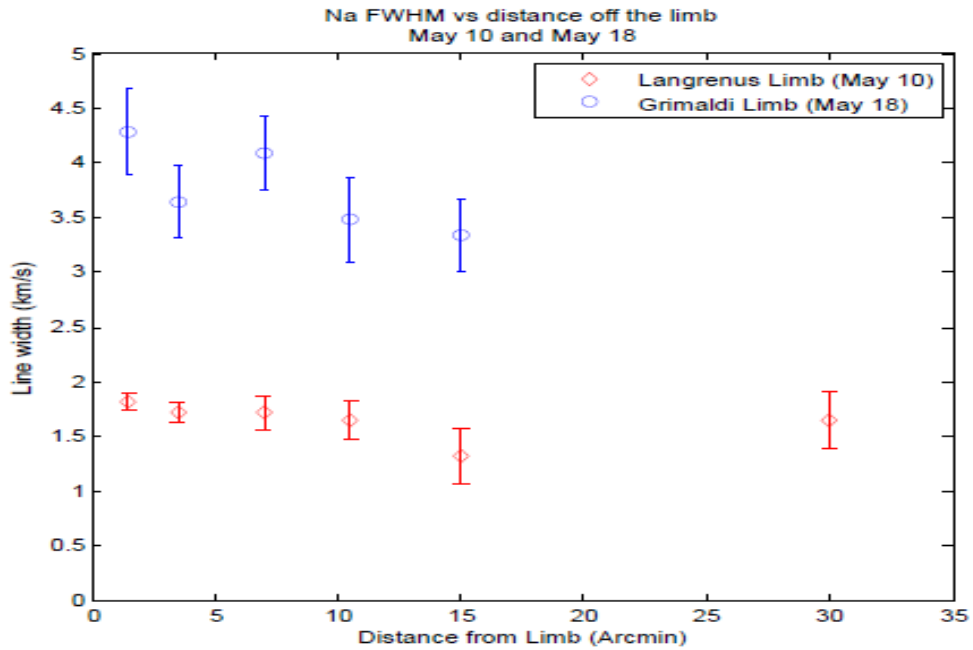


Figure 5.14: FWHM as a function of distance off the selenographic east limb (Langrenus limb) of the moon on May 10, 2014 and off the Selenographic west limb (Grimaldi limb) on May 18, 2014. May 10 and May 18 are approximately at the same phase angle pre and post full Moon.

5.3. Relative Intensity as a Function of Distance off the Limb

The relative intensity of the line and scattered light contributions decreases as a function of distance from the Moon as seen in Figures 5.15, 5.16, and 5.17. Data in Figures 5.15 and 5.16 are off craters on the selenographic east limb of the Moon while Figure 5.17 shows the selenographic west limb of the Moon. The relative intensity off the Langrenus limb, Figure 5.15, shows weaker sodium emission as compared to the Cleomedes limb shown in Figure 5.16. The relative intensities off the Grimaldi limb, Figure 5.17, have a much higher continuum at the same distances off the Langrenus and Cleomedes limbs. Due to the high continuum off the Grimaldi limb, it is difficult to see a clear sodium emission without first fitting and accounting for the background.

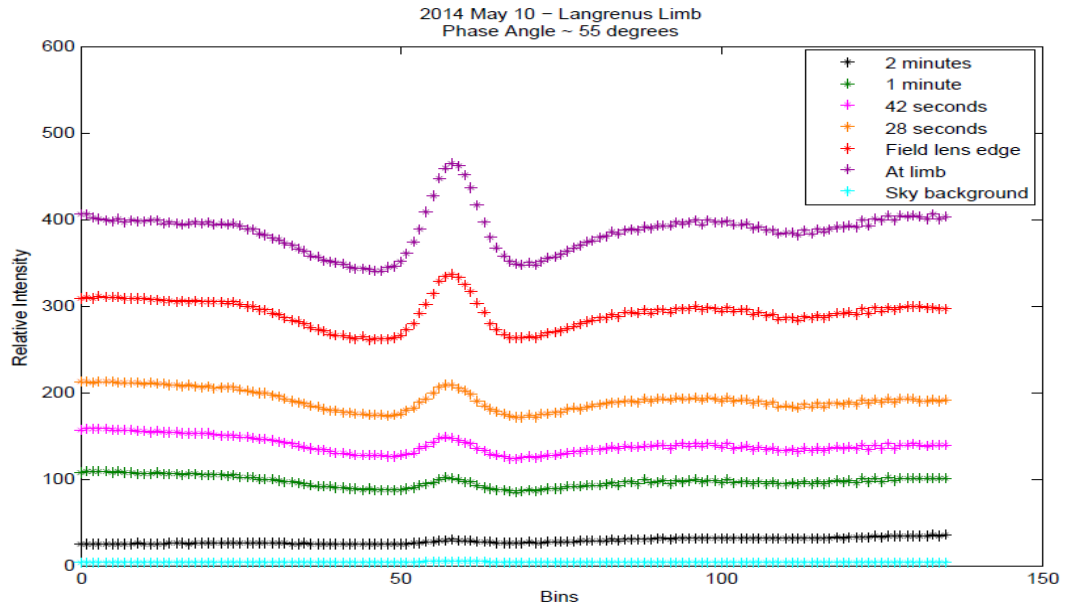


Figure 5.15: Relative intensity as a function of distance off the selenographic east limb from Langrenus crater on May 10, 2014. The highest sodium emissions are visible at observations taken close to the limb. This sequence was taken pre full Moon.

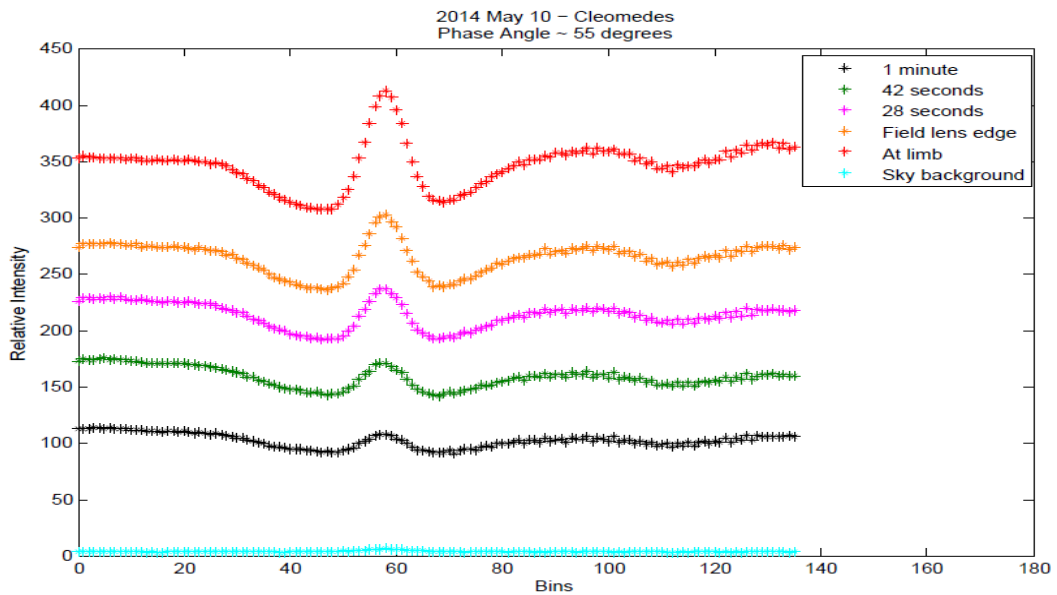


Figure 5.16: Relative intensity as a function of distance off the selenographic east limb from Cleomedes crater on May 10, 2014. An observation at 2 arcmin was not made for this crater. Strong sodium emissions are seen even at distances farther out from the limb.

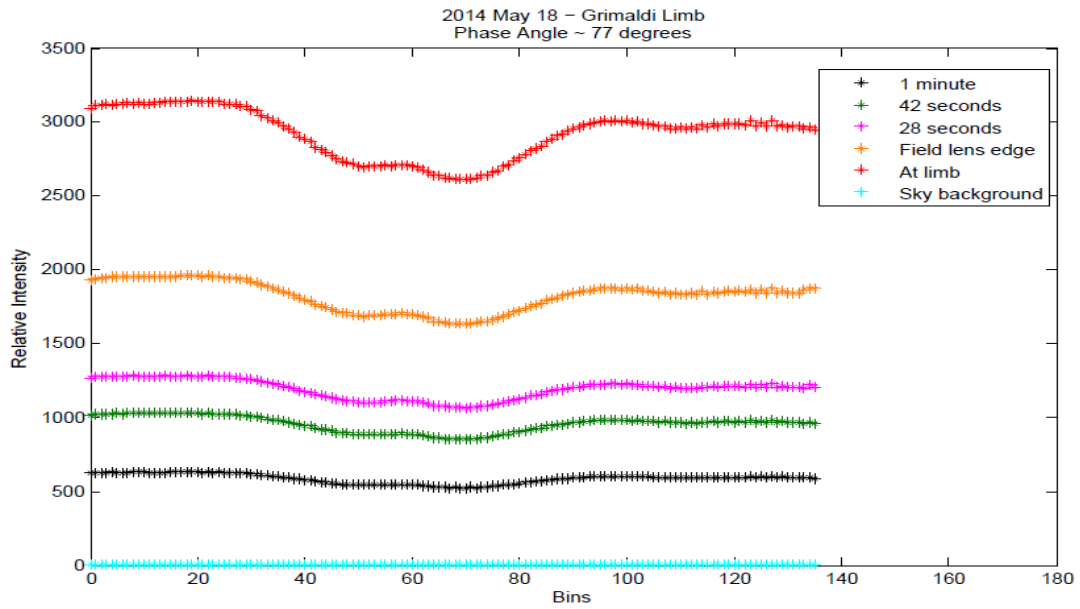


Figure 5.17: Relative intensity as a function of distance off the selenographic west limb from Grimaldi crater on May 18, 2014. An observation at 2 arcmin was not made for this crater. This sequence was taken post full Moon. The sodium emission is weak on this limb.

6. Discussion and Conclusions

A primary goal of my thesis was to collect ground based sodium and potassium data concurrent with the LADEE mission testing and science phase. As such, sodium and potassium data were collected over six observing runs (November 2013 – May 2014). The reductions, calibrations, and analysis of this extensive data set were discussed in earlier chapters. Here I discuss the morphology of the lunar sodium exosphere in the context of my seven month data set. My results are discussed in the context of existing literature, lunar missions such as LADEE and Kaguya, and are compared to potassium data, collected as part of this thesis.

6.1. Morphology of the Lunar Sodium Exosphere

6.1.1. Equatorial Regions

In order to assess the variability in observed sodium line widths, data collected over my 6 month period were grouped together in different ways including, as a function of phase, phase intervals, waxing and waning period, and day number.

The data are plotted as a function of phase in Figures 6.1 and 6.2. In Figure 6.1, negative phase angles represent pre full Moon data points (waxing phase) and positive phase angles represent post full Moon data points (waning phase). From Figure 6.1, it can be seen that the pre and post full moon data are nearly symmetric around the 0° phase angle, although the data taken pre full Moon have more scatter than data taken post full Moon. Going towards full moon the line widths increase, peaking near full. In terms of an

effective temperature the sodium exosphere appears hottest during magnetotail passage with phase angles $< 40^\circ$. Post full moon and post magnetotail passage, the line widths fall off towards higher phase angles. From Figure 6.2 it can be seen that for all the months, the pre full Moon and post full Moon line widths decrease as the phase angle increases. For both Figures 6.1 and 6.2, it can be seen that the line widths flatten out at phase angles $> 40^\circ$ for both waxing and waning phases. It seems likely this trend in line width is related to magnetotail passage.

Figures 6.1 and 6.2 exhibit a steep fall off in line width starting from small phase angles ($\sim 5^\circ$) towards higher phase angles ($\sim 40^\circ$). After phase angle 40° (and -40° for Figure 6.1), the line widths tend to flatten out instead of continuing to fall off steeply. This may be due to the Moon's position in its orbit, relative to its interaction with the Earth's magnetotail or due to viewing geometry. Note, for phase angles from 0 to approximately 40° , the Moon is inside the Earth's magnetotail (approximately 6 days). The Moon is outside of the Earth's magnetotail at phase angles larger than 40° .

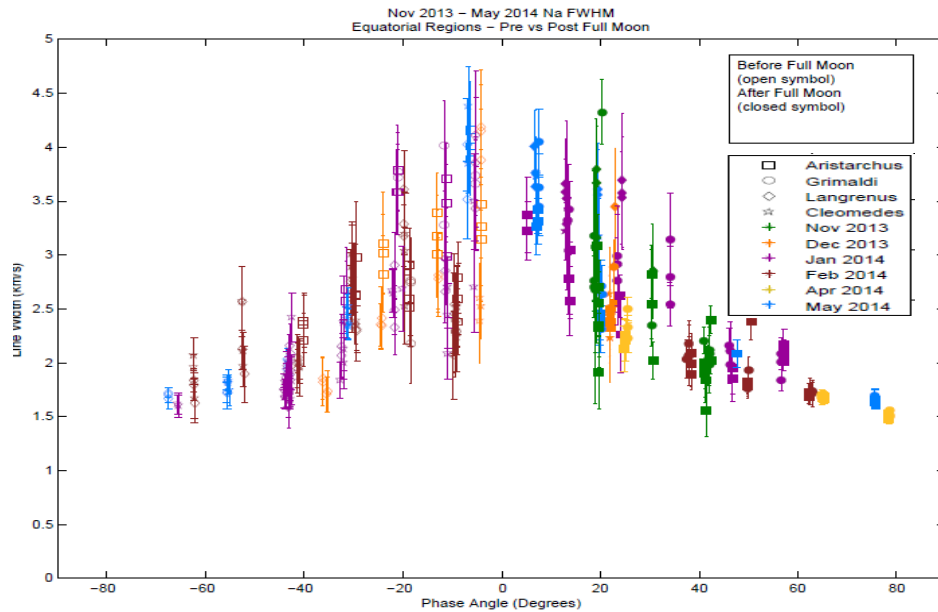


Figure 6.1: Equatorial FWHM as a function of phase angle for all data runs as found in Figure 6.2 with pre full Moon phases being negative. Data shown in this figure are for equatorial regions. Each offset crater is represented by a symbol as shown in the figure legend. The plot key depicts the symbols for each crater and color for each month.

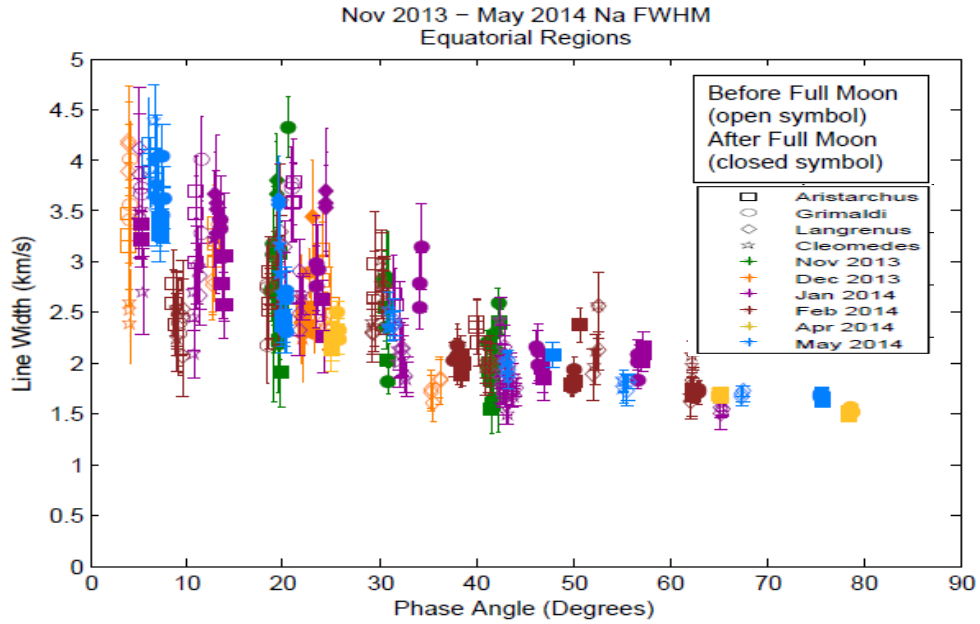


Figure 6.2: Equatorial FWHM as a function of phase angle for all data runs ranging from November 2013 – May 2014 for equatorial regions.

Table 6.1: Equatorial region line width derived effective temperatures averaged according to pre magnetotail passage ($> 40^\circ$), during magnetotail passage ($0 - 40^\circ$), post magnetotail passage ($> 40^\circ$) for all data runs.

Limb (selenographic)	Pre mag psg T (K)	Error (K)	Mag psg T (K)	Error (K)	Post mag psg T (K)	Error (K)	Max T mag psg (K)	Error (K)
Langrenus (east)	1790	164	4600	610	N/A	N/A	8770 (Dec 13)	2240
Grimaldi (west)	N/A	N/A	4320	440	1690	130	8190 (May 14)	1230
Aristarchus (west)	2600	62	4290	440	1710	120	8660 (May 14)	1860
Cleomedes (east)	1740	110	3980	350	N/A	N/A	9590 (May 14)	1610
Avg T for all data runs	2040	110	4300	460	1700	128		

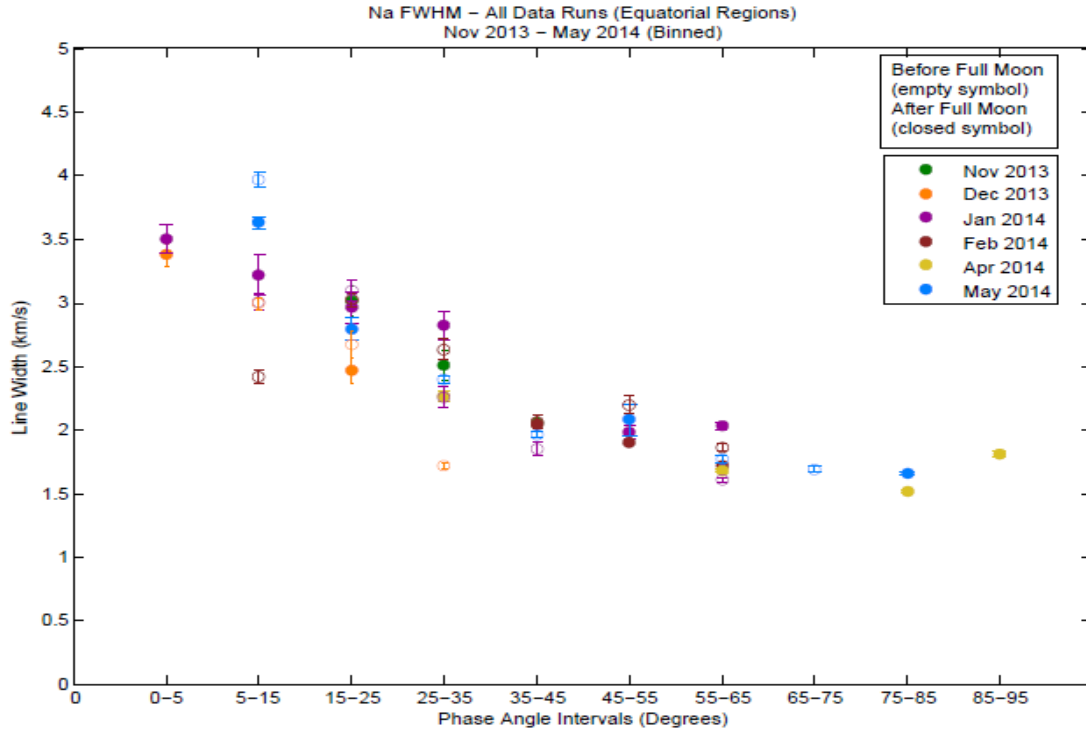


Figure 6.3: Sodium line widths as a function of phase angle for equatorial regions. Data points have been binned by intervals represented on the x-axis. The error bars are standard deviations of the errors of the data points contained within an interval.

Table 6.1 shows the average line width derived effective temperatures at different positions in the Moon's orbit for all data runs. The line widths, and thus derived temperatures, are highest while in the magnetotail with a value of 4300 ± 460 K. Line widths fall off towards higher phase angles with an average pre magnetotail temperature of 2040 ± 110 K and an average post magnetotail temperature of 1700 ± 128 K. Out of the four equatorial regions, the region off the Langrenus limb (selenographic east) has the highest temperatures during magnetotail passage while the regions off of the Aristarchus and Grimaldi limbs (selenographic west), are comparable in magnetotail passage temperatures. The highest temperatures for each of the four equatorial limb regions range from 8770 ± 2240 K to 9590 ± 1610 K with the highest magnetotail passage temperature belonging to the region off the Cleomedes limb. Overall, May 2014 (refer to Table 6.1) has the highest magnetotail passage temperatures.

The pre and post magnetotail passage temperatures are only slightly different from each other, with the post magnetotail passage temperature approximately 300 K lower. The pre full Moon data show more scatter than the post full Moon data, as was seen in previous figures, with pre full Moon data having slightly higher line widths than their post full Moon counterparts. The trend reported by Mierkiewicz et al. (2014) of highest temperatures during full Moon period agrees with data taken during the six month period presented here. The temperatures observed by Mierkiewicz et al. (2014) range from 3260 ± 190 K near full Moon to 1000 ± 135 K at a phase angle of 42° .

The magnetotail passage temperatures quoted for the results of this thesis are higher than temperatures seen by Mierkiewicz et al. (2014), but the pattern of decreasing temperatures towards large phase angles is consistent with their results and the scale height derived temperature results presented by Potter et al. (2000). Potter et al. (2000) measured a high temperature of 2900 K during full Moon phase (phase angle 4.3°) and saw a decrease in temperature to 1400 K at larger phase angles (phase angle $50 - 76^\circ$). Their data also suggested that the decrease in scale height derived exospheric temperatures occurred more rapidly during the waxing phase than the waning phase. The line widths presented in Figures 6.1 - 6.3 flattens out after a phase angle of 40° and the data presented by Potter et al. (2000) suggested that the temperature flattens out around 37° phase angle, indicating that the tendency for the temperature to flatten out after a phases greater than $\sim 40^\circ$ is apparent both in this study and theirs. Figure 6.4 shows the global data presented in Figure 6.2 with the addition of scale height - derived temperatures by Potter et al. (2000) and Mierkiewicz et al. (2014). The waxing and waning phase derived temperatures of Potter et al. (2000) agree with the lower range of our line width derived effective temperatures as seen in Figure 6.4. The waning phase scale height derived temperatures of Potter et al. (2000) at phase angles higher than 40° agree very closely with the large phase angle line width derived temperatures. This is in partial agreement with the results of Mierkiewicz et al. (2014) which showed that the scale height derived temperatures of Potter et al. (2000) only agreed with their waxing phase line width derived temperatures.

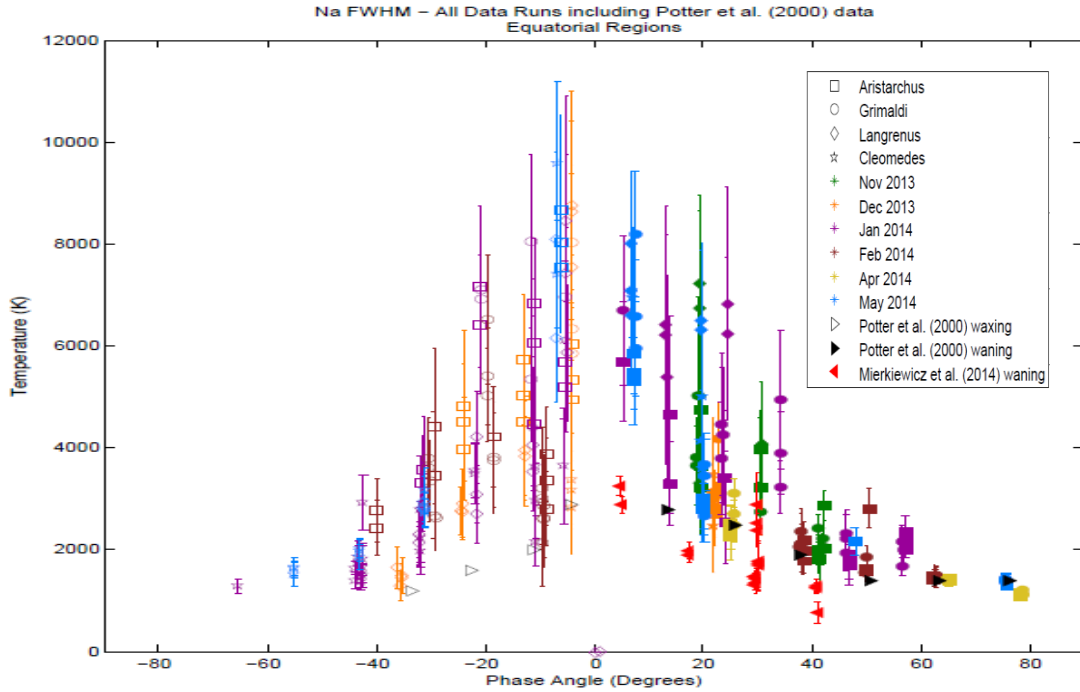


Figure 6.4: Global equatorial sodium data converted to line width derived effective temperatures and plotted along with results from Potter et al. (2000) and Mierkiewicz et al. (2014). Negative phase angles depict waxing phases.

6.1.2. High Latitude Regions

For the high latitude regions (Figure 6.5), the falloff in line width is less defined than for the equatorial regions. While there is an overall decrease in line width going towards high phase angles, there are some measurements towards phase angles of $\sim 50 - 65^\circ$ that exhibit anomalous behavior. These anomalous data points are $\sim 50\%$ wider than would be expected at high phase angles and do not clearly fit the equatorial phase angle trend of line width decreasing towards high phase angles.

When plotting waxing and waning phases, seen in Figure 6.6, the pre full Moon data exhibits more scatter than post full Moon data, similar to the equatorial region data. The high latitude data is however not as symmetric about the center as seen for the equatorial regions. Except for a few anomalies, the line widths follow the trend of becoming large towards magnetotail passage, are largest around full Moon (small phase angles), and fall off post magnetotail passage (large phase angles). The trend of decreasing line widths, and thus derived effective temperatures, towards high phase

angles is consistent with the equatorial results discussed earlier. While for the equatorial regions, the line widths flattened out after a phase angle of about 40° , the flattening of line widths at phase angles $> 40^\circ$ is not as well defined for the high latitude regions. From Figure 6.7, the pre full Moon line widths have more scatter and are larger than their post full Moon counterparts. This pattern is consistent with what was seen in the equatorial regions.

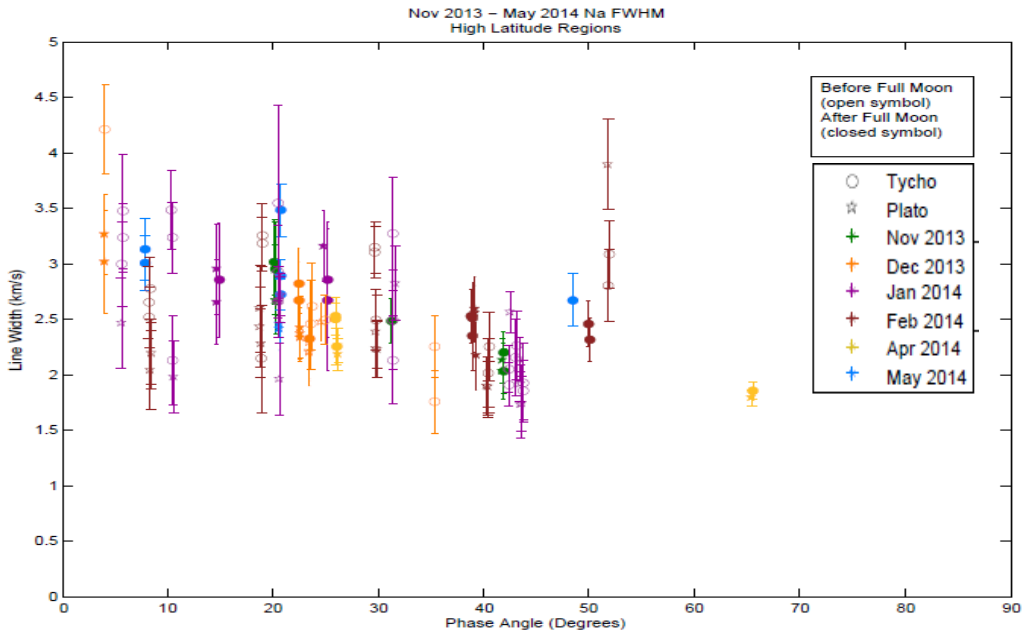


Figure 6.5: FWHM as a function of phase angle for all data runs ranging from November 2013 – May 2014 for high latitude regions. Each offset crater is represented by a symbol as shown in the figure legend.

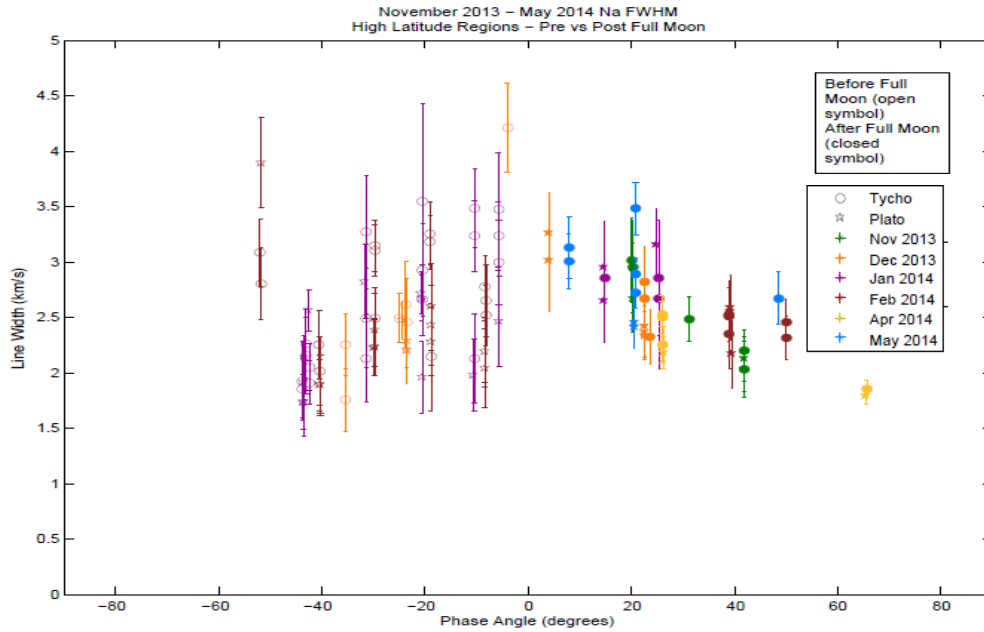


Figure 6.6: FWHM as a function of phase angle for all data runs as found in Figure 6.1 with pre full Moon phases being negative. Data shown in this figure are for high latitude regions.

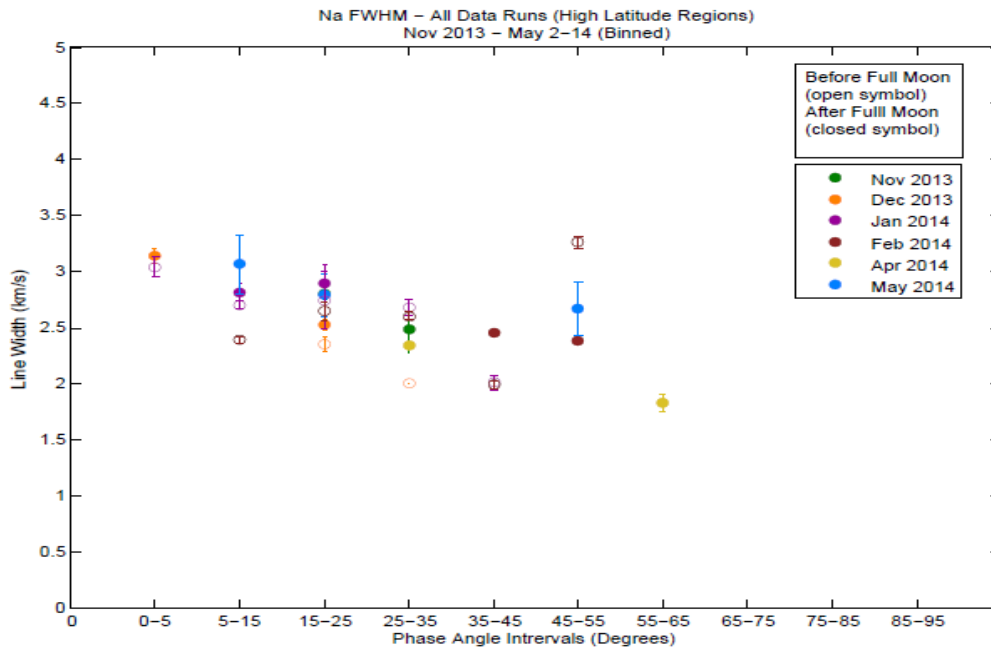


Figure 6.7: Sodium line widths as a function of phase angle for high latitude regions. Data points have been binned by intervals represented on the x-axis. The error bars are standard deviations of the errors of the data points contained within an interval.

Table 6.2 shows average temperatures for the high latitude regions for all data runs, designated by the position of the Moon in its orbit. The temperatures are highest during magnetotail passage with the south limb (off Tycho) having the highest value of 3940 ± 500 K. The pre magnetotail passage (waxing phase) average temperature for all data runs is 2590 ± 290 K and the post magnetotail passage (waning phase) temperature is 2180 ± 170 K , with magnetotail passage temperature of 3520 ± 490 K.

Our observed temperatures are consistent with results presented by Kagitani et al. (2010) from the Kaguya polar lunar orbiter. Kagitani et al. (2010) concluded in their study that the lunar sodium exosphere on the lunar nightside has a spherical symmetric distribution with a temperature range of 2400 – 6000 K. Their temperatures were obtained by fitting line of sight emission intensities taken over a six month period to model emission intensities. The line width derived effective temperatures presented here for the high latitude (polar) regions are consistent with the Kaguya results.

Table 6.2: High latitude region line width derived effective temperatures averaged according to pre magnetotail passage ($> 40^\circ$), during magnetotail passage ($0 - 40^\circ$), post magnetotail passage ($> 40^\circ$) for all data runs.

Limb	Pre mag psg T (K)	Error (K)	Mag psg T (K)	Error (K)	Post mag psg T (K)	Error (K)	Max T mag psg (K)	Error (K)
Tycho (south)	2600	190	3940	500	2750	210	6290 (Jan 14)	3100
Plato (north)	2600	380	3100	490	1600	130	5330 (Dec 13)	1180
Avg T for all data runs	2590	290	3520	490	2180	170		

6.1.3. Monthly Variations

The line widths as a function of day number, as seen in Figure 6.8 and Figure 6.9, exhibit an increase towards full Moon and a decrease post full Moon. The rise and fall in line width is a monthly pattern and could indicate seasonal variations of the sodium exosphere. May 2014 has the highest line widths during magnetotail passage among all the data and is followed by January 2014, making them the hottest months observed. Note, the fall off in line width post full Moon in May is steep compared to other months.

The high latitude regions shown in Figure 6.9 do not exhibit a monthly distinctive rise and fall in line width. In the February 2014 high latitude regions, there are some anomalous data points pre full Moon that have line widths that are higher than line widths during magnetotail passage. This does not fit the pattern of having the highest temperatures during full Moon.

The lunar surface temperature is approximately 400 K and the results presented here, along with scale height derived temperatures by Potter et al. (2000), Potter and Morgan (1988), Sprague et al. (1992) and others (see the Table 1 in Sarantos et al. (2010) and the review by Stern (1999)), are higher than what is expected for sodium atoms thermalized to the lunar surface. This may be indicative of an energetic process that liberates sodium atoms into the exosphere, such as PSD. The expected temperature of a PSD source is around 1200 K (Sarantos et al., 2010; Madey et al., 1998) ignoring the tail of non-thermal neutrals (Sarantos et al., 2010; Yakshinskiy et al., 1999; Madey et al., 1999). The pre and post magnetotail passage temperatures presented here can, in part, be due to a non-thermal source mechanism such as PSD. Temperatures during magnetotail passage are as high as 4600 K for the equatorial regions and 3940 K for the high latitude regions.

These high temperatures may also be a result of viewing geometry, as suggested by Potter et al. (2000) and Mierkiewicz et al. (2014). The Moon has a sodium tail and around full Moon, the observed line of sight is down this tail. When looking down the sodium tail, the assumption that the lunar exosphere is spherically symmetric is not valid. In this viewing geometry a larger fraction of sodium atoms with a higher red shift may be

observed, making the observed line widths broader and resulting in higher derived effective temperatures. Although, this red shifted Doppler line component near full Moon should be detectable as a distinct red wing, such an observed asymmetry has not been detected. This could simply mean that the effect of looking down the tail is minimal, but without models it is difficult to make a careful assessment. Another reason for high temperatures could simply be due to increased scattered light during full Moon, raising the continuum level and causing the emission line to become broader.

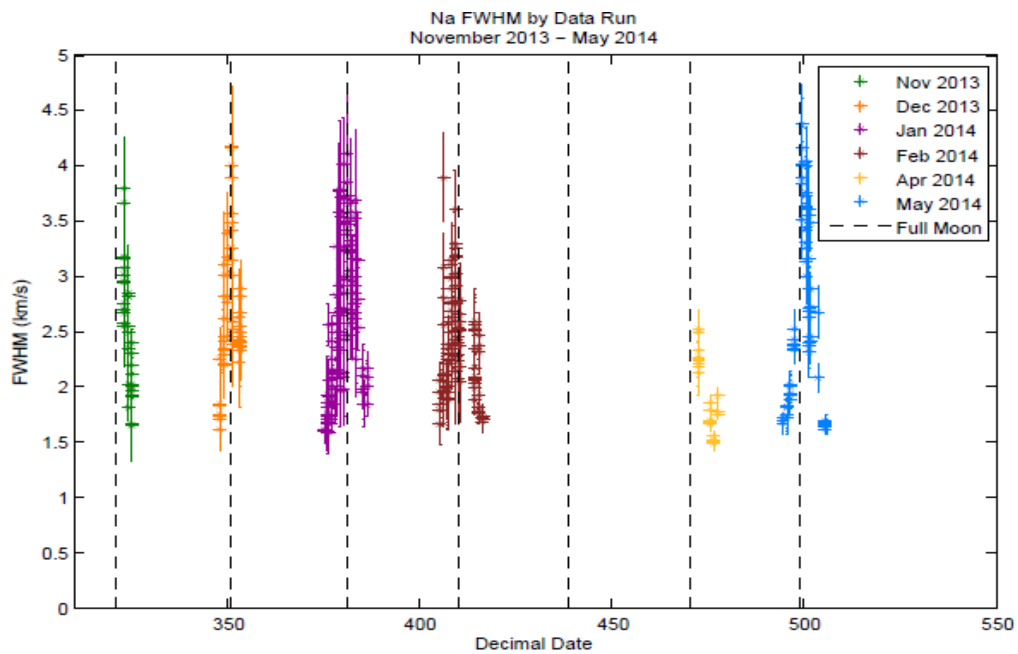


Figure 6.8: FWHM as a function of day number from November 2013 – May 2014 including both equatorial and high latitude regions. The dotted black lines mark full Moon dates for each month.

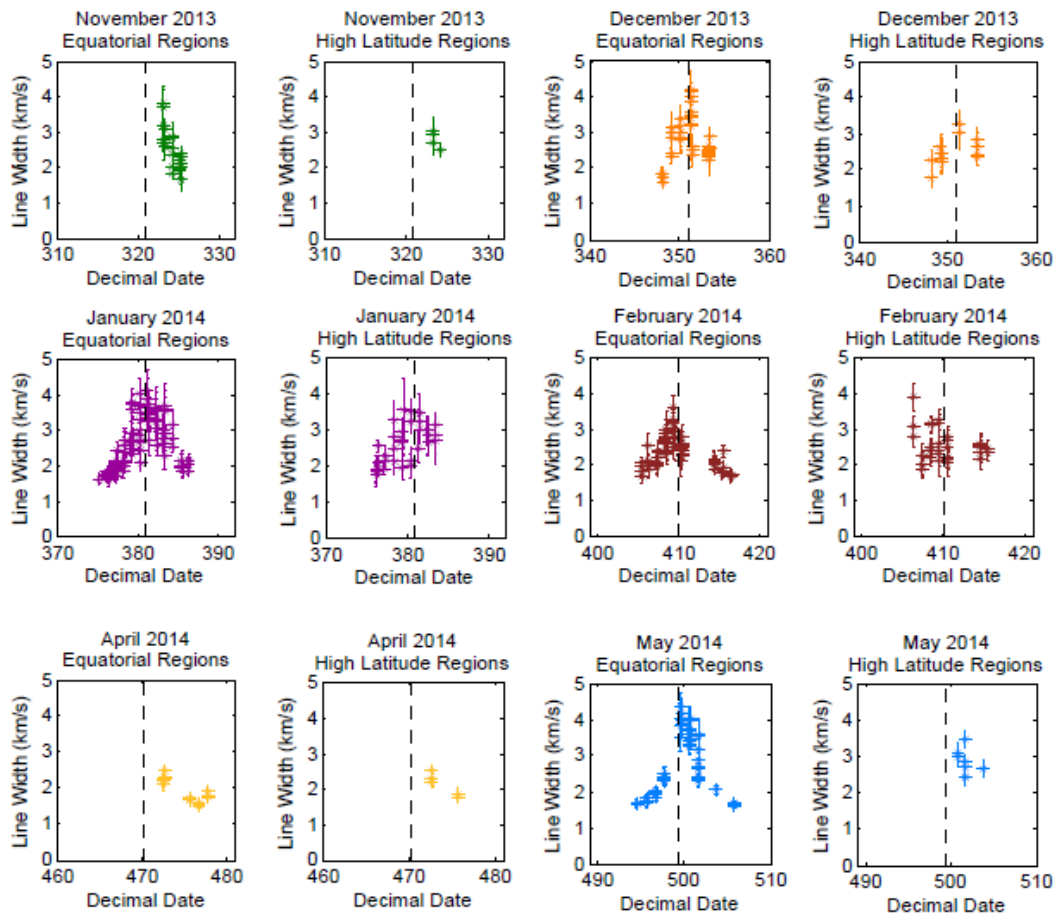


Figure 6.9: FWHM as a function of day number as seen in Figure 6.8, seperated into equatorial and high latitude regions.

6.2. Relative Intensity Trends for Sodium

The relative intensities, as seen in Figure 6.10 and 6.11, are taken at approximately full Moon +/- 4 days, with the highest values post full Moon. The highest relative intensities were recorded in January and February while April is the least bright month. December and May are comparable in brightness. The rise and fall pattern seen for the line widths (Figures 6.8 and 6.9) is not as apparent for the relative intensities. While the line widths peak during full Moon period, relative intensities exhibit varying patterns for each month as seen in Figure 6.11.

In Figure 6.12 the limb intensities are plotted by month. The data set was restricted in order to isolate near surface trends more clearly. For the equatorial regions, in November 2013, the relative intensity falls off post full Moon. In December 2013, the relative intensity becomes brighter post full Moon and then slightly falls off. In January 2014, the relative intensity decreases towards full Moon, increases during and after full Moon but does not fall off afterwards; the same is seen for February 2014. In April 2014, the relative intensities increase shortly after full Moon and then start to decrease. It is difficult to establish an exact pattern for this month due to insufficient data. In May 2014, the relative intensities decrease towards full moon and increase after full Moon. Shortly after full Moon, the relative intensities fall off rapidly and rise again towards the end of the May run. The rapid fall off in relative intensity post full Moon, is not seen in any other months.

The overall pattern that is consistent for all the months is that the relative intensities are highest right after full Moon. This may be indicative of the role plasma sheet ions play in bringing sodium atoms to the surface. As mentioned in Chapter 1, plasma sheet ions can enhance the efficiency of PSD two times more than solar wind ions (Sarantos et al., 2010). Energetic plasma sheet ions may help bring the sodium atoms to the surface and upon exiting the magnetotail, these atoms can be knocked off the surface by PSD. The lack of pre full Moon data in November 2013 and April 2014 makes it difficult to confirm this pattern for these two months, however.

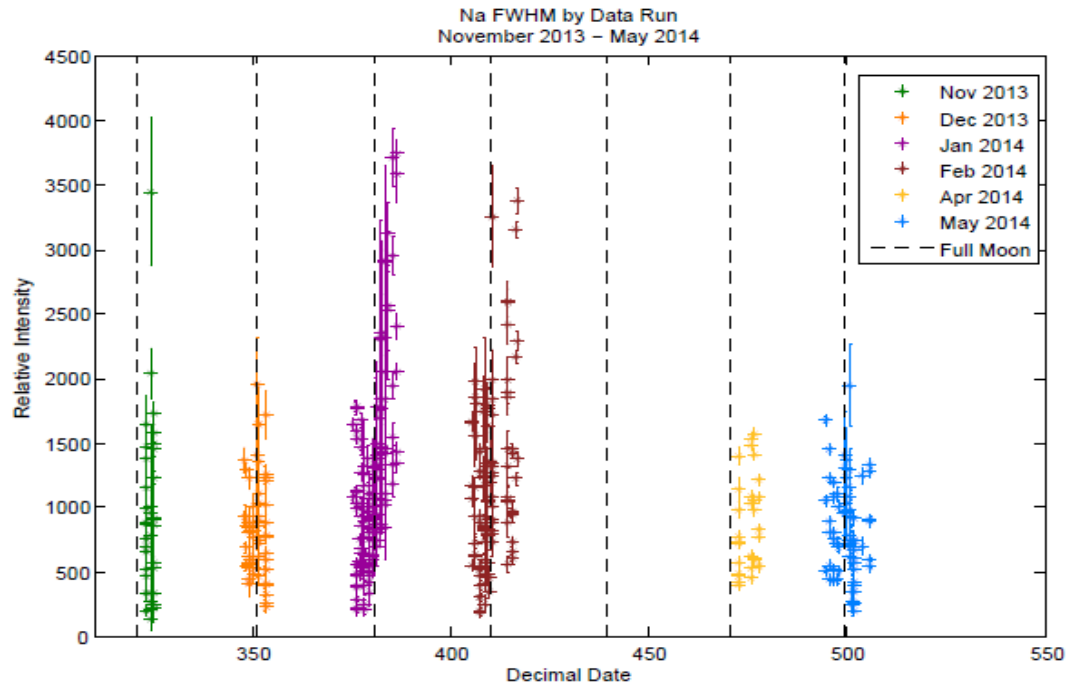


Figure 6.10: Relative intensity as a function of day number for all data runs from November 2013 – May 2014 including both equatorial and high latitude regions. The dotted black line marks full Moon dates for each month.

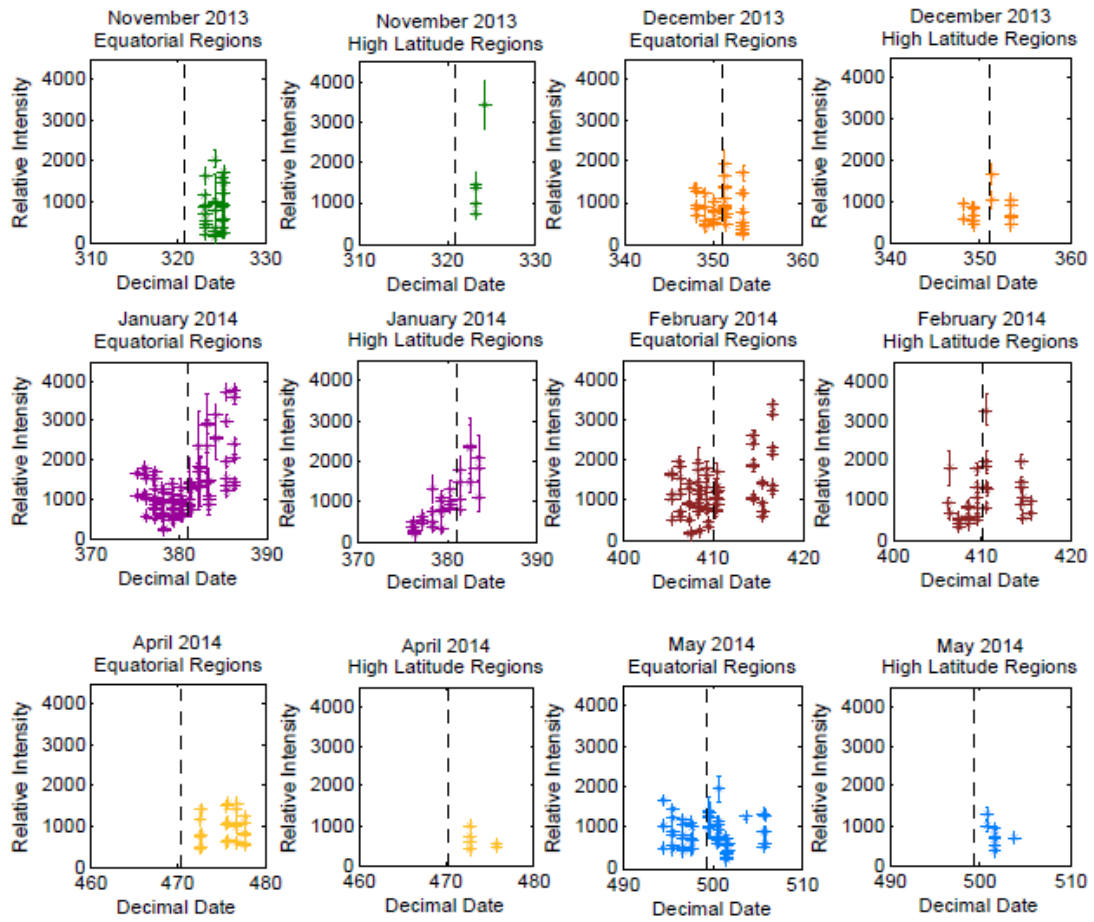


Figure 6.11: Relative intensity as a function of day number as seen in Figure 6.11 separated into equatorial and high latitude regions.

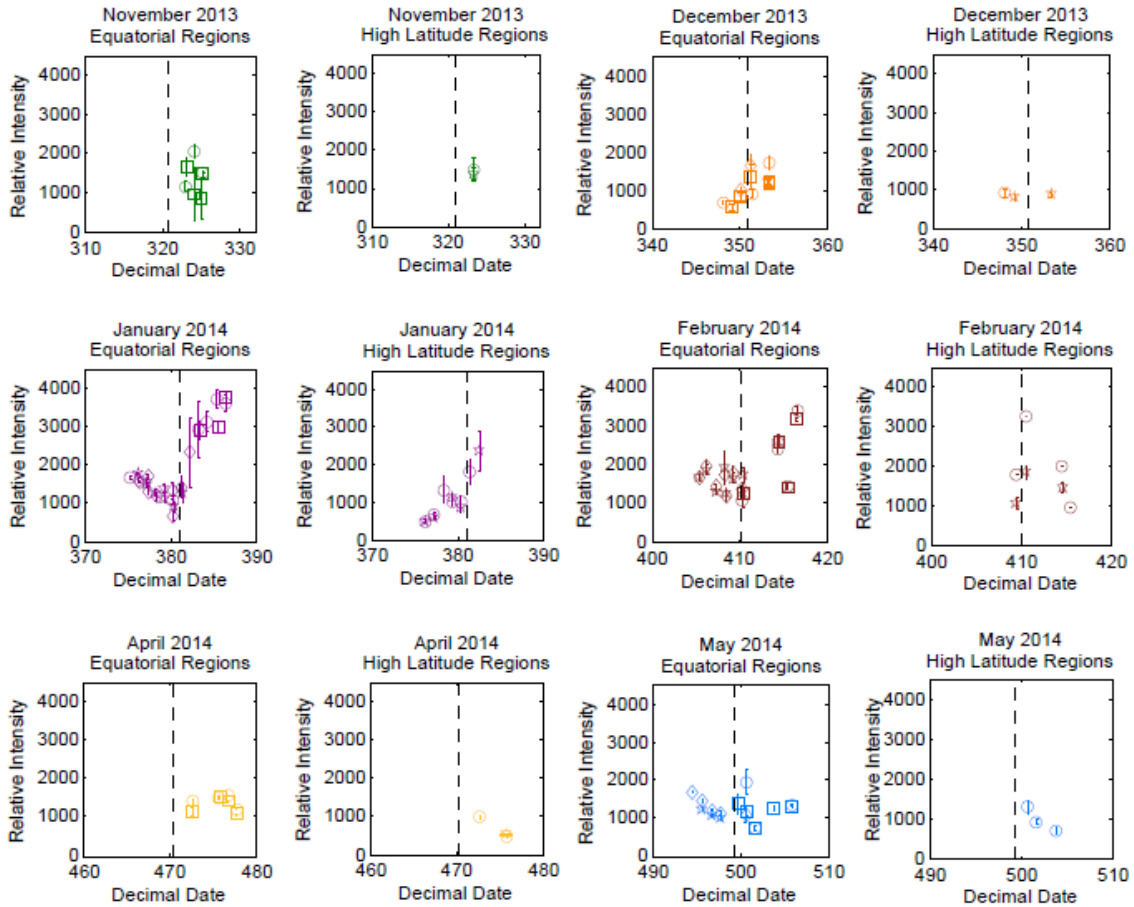


Figure 6.12: Relative intensity as a function of day number for all data runs for data points taken at the limb.

The distinctive patterns seen by month for the relative intensity could also be a result of the Sun-Moon radial velocity. Variation in the Sun-Moon radial velocity can cause the sodium atoms to see varying levels of sunlight. The continuum level that the atoms see depends on how far up the Fraunhofer line the sodium emission line moves. This movement of the emission line will cause variations in intensity as the sodium encounters more solar photons. The Sun-Moon radial velocity needs to be accounted for, before any seasonal variations in the lunar sodium exosphere can be established.

Smyth and Marconi (1995) presented models for the sodium and potassium atmosphere of the Moon. Smyth and Marconi (1995) concluded that the radiation acceleration produced by resonance scattering of sunlight by both sodium and potassium

atoms was an important factor in the transport and gravitational escape of source atoms. Furthermore, they also concluded that since the magnitude of the radiation acceleration depends upon the Doppler shift out of the Fraunhofer absorption features in the solar spectrum, it also varies with radial motion and distance of the Moon from the Sun as well as the instantaneous velocity of sodium and potassium atoms relative to the Moon. From their model results, this variability of the radiation acceleration produces an expanded sunward atmosphere with an enhanced escape of gas in the antisunward lunar coma during the first quarter in the spring. Likewise, in the fall at last quarter, the radiation acceleration produces a contracted sunward atmosphere with a reduction in the escape of gas in the antisunward coma.

This seasonal variation in the escape of gas in the antisunward coma might explain the patterns seen in the relative intensity results I've presented here. The solar radiation acceleration decreases from spring toward summer, and then increases leaving summer into fall (Smyth and Marconi, 1995). The relative intensities in Figure 6.10 and 6.11 also decrease from January 2014 towards May 2014 in a similar manner. In Figure 6.10 the relative intensities in November 2013 and December 2013 are overall lower than the relative intensities in January – May 2014. The Sun-Moon radial velocity will need to be considered for the relative intensity data presented here for the time span of November 2013 – May 2014 in order to make a more definite conclusion.

Figure 6.13 shows relative intensity at the limb as a function of day number for May 2013 and May 2014. Comparing the May 2013 limb intensities to the May 2014 limb intensities (Figure 6.13), it can be seen that they are similar to each other. The equatorial data for May 2013 looks flat overall, same as in May 2014. For the high latitude regions, the exponential like decrease in limb intensities after full Moon in May 2013 is also seen in the May 2014 data.

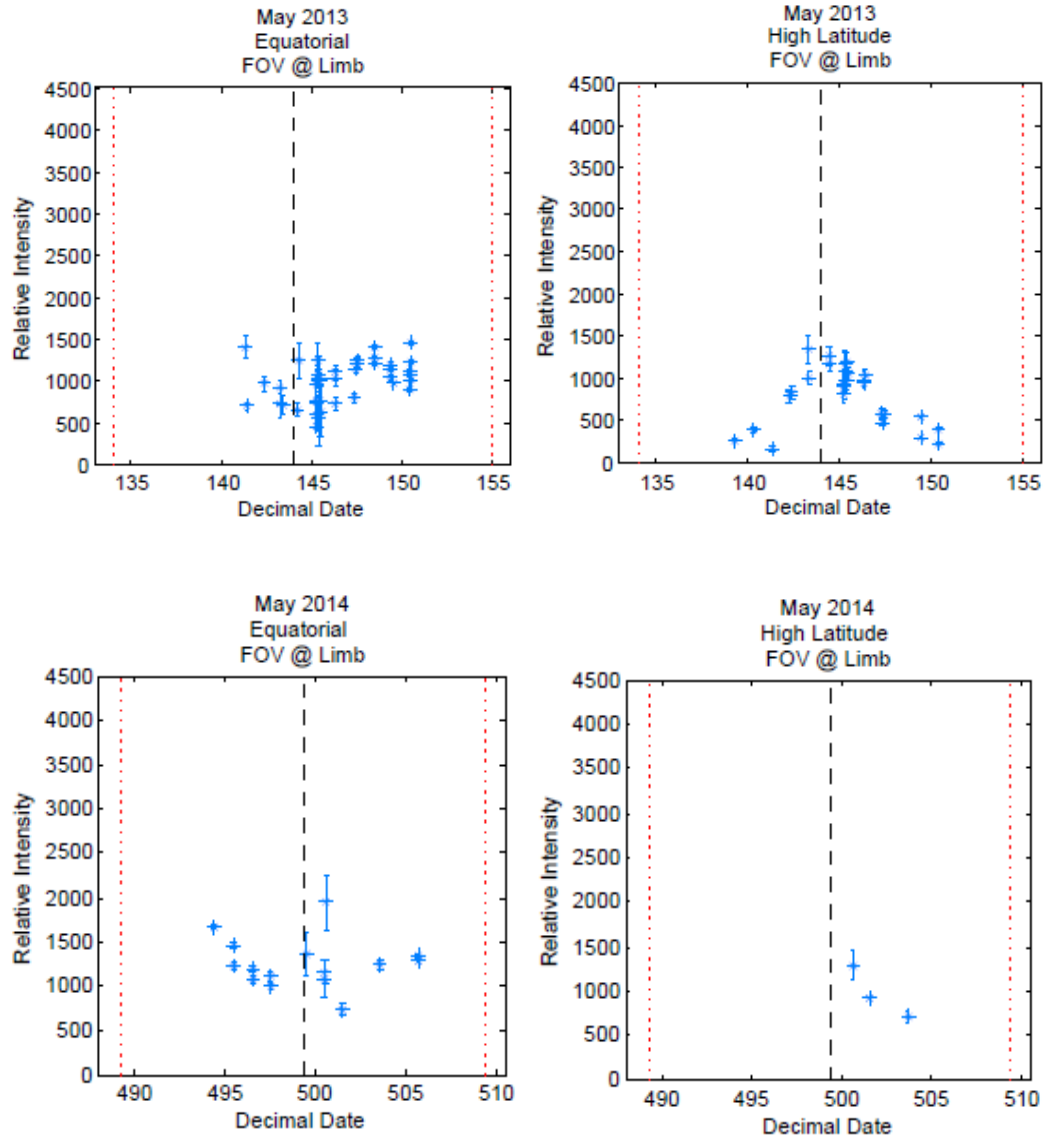


Figure 6.13: Relative intensity for equatorial and high latitude regions for May 2013 and May 2014.

6.2.1. Our Observations in the Context of LADEE and Kaguya Sodium Results

The LADEE mission was launched on September 7, 2013 (UTC) and entered into lunar orbit on October 6, 2013 (UTC). The mission had a 128 day science phase and ended in a planned crash onto the far side of the moon on April 18, 2014 (UTC). My data set is concurrent with the LADEE mission instrument testing and science phase.

The LADEE mission orbited near the lunar equator, so preliminary LADEE total column density results are compared with my equatorial region relative intensity data (Section 6.2). LADEE column density measurements indicate January and February as the months with the highest observed sodium column density (Colaprete et al., 2014; Colaprete et al., 2014; Colaprete et al., 2015). My relative intensity data (Figures 6.10 and 6.11) is consistent with this LADEE result, with January and February data sets recording the highest observed relative intensity. In addition, LADEE column density measurements indicate a fall off in density from January through April; this trend is also seen in my data (Figures 6.10 and 6.11). LADEE data also indicate increases in sodium column density after the Geminids meteor shower (Colaprete et al., 2014). Such an increase is not apparent in my data set (Figures 6.10 and 6.11).

Figure 6.14a shows the Kaguya polar orbiter results for the variation of sodium surface density over a period of six months; Figure 6.14b shows the variation of sodium surface density due to phase angle (Kagitani et al., 2010). The month with the highest surface density of sodium atoms is February, meaning that it is the brightest month. The high latitude regions show the highest relative intensities in January and February 2014, as seen in Figure 6.11. Both of these months are comparable to each other, for the high latitude regions. For a more direct comparison, the data presented here will need to be converted to absolute intensities, which may cause the final intensity results to be different from the relative intensity results shown here. The trend of relative intensities falling off towards May (Figures 6.10 and 6.12) is consistent with the surface density trends seen in Figure 6.14a from February to May. Both figures show a fall off towards May, with May having larger values than April. Note that, our observed high latitude temperatures are consistent with the Kaguya results that showed that the lunar sodium

exosphere on the lunar nightside has a spherical symmetric distribution with a temperature range of 2400 – 6000 K (Kagitani et al., 2010).

The variation of surface density of sodium atoms as a function of lunar phase angles show that the sodium density decreased going from 1st quarter (phase angle 90°) to 3rd quarter (phase angle 270°). It is hard to make direct monthly comparisons due to phase coverage not being the same as the Kaguya monthly phase coverage. From Figure 6.12 limb relative intensity data, the months of May and April see a fall of relative intensity post full Moon. This is observed in Figure 6.14b for the months of May and April as well.

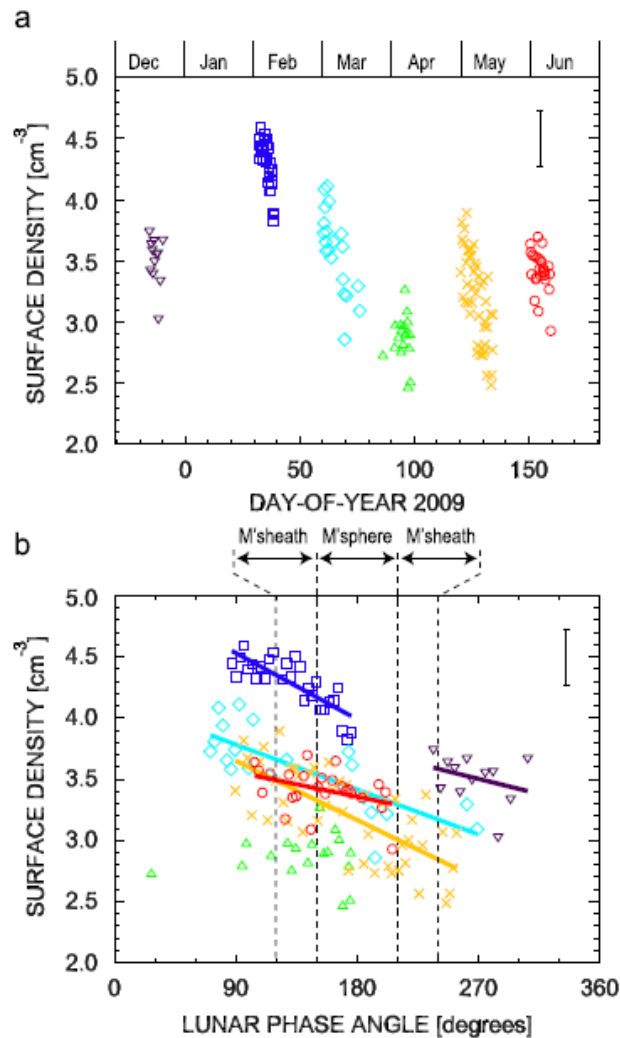


Figure 6.14: Variation in surface density of sodium atoms during day-of-year in 2009 (a) and variation in surface density of sodium atoms as a function of phase angle (b) (Kagitani et al. 2010).

6.3. Global Trends of Potassium

6.3.1. Line Width FWHM

Potassium data was collected along with sodium during my observing runs at the MMP. Reduction and processing of the potassium data was carried out by Nick Derr (University of Wisconsin). Figure 6.15 shows pre full Moon phase line widths for observations off Langrenus and Cleomedes (selenographic east limb) that are larger than the post full Moon line widths for observations off Grimaldi and Aristarchus (selenographic west limb). Note that observations off Langrenus and Cleomedes are visible during waxing phase and observations off Grimaldi and Aristarchus are visible during waning phase. All these offset craters are visible at full Moon, however as seen in Figures 6.15 – 6.17, potassium emissions are difficult to detect during full Moon phase (small phase angles $\sim 5\text{-}10^\circ$).

Unlike sodium, potassium seems to disappear near full Moon (around 30° phase angle) and reappear a few days after full Moon. The April 2014 data, presented in Figure 6.16, contains no data for Langrenus and Cleomedes offsets. Plato offset directions (north limb) have larger line widths than Tycho offsets (south limb). Grimaldi and Aristarchus limb line widths increased towards large phase angles ($> 75^\circ$) in February and April. Figure 6.17 shows that the Langrenus and Cleomedes offset directions have larger line widths, and are thus hotter than Grimaldi and Aristarchus offsets in May 2014. This is consistent with February 2014 observations.

During magnetotail passage, the lunar surface is primed by plasma sheet ions. Outside of the magnetotail, the lunar surface is primed by solar wind particles, which according to Sarantos et al. (2010), is only half as effective in increasing PSD efficiency as compared plasma sheet ions. This could mean that the decrease in temperature post magnetotail passage, during waning phase, might be the result of PSD depleting the lunar potassium exosphere and thus reducing the exospheric temperature. The lower temperatures on the selenographic west side might also be due to location. The selenographic east limb temperatures (Langrenus and Cleomedes) are also hotter for sodium data.

On average, the potassium line widths are lower than the sodium line widths for all data runs. This may be due, in part, to potassium's smaller scale height compared to sodium (due to its higher mass). As such, observed potassium distributions are closer to the lunar surface. Potassium also has a smaller scattering cross section than sodium, meaning that it is less affected by solar radiation pressure and thus has no tail. For sodium, looking down the tail may be a possible explanation for temperatures higher (> 4000 K) than a PSD dominated source (1200 K). Since potassium has no tail and is not detected during full Moon, temperatures much larger than what is expected for a PSD source are not observed. The potassium line width derived temperatures are closer to the temperature of a PSD mechanism than sodium line widths. Note that unlike sodium, potassium line widths are much higher ($\sim 50\%$) during waxing phase than waning phase at phase angles $> 40^\circ$.

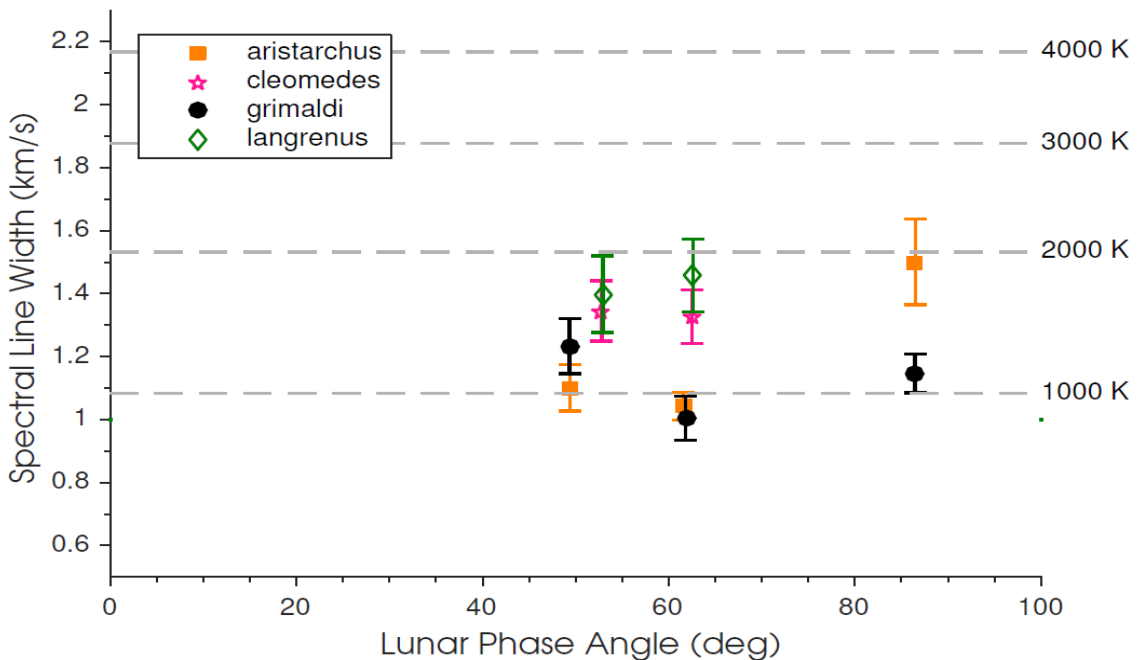


Figure 6.15: Potassium line widths for February 2014 as a function of phase angle. This Figure contains only equatorial limb data.

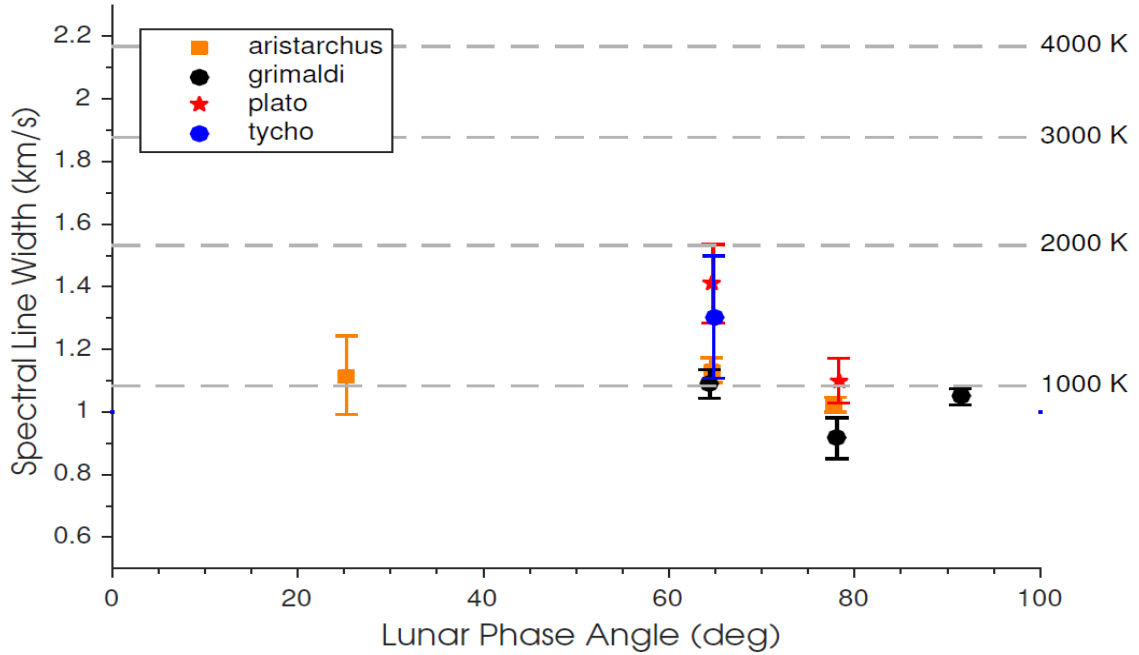


Figure 6.16: Potassium line widths for April 2014 as a function of phase angle. This Figure contains both equatorial and high latitude data.

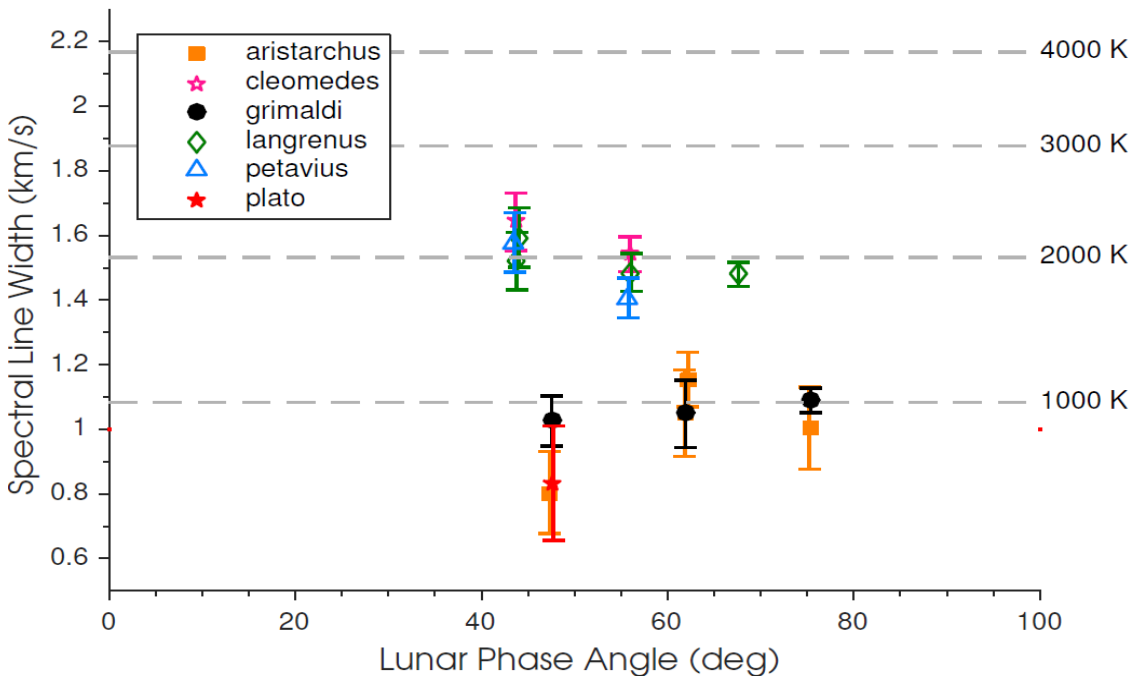


Figure 6.17: Potassium line widths for May 2014 as a function of phase angle. This Figure contains both equatorial and high latitude data.

6.3.2. Relative Intensity Trends for Potassium

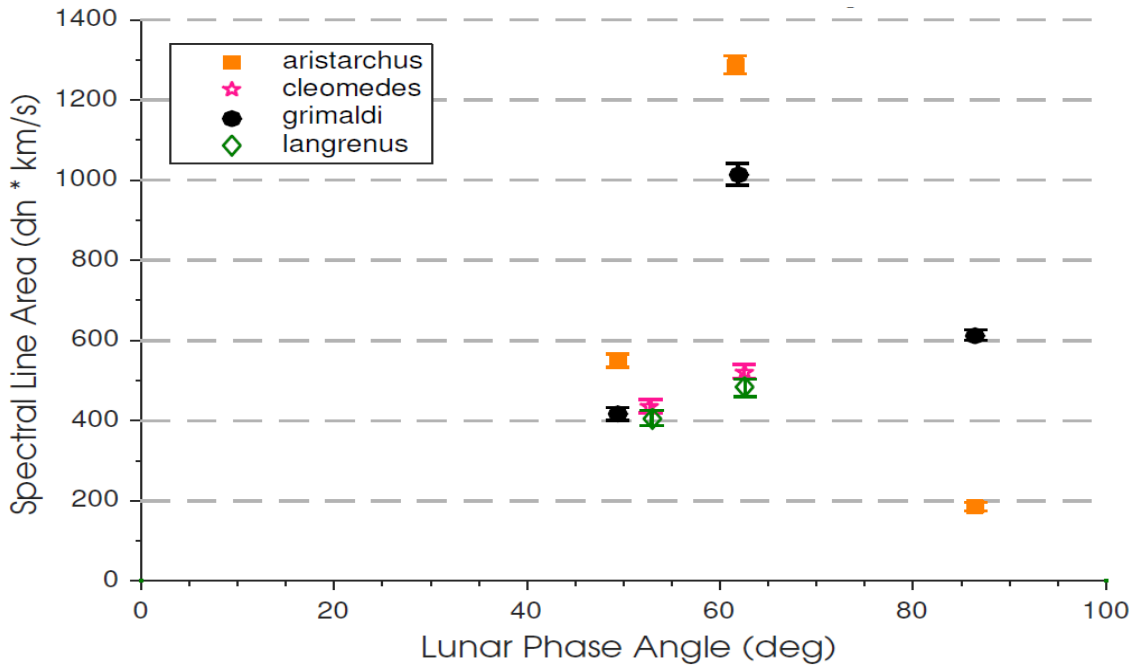


Figure 6.18: Potassium area (relative intensity) as a function of phase angle for February 2014. The y-axis is in units of relative intensity.

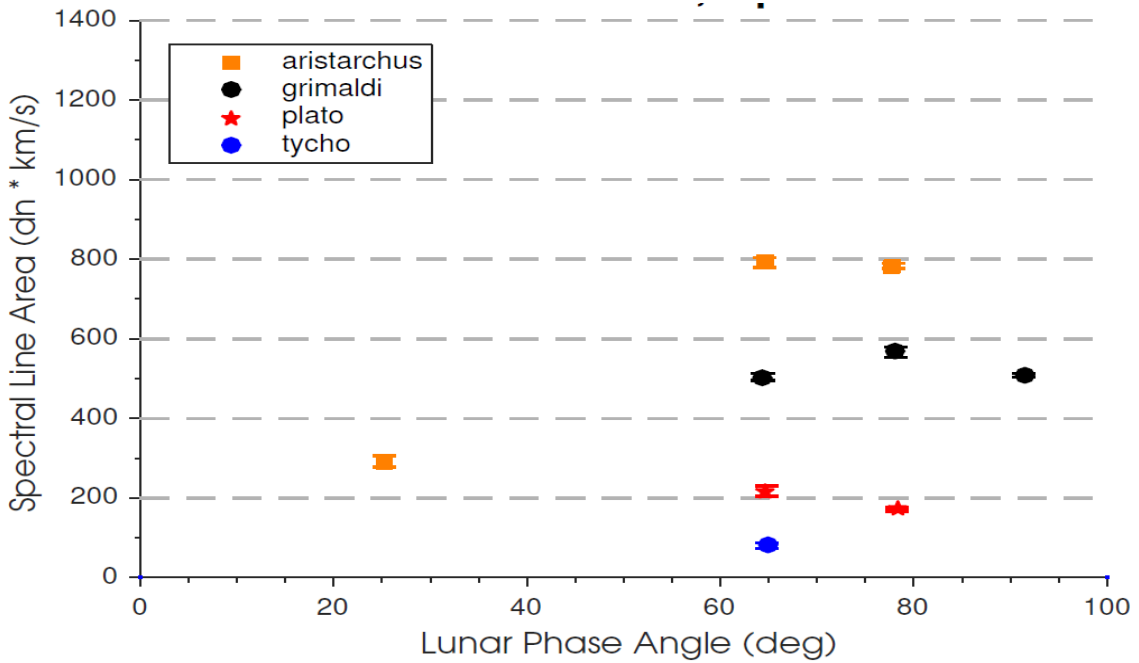


Figure 6.19: Potassium area (relative intensity) as a function of phase angle for April 2014. The y-axis is in units of relative intensity.

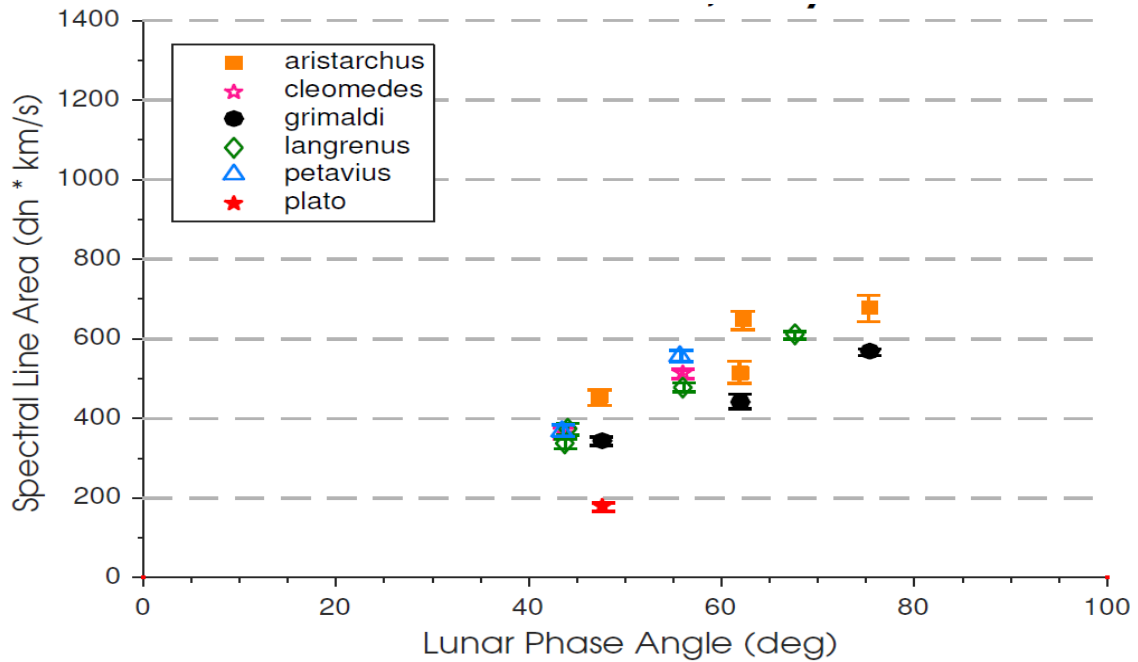


Figure 6.20: Potassium area (relative intensity) as a function of phase angle for May 2014. The y-axis is in units of relative intensity.

The observed potassium emission line intensity is shown in Figures 6.18 – 6.20. From Figures 6.18 and 6.20, it can be seen that the selenographic west limb (Grimaldi and Aristarchus) is on average brighter than the selenographic east limb (Langrenus and Cleomedes). From all three figures, it can be seen that the Aristarchus limb is brighter than all other offset craters, with the exception of the data point at $\sim 90^\circ$ during February 2014. This could be evidence for the KREEP region discussed in Chapter 1. The KREEP region is concentrated near Aristarchus crater, meaning there may be a larger abundance of potassium atoms in this region. This large abundance of potassium atoms concentrated near Aristarchus is a possible explanation for why observations off Aristarchus have areas that are brightest among all crater offsets. Note, we have noticed that potassium is much brighter when it is detected post magnetotail passage as compared to pre magnetotail passage brightness.

6.4. Conclusions

My work has led to an extensive and unique set of data to study the morphology of the lunar sodium and potassium exosphere. In this thesis I've described this work and now highlight my conclusions: (1) The line widths are largest, and temperatures hottest, during magnetotail passage (phase angle $0 - 40^\circ$). (2) Line widths are approximately constant at phase angles larger than 40° , which could be indicative of when the Moon is entering and exiting the Earth's magnetotail. (3) The selenographic east limb (waxing phase) is hotter than the selenographic west limb (waning phase), perhaps as a result of location or due to plasma sheet ions priming lunar surface and increasing PSD efficiency. (4) Line width derived temperatures may be due, in part, to a non-thermal source mechanism such as PSD. (5) Sodium relative intensities show that January and February were the brightest months, consistent with LADEE preliminary results; Kaguya results indicate that February was the brightest month. (6) Line width derived temperatures for the high latitude regions are consistent with the Kaguya results. (7) Relative intensities are highest right after full Moon, perhaps indicative of the role plasma sheet ions play in bringing the sodium atoms to the surface and upon the Moon exiting the magnetotail, these atoms can be knocked off by PSD. (8) Multi-year observations in May (2013 and 2014) combined with results from Smyth and Marconi (1995) and Kaguya, seem to indicate a seasonal variation in the lunar sodium exosphere.

With regard to my sodium and potassium comparisons, my main conclusions are: (1) Limb observations off Aristarchus are brightest compared to all other craters providing evidence for the role KREEP regions play in producing potassium. (2) Potassium is not detected during full Moon phase. (3) The selenographic east limb is hotter than the selenographic west limb, consistent with sodium observations. (4) Potassium line widths are approximately 50 % larger during waxing phase than waning phase at phase angles $> 40^\circ$.

6.5. Future Work

The data presented in this thesis represent one of the most detailed and extensive collection of lunar sodium observations to date. From the observed trends, it is evident that continued observations of the lunar exosphere will help establish seasonal patterns in the lunar SBE and its extended morphology. Future work that would help to further our understanding of the lunar exosphere includes: (1) Modeling the effects of viewing geometry in order to assess by how much the line width is broadened by looking down the sodium tail. (2) Absolute intensity calibration to get intensities in terms of Rayleighs. (3) Determine by how much solar radiation acceleration varies the velocity of the sodium atoms which in turn causes the sodium atoms to see different levels of light, depending on how far up the Solar Fraunhofer line they move. (4) Making observations that can be used to investigate the migration patterns of potassium predicted by existing models. (5) Cross check any anomalous data points with micrometeoroid events. (6) Determine any seasonal variations in the lunar sodium and potassium exosphere through observations and simulations. (7) Confirm whether the flattening of line widths seen at phase angles greater than 40° is due to the Moon entering and exiting the Earth's magnetotail through simulations.

BIBLIOGRAPHY

Agle, D(JPL)., & Brown, D(NASA). (2009). NASA Instruments Reveal Water Molecules on Lunar Surface. *jpl.nasa.gov*.

Clark, E., & Smyth, W. (1995). Potassium and Sodium Abundances on the Lunar Surface: Implications for Atmospheric Composition. *Abstracts of the Lunar Planetary Science Conference*. 26, 251.

Coakley, M., Roesler, F., Reynolds, R., Nossal, S. (1996). Fabry-Perot CCD Annular-summing Spectroscopy: Study and Implementation for Aeronomy Applications. *Applied Optics*, 35(33), 6479-6493.

Colaprete, A., et al. (2014). The Lunar Exosphere as Seen from LADEE UVS. *American Geophysical Union, Fall Meeting 2012*, abstract ID # P21F-04.

Colaprete, A., et al (2014). An Overview of the LADEE Ultraviolet – Visible Spectrometer. *Space Science Reviews*, 185(1), 63-91.

Colaprete, A., et al. (2015). An Examination of LADEE UVS Spectral Variability Associated with the Geminid Meteor Shower. *46th Lunar Planetary Science Conference*, 1832, 2364.

Combi, R., DiSanti, M., Fink, U. (1997). The Spatial Distribution of Gaseous and Atomic Sodium in the Comae of Comets: Evidence for Direct Nucleus and Extended Plasma Sources. *Icarus*, 130, 336-354.

Cremonese, G., & Verani, S. (1997). High Resolution Observations of the Sodium Emission from the Moon. *Advances in Space Research*, 19, 1561-1569.

David, L. (2005, March 29). Earth's Moon: Still a Puzzle. Retrieved April 10, 2015.

Dunbar, B. Is There an Atmosphere on the Moon. Retrieved April 10, 2015.

Elphic, R., (2014). LADEE Project Scientist Update: Milsetones, Maneuvers and Moisture?.

Future of Spaceflight, NASA Missions Information, Future Missions Facts, News, Photos -- National Geographic. Retrieved April 10, 2015.

Gardner, S., Voelz, D., Sechrist, C., Segal, A. (1986). Lidar Studies of the Nighttime Sodium Layer over Urbana, Illinois 1. Seasonal and Nocturnal Variations. *Journal of Geophysical Research*, 91(13), 659 – 673.

- Hasebe, N., et al. (2008). Gamma-Ray Spectrometer (GRS) for Lunar Polar Orbiter SELENE. *Earth Planets Space*, 60, 299-312.
- Hayne, O., et al. (2015). Evidence for Exposed Water Ice in the Moon's South Polar Regions from Lunar Reconnaissance Orbiter Ultraviolet Albedo and Temperature Measurements. *Icarus*, 255, 58 – 69.
- Hernandez G. (1986). Fabry-Perot Interferometers: Cambridge Studies in Modern in Optics 3, *Cambridge University Press*, 343 pages.
- Herwartz, D., Pack, A., Friedrichs, B., & Bischoff, A. (2014). Identification of the giant impactor Theia in lunar rocks. *Science*, 344(6188), 1146-1150.
- Hess, W., Kovach, R., Gast, P.W., & Simmons, G. (2009). The Exploration of the Moon. *Scientific American*.
- Hoffman, H., Hodges, R., Johnson, S., & Evans, E (1973). Lunar Atmospheric Composition Results from Apollo 17. *Proceedings of the Lunar Science Conference*, 4, 2865
- Huebner, F. (1992). Solar Photo Rates for Planetary Atmospheres and Atmospheric Pollutants. *Astrophysics and Space Science*, 195, 1-294.
- Hunten, D., Morgan, T., & Shemansky, D. (1988). *The Mercury Atmosphere* , 562 - 612. University of Arizona Press.
- Juncar, P., Pinard, J., Hamon, J., Chartier, A. (1981). Absolute Determination of the Wavelengths of the Sodium D₁ and D₂ Lines by Using a CW Tunable Dye Laser Stabilized on Iodine. *Metrologia*, 17(3).
- Kagitani et al., (2010). Variation in Lunar Sodium Exosphere Measured from Lunar Orbiter SELENE (Kaguya). *Planetary and Space Science*, 58, 1660-1664.
- Kaguya (2014). NSSDC/COSPAR ID: 2007-039A. nssdc.gsfc.nasa.gov.
- Killen, R., Hurley, D., Farrell, W. (2012). The Effect on the Lunar Exosphere of a Coronal Mass Ejection Passage. *Journal of Geophysical Research*, 117(E10).
- Kozlowski, R., Sprague, A., Hunten, D. (1990). Observations of Potassium in the Tenuous Lunar Atmosphere. *Geophysical Research Letters*, 17(12), 2253-2256.
- Lawrence, J., et al. (1998). Global Element Maps of the Moon: The Lunar Prospector Gamma-ray Spectrometer. *Science*, 281, 1484-1489.
- Marsh, R., Janches, D., Feng, W., Plane, J. (2013). A Global Model of Meteoritic Sodium. *Journal of Geophysical Research*, 118(11), 442-452.

- McGrath, M., Johnson, R., Lanzerotti, L. (1986). Sputtering of Sodium on the Planet Mercury. *Nature*, 323, 694-696.
- Mendillo, M., & Baumgardner, J. (1995). Constraints on the Origin of the Moon's Atmosphere from Observations During a Lunar Eclipse. *Nature*, 377(6548), 404-406.
- Mendillo, M., Baumgardner, J., Flynn, B. (1991). Imaging Observations of the Extended Sodium Atmosphere of the Moon. *Geophysical Research Letters*, 18(11), 2097-2100.
- Mendillo, M., Baumgardner, J., Wilson, J. (1999). Observational Test for the Solar Wind Sputtering Origin of the Moon's Extended Sodium Atmosphere. *Icarus*, 137, 13 - 23.
- Mendillo, M., Emery, J., Flynn, B. (1977b). Modeling the Moon's Extended Sodium Cloud as a Tool for Investigating Sources of Transient Atmospheres. *Advances in Space Research*, 19(10), 1577-1586.
- Mendillo, M., Flynn, B., Baumgardner, J. (1993). Imaging Experiments to Detect an Extended Sodium Atmosphere on the Moon. *Advances in Space Research*, 13(10), 313-319.
- Mierkiewicz, J., Oliverson, R., Roesler, F., Lupie, O. (2014). High-resolution Spectroscopy of the Lunar Sodium Exosphere. *Journal of Geophysical Research: Space Physics*, 119, 4950-4956.
- Mitrofanov, I. et al., (2012). Water Ice Permafrost at Lunar Poles: Observational Evidences from Lend Instrument Onboard LRO. *American Geophysical Union, Fall Meeting 2012*, abstract #P43B-1920
- Namiki et al., (2009). Farside Gravity Field of the Moon from Four-Way Doppler Measurements of SELENE (Kaguya). *Science*, 323(5916), 900-905.
- Neal, C.R. et al. (49 coauthors), 2011, Why the Moon is important for Solar System Science, NRC Planetary Science Decadal Survey Science Collection: Inner Planets – Mercury Venus and the Moon.
- Oliverson, R., et al. (2012). Line Profile Measurements of the Lunar Exospheric Sodium. *Proceedings of the 5th Annual Lunar Science Forum Conference*. July 17-19, NASA Ames Research Center, Moffett Field, CA.
- Phillips, T., (2009). Active Mercury. Science@NASA. *Science.nasa.gov*.
- Phillips, T., & Barry, B., (2005). Abandoned Spaceships. Science@NASA. *Science.nasa.gov*.

- Pierce, A. (1964). The McMath Solar Telescope of Kitt Peak National Observatory. *Applied Optics*, 13(12), 1337-1345.
- Potter, A., & Morgan, T. (1988a). Discovery of Sodium and Potassium Vapor in the Atmosphere of the Moon. *Science*, 241(4866), 675-680.
- Potter, A., & Morgan, T. (1988b). Extended Sodium Exosphere of the Moon. *Geophysical Research Letters*, 15(13), 1515-1518.
- Potter, A., Killen, R., Morgan, T. (2000). Variation of the Lunar Sodium During Passage of the Moon Through the Earth's Magnetotail. *Journal of Geophysical Research*, 105(E6), 15,073-15,084.
- Roesler, F., (1974). Fabry-Perot Instruments of Astronomy. *Astrophysics. Part A: Optical and Infrared*, 531-569.
- Sarantos, M., Killen, R., Sharma, A., Slavin., J. (2010). Sources of Sodium in the Lunar Exosphere: Modeling Using Ground-Based Observations of Sodium Emission and Spacecraft Data of the Plasma. *Icarus*, 205, 364-374.
- Slanger, T., et al. (2005). Variability of the Mesospheric Nightglow Sodium D₂/D₁ Ratio. *Journal of Geophysical Research*, 110 (D23).
- Slavin, A., et al. (1985). An ISEE 3 Study of Average and Substorm Conditions in the Distant Magnetotail. *Journal of Geophysical Research*, 90, 10875.
- Smith, S., Wilson, J., Baumgardner, J., Mendillo, M. (1999). Discovery of the Distant Lunar Sodium Tail and its Enhancement Following the Leonid Meteor Shower of 1998. *Geophysical Research Letters*, 26(12), 1649-1652.
- Smyth, W., Marconi, M. (1995). Theoretical Overview and Modeling of the Sodium and Potassium Atmospheres of the Moon. *The Astrophysical Journal*, 443, 371-392.
- Sprague, A., Kozlowski, R., Hunten, D., Wells, W., & Grosse, F. (1992). The Sodium and Potassium Atmosphere of the Moon and its Interaction with the Surface. *Icarus*, 96, 27-42.
- Stern, A. (1999). The Lunar Atmosphere : History, Status, Current Problems, and Context. *Reviews of Geophysics*, 453-491.
- Tenishev, V., Rubin, M., Tucker, O., Combi, R., Sarantos. M. (2013). Kinetic Modeling of Sodium in the Lunar Exosphere. *Icarus*, 226, 1538-1549.
- Tentative Signs of Water Found on Moon. *Space.com*.

- Thompson, A. (2009, September 17). Tentative Signs of Water Found on Moon. *Space.com*.
- Tufte, S. (1997). The Wham Spectrometer: Design, Performance Characteristics, & First Results. Ph.D. Dissertation. University of Wisconsin-Madison.
- Wilson, J., Baumgardner, J., Mendillo, M. (2003). The Outer Limits of the Lunar Sodium Exosphere. *Geophysical Research Letters*, 30(12).
- Yakshinskiy, V., & Madey, E. (1999). Photon-Stimulated Desorption as a Substantial Source of Sodium in the Lunar Atmosphere. *Nature*, 400(6745), 642-644.
- Yokota, S., et al. (2014). Structure of the Ionized Lunar Sodium and Potassium Exosphere: Dawn-Dusk Asymmetry. *Journal of Geophysical Research: Planets*, 119, 798-809.
- ZeZhou, S., Yang, J., He, Z. (2013). Technological Advancements and Promotion Roles of Chang'e – 3 Lunar Probe Mission. *Science China*, 56(11), 2702-2708.

APPENDIX A

Table A.1 Lunar sodium Observations, 2013 Nov - 2014 May

Date	Offset Crater	Time (UTC)	Pointing Location	Lunar Distance (km)	Phase Angle (deg)	Width (km/s)	Width error (km/s)
19-Nov-2013							
moon_14	Grimaldi	5:49	limb	395,843	18.85	2.70	0.29
moon_15	Grimaldi	5:56	field lens	395,760	18.89	2.76	0.28
moon_16	Grimaldi	6:05	28 sec	395,659	18.93	3.17	0.61
moon_22	Langrenus	7:13	14 sec	395,097	19.25	3.80	0.46
moon_23	Langrenus	7:22	28 sec	395,052	19.29	3.67	0.52
moon_29	Grimaldi	8:08	limb	394,933	19.50	2.19	0.27
moon_31	Aristarchus	8:26	limb	394,938	19.58	2.21	0.50
moon_32	Aristarchus	8:36	limb	394,955	19.62	3.08	0.30
moon_33	Aristarchus	8:43	field lens	394,971	19.65	2.70	0.25
moon_34	Aristarchus	8:52	28 sec	395,000	19.69	2.54	0.30
moon_45	Tycho	10:36	limb	395,850	20.17	3.01	0.38
moon_46	Tycho	10:44	field lens	395,954	20.21	2.95	0.42
moon_47	Plato	10:52	limb	396,062	20.25	2.94	0.23
moon_48	Plato	10:59	field lens	396,132	20.27	2.67	0.30
moon_50	Vieta	11:19	limb	396,462	20.39	2.82	0.28
moon_51	Vieta	11:32	field lens	396,674	20.45	2.69	0.28
20-Nov-2013							
moon_07	Grimaldi	7:29	limb	397,630	30.49	2.82	0.23
moon_08	Grimaldi	7:37	field lens	397,564	30.52	2.35	0.20
moon_09	Aristarchus	7:48	limb	397,481	30.57	2.54	0.32
moon_10	Aristarchus	7:57	field lens	397,421	30.61	2.82	0.27
moon_11	Langrenus	8:14	14 sec	397,327	30.69	2.85	0.43
moon_12	Langrenus	8:24	28 sec	397,283	30.73	2.85	0.44
moon_14	Grimaldi	8:37	limb	397,240	30.79	1.82	0.13
moon_15	Aristarchus	8:46	limb	397,219	30.83	2.02	0.17
moon_23	Tycho	10:03	limb	397,344	31.16	4.11	0.29
moon_24	Tycho	10:10	field lens	397,382	31.20	2.48	0.21

21-Nov-2013							
moon_13	Grimaldi	6:17	limb	400,841	41.14	2.20	0.12
moon_14	Grimaldi	6:24	field lens	400,721	41.17	1.96	0.12
moon_15	Aristarchus	6:31	limb	400,603	41.21	2.00	0.14
moon_16	Aristarchus	6:40	field lens	400,455	41.26	1.93	0.17
moon_24	Aristarchus	8:05	limb	399,323	41.69	1.60	0.12
moon_25	Grimaldi	8:13	limb	399,243	41.72	1.66	0.14
moon_26	Plato	8:23	limb	399,152	41.77	2.12	0.20
moon_27	Plato	8:36	field lens	399,045	41.83	2.03	0.25
moon_28	Tycho	8:43	limb	398,994	41.86	2.20	0.19
moon_29	Tycho	8:50	field lens	398,946	41.89	2.03	0.20
moon_30	Grimaldi	9:05	limb	398,860	41.96	2.30	0.13
moon_31	Grimaldi	9:20	field lens	398,793	42.02	2.03	0.12
moon_32	Grimaldi	9:27	field lens	398,769	42.05	2.00	0.15
moon_33	Grimaldi	9:37	28 sec	398,742	42.09	2.11	0.21
moon_36	Grimaldi	10:06	limb	398,716	42.22	2.59	0.15
moon_37	Aristarchus	10:13	limb	398,722	42.25	1.65	0.33
moon_38	Aristarchus	10:31	limb	398,757	42.33	2.01	0.12
moon_39	Aristarchus	10:31	field lens	398,782	42.36	2.40	0.13
13-Dec-2013							
moon_06	Plato	8:41	limb	390,361	45.89	1.87	0.15
moon_07	Plato	8:49	field lens	390,547	45.84	1.92	0.18
moon_08	Langrenus	9:07	limb	390,972	45.72	1.72	0.14
moon_09	Langrenus	9:15	field lens	391,164	45.66	1.86	0.15
14-Dec-2013							
moon_06	Langrenus	2:38	limb	390,364	36.22	1.82	0.23
moon_07	Langrenus	2:47	field lens	390,282	36.17	1.85	0.19
moon_30	Tycho	5:30	limb	390,024	35.38	2.25	0.28
moon_31	Tycho	5:36	field lens	390,062	35.35	1.75	0.28
moon_32	Langrenus	5:48	limb	390,147	35.30	1.70	0.17
moon_33	Langrenus	5:55	field lens	390,202	35.27	1.74	0.20
moon_44	Messala	8:08	limb	392,033	34.59	1.98	0.19
moon_45	Messala	8:08	field lens	392,033	34.59	2.01	0.22
moon_46	Messala	8:08	28 sec	392,033	34.59	1.76	0.25
15-Dec-2013							
moon_19	Langrenus	4:07	limb	393,097	24.41	2.35	0.20
moon_20	Langrenus	4:28	field lens	392,982	24.31	2.34	0.21
moon_21	Langrenus	4:37	28 sec	392,945	24.27	2.41	0.29

moon_28	Aristarchus	5:32	terminator	392,878	24.02	3.01	0.37
moon_29	Aristarchus	5:40	field lens	392,891	23.98	2.82	0.35
moon_30	Aristarchus	5:48	28 sec	392,910	23.94	3.11	0.48
moon_38	Tycho	6:53	field lens	393,286	23.65	2.61	0.39
moon_39	Tycho	7:03	7'	393,378	23.61	2.45	0.41
moon_43	Plato	7:29	limb	393,656	23.48	2.21	0.27
moon_44	Plato	7:37	field lens	393,753	23.45	2.20	0.31
moon_45	Plato	7:45	7'	393,855	23.41	2.29	0.32
moon_56	Proclus	9:06	limb	395,154	23.00	2.40	0.19
moon_57	Proclus	9:14	field lens	395,305	22.95	2.35	0.20
moon_58	Proclus	9:21	28 sec	395,440	22.91	2.29	0.20
16-Dec-2013							
moon_10	Aristarchus	3:23	limb	396,646	13.63	5.36	0.34
moon_11	Grimaldi	3:30	limb	396,551	13.60	5.71	0.40
moon_12	Tycho	3:39	limb	396,435	13.55	5.80	0.41
moon_14	Furnerius	4:23	limb	395,949	13.33	3.06	0.28
moon_16	Langrenus	4:45	limb	395,763	13.22	3.37	0.25
moon_24	Aristarchus	5:35	limb	395,493	12.99	3.38	0.37
moon_25	Aristarchus	5:42	field lens	395,472	12.96	3.17	0.38
moon_26	Aristarchus	5:49	28 sec	395,457	12.93	3.01	0.40
moon_33	Langrenus	6:31	limb	395,456	12.75	2.77	0.28
moon_34	Langrenus	6:38	field lens	395,472	12.72	2.81	0.35
moon_35	Langrenus	6:59	28 sec	395,537	12.64	2.81	0.38
moon_43	Grimaldi	7:56	field lens	395,949	12.40	4.80	0.39
moon_44	Grimaldi	8:06	28 sec	396,049	12.35	4.61	0.40
17-Dec-2013							
moon_07	Langrenus	6:50	limb	397,519	4.11	3.84	0.44
moon_09	Grimaldi	7:51	limb	397,620	4.07	4.30	0.32
moon_10	Aristarchus	8:01	limb	397,669	4.07	4.05	0.37
moon_11	Langrenus	8:07	limb	397,702	4.07	4.15	0.43
moon_12	Langrenus	8:14	field lens	397,746	4.07	4.18	0.53
moon_13	Langrenus	8:21	28 sec	397,794	4.07	3.88	0.47
moon_16	Tycho	8:44	field lens	397,981	4.07	4.21	0.40
moon_19	Plato	9:02	limb	398,160	4.07	3.26	0.36
moon_20	Plato	9:09	field lens	398,236	4.07	3.01	0.46
moon_21	Aristarchus	9:17	limb	398,329	4.08	3.47	0.50
moon_22	Aristarchus	9:23	field lens	398,402	4.08	3.26	0.54
moon_23	Aristarchus	9:30	28 sec	398,490	4.08	3.14	0.58
moon_26	Grimaldi	9:51	limb	398,778	4.10	4.00	0.38

moon_27	Grimaldi	9:58	field lens	398,866	4.10	3.56	0.40
moon_28	Grimaldi	10:06	28 sec	399,003	4.11	3.42	0.46
moon_38	Cleomedes	11:17	limb	400,263	4.20	2.52	0.30
moon_39	Cleomedes	11:24	field lens	400,401	4.21	2.59	0.33
moon_40	Cleomedes	11:32	28 sec	400,563	4.22	2.38	0.39
18-Dec-2013							
moon_06	Langrenus	3:21	limb	402,080	10.02	6.05	0.87
moon_07	Grimaldi	3:39	limb	401,737	10.12	5.40	0.60
moon_08	Tycho	3:48	limb	401,570	10.17	4.68	0.56
moon_09	Aristarchus	3:56	limb	401,425	10.21	4.43	0.50
moon_10	Plato	4:03	limb	401,300	10.24	5.68	0.62
moon_12	Plato	4:35	limb	400,760	10.40	5.13	0.64
19-Dec-2013							
moon_14	Langrenus	7:59	Crater - 28 sec	400,053	21.87	2.40	0.41
moon_15	Cleomedes	8:07	terminator	400,011	21.91	2.63	0.43
moon_16	Cleomedes	8:14	field lens	399,988	21.94	2.43	0.37
moon_17	Cleomedes	8:22	Crater - 32 sec	399,966	21.98	2.22	0.41
moon_19	Grimaldi	8:36	limb	399,942	22.04	2.51	0.17
moon_20	Grimaldi	8:43	field lens	399,937	22.07	2.46	0.20
moon_21	Grimaldi	8:49	28 sec	399,937	22.09	2.39	0.23
moon_22	Aristarchus	8:59	limb	399,941	22.13	2.49	0.18
moon_23	Aristarchus	9:05	field lens	399,951	22.16	2.33	0.20
moon_24	Aristarchus	9:13	28 sec	399,968	22.20	2.36	0.30
moon_34	Tycho	10:15	field lens	400,294	22.47	2.82	0.32
moon_35	Tycho	10:22	7'	400,353	22.50	2.67	0.34
moon_36	Plato	10:29	limb	400,415	22.54	2.33	0.22
moon_37	Plato	10:35	field lens	400,472	22.57	2.37	0.24
moon_38	Plato	10:43	7'	400,553	22.60	2.42	0.28
moon_41	Grimaldi	11:06	limb	400,815	22.72	2.89	0.24
moon_44	Aristarchus	11:28	limb	401,105	22.83	2.55	0.19
moon_47	Langrenus	11:49	limb	401,414	22.94	3.45	0.54
moon_50	Cleomedes	12:10	terminator	401,753	23.06	3.56	0.47
moon_55	Aristarchus	12:45	limb	402,377	23.26	2.33	0.17
moon_56	Grimaldi	12:51	limb	402,491	23.30	2.29	0.20
moon_59	Plato	13:07	limb	402,802	23.40	2.31	0.24
moon_60	Tycho	13:13	limb	402,921	23.43	2.32	0.25
10-Jan-2014							

moon_11	Cleomedes	7:21	limb	391,809	65.47	1.61	0.09
moon_12	Cleomedes	7:29	field lens	391,996	65.42	1.60	0.12
moon_13	Langrenus	7:39	limb	392,232	65.35	1.55	0.08
moon_14	Langrenus	7:49	field lens	392,472	65.29	1.56	0.10
moon_15	Langrenus	7:59	28 sec	392,665	65.23	1.50	0.16
moon_17	Langrenus	8:15	limb	393,106	65.11	1.46	0.24
11-Jan-2014							
moon_10	Langrenus	3:51	limb	391,994	55.17	1.75	0.09
moon_11	Langrenus	3:59	field lens	392,020	55.14	1.68	0.11
moon_12	Cleomedes	4:06	limb	392,063	55.10	1.82	0.08
moon_13	Cleomedes	4:13	field lens	392,103	55.07	1.67	0.09
moon_15	Tycho	4:28	Crater - 5'36"	392,202	55.00	1.86	0.27
moon_16	Tycho	4:37	Crater - 8'	392,271	54.96	1.92	0.35
moon_17	Petavinus	4:56	limb	392,442	54.87	1.74	0.16
moon_18	Petavinus	5:05	field lens	392,534	54.83	1.69	0.12
moon_20	Plato	5:16	Crater + 4'17'	392,655	54.78	1.74	0.25
moon_21	Plato	5:25	Crater + 6'20"	392,762	54.74	1.73	0.29
moon_26	Cleomedes	6:40	limb	393,901	54.36	1.48	0.08
moon_27	Langrenus	6:48	limb	394,046	54.32	1.52	0.10
moon_28	Langrenus	6:56	limb	394,196	54.28	1.59	0.11
moon_29	Langrenus	7:04	field lens	394,349	54.23	1.71	0.12
moon_30	Langrenus	7:13	28 sec	394,525	54.18	1.59	0.19
moon_32	Langrenus	7:30	limb	394,870	54.09	1.53	0.24
moon_33	Langrenus	7:37	limb	395,017	54.05	1.74	0.19
moon_36	Cleomedes	8:05	limb	395,625	53.88	1.66	0.10
moon_37	Cleomedes	8:12	field lens	395,781	53.83	1.75	0.10
moon_38	Cleomedes	8:20	28 sec	395,963	53.78	1.73	0.14
moon_40	Cleomedes	8:36	limb	396,331	53.68	1.54	0.27
12-Jan-2014							
moon_22	Langrenus	5:00	limb	395,327	43.65	1.70	0.14
moon_23	Petavinus	5:07	limb	395,366	43.62	1.64	0.12
moon_24	Cleomedes	5:13	limb	395,402	43.60	1.71	0.13
moon_27	Plato	5:47	limb	395,671	43.44	1.92	0.17
moon_29	Plato	5:56	field lens	395,759	43.40	2.14	0.19
moon_30	Cleomedes	6:06	limb	395,865	43.36	1.93	0.17
moon_31	Cleomedes	6:14	field lens	395,955	43.32	1.87	0.18
moon_32	Langrenus	6:21	limb	396,039	43.29	1.86	0.14

moon_33	Langrenus	6:29	field lens	396,140	43.25	1.97	0.15
moon_34	Petavinus	6:36	limb	396,232	43.22	1.89	0.14
moon_35	Petavinus	6:45	field lens	396,356	43.18	2.05	0.16
moon_36	Tycho	7:02	limb	396,607	43.09	2.26	0.31
moon_36	Tycho	7:11	field lens	396,748	43.05	2.15	0.34
moon_42	Langrenus	7:50	limb	397,422	42.85	2.15	0.11
moon_43	Langrenus	7:59	field lens	397,553	42.81	2.02	0.16
moon_44	Langrenus	8:07	28 sec	397,745	42.75	2.08	0.28
moon_51	Cleomedes	8:52	limb	398,670	42.49	1.91	0.16
moon_52	Cleomedes	8:59	field lens	398,778	42.46	1.83	0.22
moon_53	Cleomedes	9:06	28 sec	398,974	42.41	2.42	0.22
13-Jan-2014							
moon_16	Cleomedes	4:50	limb	397,609	32.68	1.83	0.17
moon_17	Langrenus	4:57	limb	397,606	32.65	1.88	0.17
moon_18	Petavinus	5:04	limb	397,608	32.62	1.85	0.21
moon_19	Petavinus	5:17	limb	397,623	32.56	2.08	0.18
moon_20	Petavinus	5:25	field lens	397,640	32.53	2.17	0.21
moon_21	Petavinus	5:33	28 sec	397,663	32.49	1.95	0.34
moon_27	Langrenus	6:13	limb	397,865	32.32	2.07	0.20
moon_28	Langrenus	6:20	field lens	397,915	32.29	2.15	0.22
moon_29	Langrenus	6:28	28 sec	397,978	32.26	2.15	0.30
moon_35	Cleomedes	7:22	limb	398,543	32.02	1.99	0.24
moon_36	Cleomedes	7:30	field lens	398,646	31.98	2.12	0.28
moon_37	Cleomedes	7:37	28 sec	398,741	31.95	2.37	0.44
moon_44	Plato	8:34	field lens	399,643	31.67	2.82	0.33
moon_48	Aristarchus	9:00	Crater + 22 sec	400,121	31.53	2.57	0.36
moon_49	Aristarchus	9:08	Crater + 36 sec	400,276	31.48	2.67	0.39
moon_50	Tycho	9:19	limb	400,493	31.42	3.27	0.51
moon_51	Tycho	9:26	field lens	400,635	31.38	2.13	0.39
moon_52	Tycho	9:33	7'	400,778	31.34	2.49	0.45
14-Jan-2014							
moon_09	Cleomedes	4:19	limb	399,629	22	2.67	0.20
moon_10	Cleomedes	4:29	field lens	399,551	21.95	2.64	0.22
moon_17	Langrenus	5:42	limb	399,246	21.64	2.48	0.23
moon_18	Langrenus	5:49	field lens	399,242	21.62	2.90	0.31
moon_19	Langrenus	5:59	28 sec	401,968	21.58	2.33	0.25
moon_20	Langrenus	6:06	42 sec	399,252	21.55	2.31	0.28
moon_21	Langrenus	6:14	1 min	399,265	21.51	2.62	0.34

moon_25	Petavinus	6:52	limb	399,411	21.36	2.91	0.23
moon_26	Petavinus	7:00	field lens	399,458	21.33	3.11	0.27
moon_27	Petavinus	7:09	28 sec	399,518	21.29	3.16	0.30
moon_33	Aristarchus	8:02	Crater + 22 sec	400,014	21.06	3.58	0.38
moon_34	Aristarchus	8:09	Crater + 36 sec	400,097	21.03	3.78	0.42
moon_35	Aristarchus	8:18	Crater + 50 sec	400,209	20.99	3.58	0.40
moon_37	Grimaldi	8:34	Crater + 10 sec	400,424	20.92	3.77	0.37
moon_38	Grimaldi	8:40	Crater + 24 sec	400,509	20.89	3.72	0.30
moon_42	Plato	9:17	limb	401,091	20.71	2.71	0.19
moon_43	Plato	9:25	field lens	401,228	20.67	2.67	0.21
moon_44	Plato	9:33	7'	401,369	20.63	1.96	0.32
moon_45	Plato	9:41	10.5'	401,514	20.59	1.94	0.27
moon_46	Tycho	9:49	limb	401,662	20.55	2.66	0.32
moon_47	Tycho	9:57	field lens	401,813	20.51	2.92	0.42
moon_48	Tycho	10:05	7'	401,968	20.46	3.54	0.87
moon_49	Tycho	10:14	10.5'	402,146	20.41	3.59	0.39
moon_54	Langrenus	10:57	limb	403,038	20.16	3.14	0.26
moon_55	Petavius	11:04	limb	403,188	20.12	3.18	0.25
moon_56	Cleomedes	11:12	limb	403,362	20.07	2.68	0.40

15-Jan-
2014

moon_10	Grimaldi	4:20	limb	401,082	11.63	4.01	0.42
moon_12	Grimaldi	4:44	28 sec	400,805	11.53	3.27	0.38
moon_18	Langrenus	5:37	limb	400,359	11.32	2.66	0.29
moon_19	Langrenus	5:45	field lens	400,313	11:29	2.85	0.32
moon_20	Langrenus	5:55	28 sec	400,263	11:25	2.97	0.39
moon_26	Aristarchus	6:47	limb	400,152	11:06	2.99	0.44
moon_27	Aristarchus	6:55	field lens	400,158	11:03	3.70	0.34
moon_28	Aristarchus	7:03	28 sec	400,169	11:00	3.48	0.36
moon_34	M Cleomedes	7:47	limb	400,337	10.85	2.43	0.30
moon_35	Cleomedes	7:57	field lens	400,399	10.81	2.08	0.24
moon_36	Cleomedes	8:05	28 sec	400,456	10.78	2.70	0.28
moon_42	Plato	8:57	limb	400,958	10.60	1.98	0.33
moon_47	Tycho	9:40	limb	401,537	10.43	2.13	0.40
moon_48	Tycho	9:47	field lens	401,643	10.40	3.23	0.32
moon_49	Tycho	9:55	7'	401,769	10.37	3.48	0.35

16-Jan-2014							
moon_10	Langrenus	4:37	limb	401,808	5.15	3.42	0.39
moon_11	Langrenus	4:47	field lens	401,660	5.16	3.85	0.60
moon_12	Langrenus	5:01	28 sec	401,464	5.17	4.11	0.60
moon_17	Grimaldi	6:40	field lens	400,530	5.26	3.73	0.37
moon_18	Grimaldi	6:48	28 sec	400,492	5.27	3.66	0.40
moon_24	Aristarchus	7:29	field lens	400,390	5.34	3.22	0.27
moon_25	Aristarchus	7:39	28 sec	400,389	5.36	3.37	0.35
moon_31	Cleomedes	8:19	limb	400,480	5.43	3.49	0.44
moon_32	Cleomedes	8:27	field lens	400,516	5.45	2.70	0.42
moon_33	Cleomedes	8:35	28 sec	400,558	5.47	3.03	0.42
moon_40	Plato	9:22	field lens	400,920	5.58	2.47	0.41
moon_44	Tycho	10:05	limb	401,416	5.69	3.00	0.38
moon_45	Tycho	10:14	field lens	401,538	5.72	3.23	0.31
moon_46	Tycho	10:21	7'	401,637	5.74	3.47	0.52
moon_51	Petavinus	11:04	limb	402,317	5.87	3.16	0.56
moon_52	Petavinus	11:13	field lens	402,475	5.90	3.66	0.55
moon_53	Petavinus	11:25	28 sec	402,691	5.94	3.93	0.46
17-Jan-2014							
moon_10	Grimaldi	5:17	limb	401,542	12.74	2.44	0.25
moon_11	Aristarchus	5:31	limb	401,324	12.80	3.12	0.29
moon_12	Langrenus	5:45	limb	401,121	12.87	3.66	0.23
moon_13	Cleomedes	6:01	limb	400,906	12.94	3.21	0.26
moon_17	Langrenus	6:32	limb	400,549	13.08	3.58	0.50
moon_18	Langrenus	6:46	field lens	400,415	13.14	3.52	0.72
moon_19	Langrenus	7:00	28 sec	400,297	13.20	3.28	0.61
moon_27	Grimaldi	8:21	field lens	399,975	13.55	3.32	0.34
moon_28	Grimaldi	8:33	28 sec	399,980	13.60	3.42	0.42
moon_33	Aristarchus	9:15	limb	400,106	13.79	2.78	0.33
moon_34	Aristarchus	9:26	field lens	400,166	13.84	2.57	0.32
moon_35	Aristarchus	9:39	28 sec	400,251	13.90	3.05	0.63
moon_49	Plato	12:02	limb	402,100	14.64	2.95	0.41
moon_50	Plato	12:13	field lens	402,300	14.71	2.65	0.38
moon_52	Tycho	12:40	field lens	402,814	14.87	2.85	0.52
18-Jan-2014							
moon_12	Grimaldi	6:04	limb	400,522	23.41	2.75	0.40
moon_13	Grimaldi	6:17	field lens	400,314	23.47	2.99	0.47
moon_14	Grimaldi	6:30	28 sec	400,118	23.54	2.91	0.45

moon_20	Aristarchus	8:09	limb	399,087	24.00	2.61	0.20
moon_22	Aristarchus	8:33	28 sec	398,970	24.11	2.26	0.35
moon_28	Langrenus	9:32	Crater - 12 sec	398,921	24.38	3.53	0.43
moon_29	Langrenus	9:46	Crater - 26 sec	398,958	24.44	3.69	0.62
moon_36	Plato	10:55	field lens	399,410	24.77	3.16	0.32
moon_40	Tycho	12:09	field lens	400,342	25.16	2.85	0.52
moon_41	Tycho	12:22	7'	400,547	25.24	2.67	0.64
19-Jan-2014							
moon_14	Grimaldi	5:49	limb	399,959	34.13	2.54	0.21
moon_15	Grimaldi	5:56	field lens	399,835	34.17	2.79	0.29
moon_16	Grimaldi	6:08	28 sec	399,575	34.24	3.14	0.43
20-Jan-2014							
moon_32	Grimaldi	9:15	limb	395,008	46.24	2.16	0.16
moon_33	Grimaldi	9:27	field lens	394,907	46.29	1.97	0.17
moon_34	Grimaldi	9:49	28 sec	394,757	46.40	2.11	0.27
moon_40	Aristarchus	11:17	limb	394,630	46.81	1.95	0.13
moon_41	Aristarchus	11:29	field lens	394,670	46.87	1.85	0.14
moon_42	Aristarchus	11:41	28 sec	394,725	46.93	1.85	0.21
21-Jan-2014							
moon_07	Grimaldi	6:43	limb	395,104	56.60	2.08	0.15
moon_08	Grimaldi	6:56	field lens	394,827	56.68	1.83	0.10
moon_09	Grimaldi	7:08	28 sec	394,534	56.76	2.00	0.17
moon_14	Aristarchus	8:06	limb	393,339	57.11	2.01	0.08
moon_15	Aristarchus	8:18	field lens	393,118	57.18	2.09	0.12
moon_16	Aristarchus	8:30	28 sec	392,908	57.25	2.16	0.15
9-Feb-2014							
moon_12	Langrenus	8:01	limb	399,607	62.36	1.83	0.11
moon_13	Langrenus	8:08	field lens	399,765	62.31	1.79	0.14
moon_14	Cleomedes	8:15	limb	399,924	62.27	1.96	0.12
moon_15	Cleomedes	8:22	field lens	400,085	62.22	2.06	0.16
moon_16	Cleomedes	8:29	28 sec	400,246	62.17	1.67	0.19
moon_17	Langrenus	8:36	28 sec	400,408	62.12	1.62	0.18
10-Feb-2014							
moon_14	Langrenus	4:00	limb	398,138	52.59	2.12	0.18
moon_15	Langrenus	4:08	field lens	398,153	52.55	2.56	0.32
moon_16	Cleomedes	5:01	limb	398,405	52.33	2.11	0.17

moon_17	Cleomedes	5:13	field lens	398,497	52.27	1.96	0.18
moon_18	Cleomedes	5:20	28 sec	398,557	52.24	2.01	0.27
moon_24	Langrenus	6:06	28 sec	399,051	52.04	1.89	0.26
moon_28	Tycho	6:37	Crater - 5.5'	399,479	51.89	3.08	0.30
moon_29	Tycho	6:45	Crater - 7'	399,601	51.85	2.80	0.32
moon_30	Plato	6:53	Crater + 5.5'	399,727	51.81	3.89	0.40
11-Feb-2014							
moon_18	Langrenus	5:13	limb	399,669	41.38	1.83	0.12
moon_19	Cleomedes	5:22	limb	399,702	41.34	1.82	0.12
moon_21	Langrenus	5:33	limb	399,752	41.29	2.04	0.14
moon_22	Langrenus	5:41	field lens	399,796	41.26	1.95	0.18
moon_23	Langrenus	5:47	28 sec	399,832	41.23	1.99	0.27
moon_31	Cleomedes	6:51	limb	400,417	40.95	2.00	0.16
moon_32	Cleomedes	6:58	field lens	400,489	40.92	2.00	0.20
moon_33	Cleomedes	7:06	28 sec	400,603	40.88	1.95	0.27
moon_40	Tycho	8:10	Crater - 5.5'	401,578	40.56	2.21	0.26
moon_41	Tycho	8:19	Crater - 7'	401,737	40.51	2.25	0.31
moon_42	Tycho	8:27	Crater - 10'	401,882	40.47	2.01	0.31
moon_43	Plato	8:35	Crater + 5.5'	402,030	40.42	1.89	0.23
moon_44	Plato	8:44	Crater + 8'	402,200	40.37	1.89	0.27
moon_45	Plato	8:51	Crater + 11'	402,336	40.33	1.90	0.27
moon_49	Aristarchus	9:31	Crater + 24 sec	403,148	40.09	2.21	0.24
moon_50	Aristarchus	9:39	Crater + 38 sec	403,318	40.04	2.35	0.27
12-Feb-2014							
moon_16	Langrenus	4:50	limb	400,184	30.64	3.06	0.26
moon_17	Cleomedes	5:26	limb	400,106	30.49	2.78	0.38
moon_19	Langrenus	5:37	limb	400,107	30.47	2.69	0.33
moon_20	Langrenus	5:45	field lens	400,114	30.45	2.75	0.29
moon_21	Langrenus	5:55	28 sec	400,132	30.42	2.59	0.31
moon_27	Cleomedes	6:38	limb	400,314	30.20	2.89	0.39
moon_28	Cleomedes	6:45	field lens	400,360	30.17	3.00	0.29
moon_29	Cleomedes	6:53	28 sec	400,417	30.13	2.77	0.34
moon_35	Plato	7:51	Crater + 5.5'	16.07403	29.87	2.23	0.25
moon_36	Plato	8:00	Crater + 8'	16.05583	29.83	2.23	0.26
moon_37	Plato	8:08	Crater + 11.5'	16.03942	29.79	2.39	0.33
moon_38	Tycho	8:18	Crater - 5'	16.01862	29.74	2.49	0.27
moon_39	Tycho	8:26	Crater - 8'	16.00176	29.70	3.15	0.23

moon_40	Tycho	8:33	Crater - 11'	15.98685	29.67	3.10	0.23
moon_45	Aristarchus	9:11	Crater + 38 sec	15.90355	29.47	2.63	0.47
moon_47	Cleomedes	9:27	limb	15.86741	29.38	2.35	0.24
moon_48	Cleomedes	9:38	field lens	15.84225	29.32	2.39	0.27
moon_49	Langrenus	9:45	limb	15.82611	29.27	2.31	0.22
moon_50	Langrenus	9:54	field lens	15.80522	29.22	2.30	0.28
moon_51	Petavinus	10:03	limb	15.78420	29.17	2.32	0.22
moon_52	Petavinus	10:10	field lens	15.76776	29.12	2.46	0.27
13-Feb-2014							
moon_14	Langrenus	4:05	limb	400,617	20.10	1.79	0.31
moon_15	Cleomedes	4:12	limb	400,533	20.07	1.83	0.26
moon_16	Petavinus	4:19	limb	400,452	20.04	1.93	0.29
moon_17	Tycho	4:35	limb	400,283	19.97	1.94	0.30
moon_18	Messala	4:59	limb	400,087	19.88	1.68	0.28
moon_19	Plato	5:14	limb	399,965	19.81	1.44	0.28
moon_23	Langrenus	5:36	limb	399,847	19.72	3.17	0.29
moon_24	Langrenus	5:44	field lens	399,815	19.68	3.29	0.29
moon_31	Cleomedes	6:33	limb	399,752	19.49	3.03	0.22
moon_32	Cleomedes	6:40	field lens	399,761	19.46	2.52	0.35
moon_33	Cleomedes	6:47	28 sec	399,775	19.43	3.19	0.38
moon_39	Petavinus	7:27	limb	399,945	19.27	3.11	0.19
moon_40	Petavinus	7:34	field lens	399,990	19.24	3.24	0.23
moon_41	Petavinus	7:42	28 sec	400,046	19.21	3.34	0.28
moon_47	Tycho	8:33	limb	400,538	18.98	3.18	0.24
moon_48	Tycho	8:40	field lens	400,622	18.95	3.26	0.28
moon_49	Tycho	8:50	7'	400,749	18.91	2.14	0.48
moon_51	Plato	9:05	limb	400,954	18.84	2.28	0.31
moon_52	Plato	9:13	field lens	401,069	18.80	2.43	0.36
moon_53	Plato	9:21	7'	401,189	18.76	2.60	0.39
moon_58	Aristarchus	9:56	Crater + 28 sec	401,764	18.58	2.90	0.34
moon_59	Aristarchus	10:03	Crater + 38 sec	401,887	18.54	2.59	0.34
moon_61	Grimaldi	10:19	Crater + 16 sec	402,179	18.46	2.76	0.40
moon_62	Grimaldi	10:26	Crater + 30 sec	402,311	18.42	2.74	0.34
14-Feb-2014							
moon_15	Langrenus	4:39	limb	399,735	9.64	2.07	0.41

moon_16	Langrenus	4:52	field lens	399,564	9.58	2.45	0.37
moon_17	Langrenus	5:03	28 sec	399,431	9.54	2.53	0.47
moon_23	Grimaldi	6:02	limb	398,895	9.33	2.29	0.42
moon_24	Grimaldi	6:14	field lens	398,824	9.29	2.29	0.39
moon_25	Grimaldi	6:25	28 sec	398,772	9.25	2.39	0.43
moon_32	Cleomedes	7:29	limb	398,698	9.04	2.24	0.33
moon_33	Cleomedes	7:44	field lens	398,738	8.99	2.51	0.38
moon_34	Cleomedes	7:57	28 sec	398,780	8.96	2.53	0.37
moon_40	Aristarchus	8:55	limb	399,208	8.76	2.37	0.31
moon_41	Aristarchus	9:06	field lens	399,321	8.72	2.78	0.33
moon_42	Aristarchus	9:20	28 sec	399,479	8.67	2.59	0.33
moon_48	Plato	10:13	limb	400,212	8.48	2.19	0.27
moon_49	Plato	10:25	field lens	400,405	8.43	2.19	0.31
moon_50	Plato	10:38	7'	400,624	8.38	2.04	0.36
moon_51	Tycho	10:51	limb	400,853	8.33	2.78	0.28
moon_52	Tycho	11:03	field lens	401,072	8.28	2.52	0.27
moon_53	Tycho	11:15	7'	401,298	8.22	2.65	0.32
18-Feb-2014							
moon_24	Grimaldi	6:34	limb	391,584	37.55	2.03	0.18
moon_25	Aristarchus	6:48	limb	391,318	37.64	2.01	0.15
moon_26	Tycho	7:00	limb	391,101	37.71	2.61	0.24
moon_30	Grimaldi	7:38	limb	390,482	37.92	2.06	0.18
moon_31	Grimaldi	7:49	field lens	390,324	37.98	2.17	0.21
moon_32	Grimaldi	8:01	28 sec	390,163	38.04	2.06	0.28
moon_39	Aristarchus	9:16	limb	389,452	38.43	1.88	0.13
moon_40	Aristarchus	9:27	field lens	389,392	38.48	2.09	0.18
moon_41	Aristarchus	9:40	28 sec	389,336	38.55	1.99	0.22
moon_47	Tycho	10:40	limb	389,294	38.84	2.53	0.24
moon_48	Tycho	10:59	field lens	389,337	38.91	2.35	0.31
moon_49	Tycho	11:10	7'	389,402	38.99	2.51	0.31
moon_50	Tycho	11:23	10.5'	389,475	39.05	2.83	0.36
moon_52	Plato	11:39	limb	389,586	39.13	2.55	0.25
moon_53	Plato	11:51	field lens	389,684	39.20	2.59	0.29
moon_54	Plato	12:03	7'	389,794	39.26	2.17	0.30
19-Feb-2014							
moon_14	Grimaldi	8:37	limb	386,885	49.85	1.76	0.08
moon_15	Grimaldi	8:44	field lens	386,789	49.89	1.76	0.09
moon_16	Aristarchus	8:50	limb	386,710	49.92	1.78	0.07
moon_17	Aristarchus	8:58	field lens	386,621	49.96	1.81	0.10

moon_18	Tycho	9:05	limb	386,525	50.00	2.46	0.20
moon_19	Tycho	9:16	field lens	386,402	50.06	2.31	0.20
moon_21	Grimaldi	9:28	28 sec	386,280	50.12	1.93	0.12
moon_27	Aristarchus	11:12	28 sec	385,795	50.64	2.37	0.17
20-Feb-2014							
moon_16	Aristarchus	10:24	limb	382,290	62.32	1.68	0.07
moon_17	Aristarchus	10:38	field lens	382,175	62.39	1.72	0.08
moon_18	Aristarchus	10:51	28 sec	382,085	62.46	1.73	0.12
moon_25	Grimaldi	12:08	limb	381,876	62.85	1.73	0.08
moon_26	Grimaldi	12:20	field lens	381,894	62.91	1.73	0.09
moon_27	Grimaldi	12:32	28 sec	381,925	62.97	1.71	0.12
17-Apr-2014							
moon_18	Aristarchus	6:53	limb	374,731	24.97	2.12	0.21
moon_19	Aristarchus	7:01	field lens	374,624	25.02	2.25	0.16
moon_20	Aristarchus	7:08	28 sec	374,535	25.06	2.20	0.19
moon_32	Grimaldi	8:41	limb	373,750	25.58	2.49	0.11
moon_33	Grimaldi	8:57	field lens	373,694	25.66	2.32	0.11
moon_34	Grimaldi	9:05	28 sec	373,675	25.70	2.23	0.14
moon_40	moon_40	9:46	limb	373,670	25.92	2.53	0.17
moon_41	moon_41	9:54	field lens	373,688	25.97	2.50	0.14
moon_42	moon_42	10:01	7'	373,708	26.00	2.25	0.17
moon_45	moon_45	10:24	field lens	373,804	26.13	2.18	0.14
moon_46	moon_46	10:32	7'	373,848	26.17	2.27	0.16
20-Apr-2014							
moon_19	Grimaldi	9:32	limb	368,309	64.93	1.68	0.04
moon_20	Grimaldi	9:38	field lens	368,231	64.97	1.70	0.04
moon_21	Grimaldi	9:45	28 sec	368,143	65.01	1.66	0.05
moon_27	Aristarchus	10:18	limb	367,781	65.20	1.69	0.04
moon_28	Aristarchus	10:25	field lens	367,716	65.24	1.68	0.04
moon_29	Aristarchus	10:32	28 sec	367,655	65.28	1.67	0.06
moon_35	Plato	11:07	limb	367,414	65.48	1.79	0.07
moon_36	Tycho	11:14	limb	367,379	65.52	1.86	0.08
21-Apr-2014							
moon_20	Aristarchus	10:17	limb	367,255	78.44	1.52	0.02
moon_21	Aristarchus	10:24	field lens	367,158	78.48	1.51	0.04
moon_22	Aristarchus	10:30	28 sec	367,079	78.52	1.48	0.05
moon_26	Grimaldi	10:53	limb	366,800	78.66	1.56	0.03
moon_27	Grimaldi	11:01	field lens	366,713	78.70	1.50	0.03

moon_28	Grimaldi	11:08	28 sec	366,641	78.74	1.51	0.05
22-Apr-2014							
moon_22	Aristarchus	9:56	limb	367,752	91.57	1.76	0.02
moon_23	Aristarchus	10:03	field lens	367,622	91.62	1.76	0.03
moon_24	Aristarchus	10:10	28 sec	367,495	91.66	1.75	0.04
moon_25	Grimaldi	10:17	limb	367,370	91.71	1.78	0.03
moon_26	Grimaldi	10:23	field lens	367,266	91.75	1.92	0.07
moon_27	Grimaldi	10:29	28 sec	367,163	91.79	1.92	0.07
9-May-2014							
moon_10	Langrenus	4:17	limb	394,278	67.47	1.72	0.14
moon_10	Langrenus	4:25	field lens	394,325	67.43	1.70	0.18
moon_12	Langrenus	4:34	28 sec	394,385	67.39	1.67	0.23
10-May-2014							
moon_20	Langrenus	5:42	limb	390,851	55.62	1.81	0.13
moon_21	Langrenus	5:49	field lens	390,913	55.58	1.72	0.10
moon_22	Langrenus	6:05	28 sec	391,070	55.50	1.72	0.11
moon_23	Langrenus	6:13	42 sec	391,157	55.46	1.65	0.13
moon_24	Langrenus	6:19	1 min	391,224	55.42	1.32	0.15
moon_25	Langrenus	6:26	2 min	391,307	55.39	1.65	0.15
moon_29	Cleomedes	6:54	limb	391,673	55.23	1.81	0.13
moon_30	Cleomedes	7:02	field lens	391,788	55.18	1.82	0.12
moon_31	Cleomedes	7:10	28 sec	391,906	55.13	1.74	0.14
moon_38	Petavinus	7:59	limb	392,675	54.84	1.93	0.11
moon_39	Petavinus	8:05	field lens	395,817	54.79	1.85	0.11
11-May-2014							
moon_22	Langrenus	7:32	limb	387,083	43.32	1.94	0.14
moon_23	Langrenus	7:39	field lens	387,177	43.27	2.03	0.17
moon_24	Langrenus	7:47	28 sec	387,288	43.23	1.88	0.17
moon_25	Cleomedes	7:55	limb	387,402	43.18	2.02	0.26
moon_26	Cleomedes	8:02	field lens	387,506	43.14	2.00	0.15
moon_27	Cleomedes	8:10	28 sec	387,628	43.09	1.93	0.18
moon_29	Petavinus	8:24	limb	387,850	43.00	2.20	0.15
moon_30	Petavinus	8:30	field lens	387,948	42.96	1.98	0.40
moon_31	Petavinus	8:38	28 sec	388,081	42.91	1.93	0.15
12-May-2014							
moon_16	Langrenus	6:57	limb	381,427	31.48	2.39	0.36
moon_17	Langrenus	7:12	field lens	381,533	31.39	2.37	0.43

moon_18	Langrenus	7:19	28 sec	381,589	31.36	2.43	0.27
moon_24	Cleomedes	8:07	limb	382,079	31.08	2.33	0.33
moon_25	Cleomedes	8:14	field lens	382,164	31.04	2.35	0.35
moon_26	Cleomedes	8:21	28 sec	382,253	31.00	2.52	0.45
moon_35	Petavinus	8:59	limb	382,761	30.78	2.45	0.32
moon_36	Petavinus	9:05	field lens	382,883	30.72	2.47	0.27
moon_37	Petavinus	9:12	28 sec	382,994	30.68	2.40	0.33
14-May-2014							
moon_10	Langrenus	5:14	limb	372,726	7.01	4.69	0.21
moon_11	Langrenus	5:20	field lens	372,656	6.98	3.51	0.23
moon_12	Langrenus	5:27	28 sec	372,578	6.93	4.02	0.30
moon_18	Cleomedes	6:00	field lens	372,268	6.75	3.84	0.27
moon_19	Cleomedes	6:09	28 sec	372,201	6.70	4.37	0.31
moon_31	Aristarchus	7:31	limb	371,935	6.25	3.88	0.25
moon_32	Aristarchus	7:37	field lens	371,940	6.22	4.00	0.27
moon_33	Aristarchus	7:44	28 sec	371,950	6.18	4.16	0.38
15-May-2014							
moon_10	Langrenus	6:07	limb	368,941	6.73	4.00	0.48
moon_11	Langrenus	6:16	field lens	368,842	6.78	3.63	0.36
moon_12	Langrenus	6:27	28 sec	368,729	6.85	3.76	0.36
moon_18	Cleomedes	7:04	field lens	368,428	7.04	3.73	0.41
moon_19	Cleomedes	7:11	28 sec	368,385	7.08	3.76	0.21
moon_24	Aristarchus	7:39	limb	368,257	7.23	3.26	0.25
moon_25	Aristarchus	7:50	field lens	368,227	7.29	3.31	0.30
moon_26	Aristarchus	7:59	28 sec	368,213	7.33	3.42	0.22
moon_31	Grimaldi	8:35	limb	368,218	7.53	4.04	0.24
moon_32	Grimaldi	8:42	field lens	368,234	7.57	3.45	0.27
moon_33	Grimaldi	8:51	28 sec	368,260	7.62	3.62	0.18
moon_40	Tycho	9:38	limb	368,512	7.88	3.00	0.24
moon_41	Tycho	9:45	field lens	368,566	7.92	3.13	0.14
16-May-2014							
moon_10	Langrenus	5:14	Crater - 10 sec	367,707	19.55	3.60	0.38
moon_12	Langrenus	5:29	Crater - 30 sec	367,435	19.66	3.55	0.48
moon_14	Cleomedes	5:40	Crater - 13 sec	367,244	19.73	2.88	0.36
moon_15	Cleomedes	5:48	Crater - 23 sec	367,110	19.78	3.16	0.36

moon_16	Cleomedes	5:55	Crater - 33 sec	366,997	19.83	2.68	0.41
moon_20	Aristarchus	6:15	limb	366,690	19.96	2.37	0.21
moon_21	Aristarchus	6:21	field lens	366,604	19.99	2.45	0.25
moon_22	Aristarchus	6:29	28 sec	366,493	20.04	2.39	0.30
moon_28	Grimaldi	7:04	limb	366,066	20.26	2.31	0.22
moon_29	Grimaldi	7:11	field lens	365,993	20.30	2.71	0.24
moon_30	Grimaldi	7:18	28 sec	365,924	20.34	2.63	0.27
moon_37	Plato	8:02	field lens	365,585	20.59	2.41	0.18
moon_38	Plato	8:10	7'	365,542	20.64	2.45	0.24
moon_39	Tycho	8:19	limb	365,500	20.69	2.72	0.14
moon_40	Tycho	8:26	field lens	365,473	20.73	2.89	0.16
moon_41	Tycho	8:34	7'	365,447	20.77	3.48	0.24
18-May-2014							
moon_16	Aristarchus	8:46	limb	363,613	47.87	2.08	0.13
moon_17	Aristarchus	8:53	field lens	363,540	47.92	3.85	0.33
moon_18	Aristarchus	9:00	28 sec	363,471	47.96	3.63	0.26
moon_24	Grimaldi	9:39	limb	363,160	48.19	4.29	0.39
moon_25	Grimaldi	9:45	field lens	363,124	48.22	3.65	0.33
moon_26	Grimaldi	9:52	28 sec	363,086	48.26	4.09	0.34
moon_32	Tycho	10:29	limb	362,959	48.48	2.67	0.23
20-May-2014							
moon_13	Grimaldi	10:35	limb	364,768	75.56	1.66	0.04
moon_14	Grimaldi	10:41	field lens	364,707	75.59	1.69	0.05
moon_15	Grimaldi	10:49	28 sec	364,631	75.64	1.69	0.07
moon_16	Aristarchus	10:56	limb	364,569	75.69	1.65	0.04
moon_17	Aristarchus	11:03	field lens	364,511	75.73	1.63	0.04
moon_18	Aristarchus	11:10	28 sec	364,457	75.77	1.62	0.05